UNIVERSITY OF CALIFORNIA SAN DIEGO
SAN DIEGO STATE UNIVERSITY

Applications of high-frequency deterministic numerical simulations: Moving forward

A dissertation submitted in partial satisfaction of the
requirements for the degree
Doctor of Philosophy

in

Geophysics

by

Te-Yang Yeh

Committee in charge:

University of California San Diego

Professor Li-Tien Cheng
Professor Peter Shearer

San Diego State University

Professor Kim Olsen, Chair
Professor Steven Day
Professor Samuel Shen

2022

The dissertation of Te-Yang Yeh is approved, and it is acceptable in quality and form for publication on microfilm and electronically.

University of California San Diego

San Diego State University

2022

DEDICATION

To the family that created me, and the one Ting-An and I created.

TABLE OF CONTENTS

LIST OF FIGURES

LIST OF TABLES

ACKNOWLEDGEMENTS

I would like to express my deepest appreciation to my advisor, Dr. Kim Olsen, for his kind support, advice, and inspiration, academically and personally, throughout my entire study. A few years ago, Dr. Olsen not only made my American dream come true, but also brought me into this whole new world of numerical simulation, let me freely explore endless possibilities, and encouraged me to work with many great people. Many thanks to Dr. Steven Day, Dr. Daniel Roten, and Dr. Ossian O'Reilly, from whom I learned a lot on how to establish good practices to become a better scientist (still trying). We have been working together to make many ambitious projects happen using one of the world's fastest supercomputers at the Oak Ridge National Laboratories Computing Facility. I would like to extend my sincere thanks to the Southern California Earthquake Center (SCEC) for being a strong supporter of most of the computational resources for the research that we have been conducting. Thanks should also go to Dr. Christine Goulet at SCEC who plays an important role in securing resources that made many parts of my research possible. I feel extremely lucky to be part of this supportive community. Even though the air conditioning at the SCEC annual meeting is colder than the north pole and I caught a cold every single time, going to the SCEC annual meeting in Palm Springs has been my favorite event of the year. But then COVID came along.

Many thanks to the UCSD/SDSU Joint Doctoral Program in Geophysics for giving me the opportunity to appreciate the beauty of both campuses at UC San Diego and San Diego State University. Being able to take classes, do research, and have fun with people at both campuses is what I enjoyed the most. Many thanks to the department chairs, professors, and staff at both campuses. Special thanks to Irene, Heather, Dr. Shuo Ma, my long-time office mate Zhifeng, and all other graduate student cohorts for their companies and support.

Last but not least, I could not have undertaken this journey without my spouse, Ting-An, and our cute son, Gabriel. Having them around is the sweetest thing of my life.

Chapter 2, in full, is a reformatted version of a paper currently in preparation for submission for publication: Yeh, T. and Olsen, K.B. (2022), Fault damage zone effects on ground motions during the 2019 M_w 7.1 Ridgecrest, CA, earthquake. The dissertation author was the primary investigator and author of this paper.

Chapter 3, in full, is a reformatted version of a paper currently in preparation for submission for publication: Yeh, T. and Olsen, K.B. (2022), Simulation and validation of basin effects in Los Angeles during the 2019 M_w 7.1 Ridgecrest, CA earthquake. The dissertation author was the primary investigator and author of this paper.

Chapter 4, in full, is a reformatted version of a paper currently in preparation for submission for publication: Yeh, T. and Olsen, K.B. (2022), Simulation of 0-7.5 Hz deterministic ground motions for Maximum Credible Earthquake scenarios at the Long Valley Dam, CA. The dissertation author was the primary investigator and author of this paper.

VITA

2012	B.S. in Geophysics, National Central University, Taiwan
2014	M.S. in Geophysics, National Central University, Taiwan
2016-2021	Graduate Teaching/Research Assistant, San Diego State University
2022	Ph.D. in Geophysics, University of California, San Diego and San Diego State University

PUBLICATIONS

O'Reilly, O., **Yeh, T.**, Olsen, K. B., Hu, Z., Breuer, A., Roten, D., and Goulet, C. A. (2021). A High-Order Finite-Difference Method on Staggered Curvilinear Grids for Seismic Wave Propagation Applications with Topography. *Bulletin of the Seismological Society of America*. https://doi.org/10.1785/0120210096

Yeh, T. and Olsen, K.B. (2021) Effects of near fault structure on ground motions during the 2019 M_w 7.1 Ridgecrest, CA, earthquake. *In preparation for publication*.

Yeh, T. and Olsen, K.B. (2021) Simulation and validation of basin effects in Los Angeles during the 2019 M_w 7.1 Ridgecrest, CA earthquake. *In preparation for publication*.

Yeh, T. and Olsen, K.B. (2021) Simulation of 0-7.5 Hz deterministic ground motions for Maximum Credible Earthquake scenarios at the Long Valley Dam, CA. *In preparation for publication*.

ABSTRACT OF THE DISSERTATION

Applications of high-frequency deterministic numerical simulations: Moving forward

by

Te-Yang Yeh

Doctor of Philosophy in Geophysics

University of California San Diego, 2022
San Diego State University, 2022

Professor Kim Olsen, Chair

Ground motion prediction plays an important role in seismic hazard analysis. Deterministic wave propagation simulation has proven to be a powerful tool, widely used to predict ground motions in various applications. Recent advances in computing speed and sophistication of numerical methods have allowed ground motion prediction to achieve higher frequencies and broader applicability. However, realistic broadband simulations also require more accurate description of subsurface structure and more complicated physics. Thus, an important question is whether existing velocity models are sufficiently accurate for high frequency simulations. The main objectives of the research presented in this thesis are (1) to examine the efficacy of the

current models for accurate ground motion prediction, and (2) if lacking sufficient accuracy, to establish model calibration procedures to deliver more accurate prediction of high-frequency ground motions. The introductory chapter first lays out the specific research questions addressed in this thesis. The following chapters demonstrate the procedure of using seismic data to constrain seismic frequency-dependent attenuation models and near-surface geotechnical layers. Finally, the calibrated models are used to demonstrate that deterministic ground motion simulation in both linear and nonlinear regimes indeed has the potential to be widely used in seismic hazard analysis.

Chapter 1

Introduction

1.1 Motivation

It is well known that seismic waves radiated from earthquake sources can cause catastrophic damage on built environment. In some scenarios, earthquake ground shaking may trigger other natural phenomena, such as landslides and tsunamis, which can lead to consequences worse than ground shaking. Such scenarios are especially of concern for densely populated areas in the vicinity of seismically active faults. From a hazard mitigation stand point, accurate earthquake ground motion prediction is a critical but challenging task needed to address the associated risks. Ground motion estimation can be obtained from either (1) empirical, (2) stochastic, (3) hybrid stochastic-deterministic, or (4) deterministic approaches, all of which have been shown to be useful. However, each method entails different limitations and assumptions. In general, progressing from approaches (1) to (4) requires increasing computational costs, and better understanding of the properties of subsurface material as well as the physics behind the seismic wave propagation. The topics of the research presented in this thesis pertain to the deterministic approach. The next few paragraphs will briefly discuss the deterministic approach, and the motivation to choose such method over alternative ones. In the last part of this section, we list our research objectives that

the following chapters will be addressing in order to improve ground motion prediction at higher frequencies.

1.2 Methods for ground motion prediction

Characteristics of seismic waveforms are modulated by the source, the path, and the site response. Without detailed knowledge in these areas, ground motion prediction can be done empirically. For areas where large amounts of seismic recordings have been collected (e.g., California, Japan, and Taiwan), empirical ground motion models (GMMs, or ground motion prediction equations, GMPEs), are developed by regression analysis to provide predictions of median values on some important ground motion metrics (e.g., peak ground acceleration, spectral acceleration) along with their uncertainties (Boore and Atkinson, 2008; Boore *et al*., 2014; Zhao *et al*., 2016; Phung *et al*., 2020).

GMPEs do not produce seismic waveforms, which can be very useful in structural engineering analysis. However, seismic waveforms that match the metrics predicted by GMPEs can be generated in a stochastic fashion (such as Boore, 2003). These methods typically combine parametric or functional models of ground motion amplitude spectra with a random phase spectrum, calibrated such to obtain a duration related to the earthquake magnitude and the distance from the source. This approach has been widely used for general engineering practices due to its simplicity and computational efficiency.

Hybrid deterministic-stochastic methods take ground motion prediction one step further by introducing physics-based calculations of synthetic waveforms, typically only for the low-frequency waves (f$\leq$1 Hz), while generation of high-frequency waves remains stochastic. One example is the Southern California Earthquake Center (SCEC) Broadband Platform (BBP) (Maechling *et al*., 2014) which comprises different hybrid methods contributed by many research groups (Anderson, 2014; Atkinson and Assatourians, 2014; Crempien and Archuleta,

2014; Graves and Pitarka, 2014; Olsen and Takedatsu, 2014; Song *et al*., 2014; Song, 2016). Deterministic calculation of the low-frequency wavefield by hybrid methods is a computationally affordable option, in particular using 1D approaches as is the case on the SCEC BBP. However, the stochastic high-frequency component oftentimes comes with large uncertainties, especially for the near-source areas (within about 10 km) where seismic recordings are rare. For areas without well-established GMPEs, models developed for another geological region introduces additional epistemic uncertainties. In addition, the stochastic nature intrinsically limits the resolution of the predicted ground motions, which makes it difficult to adequately capture many features that statistical models cannot appropriately describe.

The deterministic approach, namely physics-based full waveform simulations in a 3D heterogeneous medium, in which the source, the path, and the site response are fully coupled, almost entirely eliminates the limitations of the stochastic methods mentioned above. This approach requires adequate understanding of the material properties of the subsurface, the physics governing the characteristics of the propagating waves, and the seismic source. As solving the elastodynamic equations analytically in a 3D heterogeneous medium is not feasible, the wave equations are solved numerically. Popular 3D deterministic methods successfully applied in seismology include finite-difference (FD), finite-element (FE), spectral-element, and boundary-element methods (Frankel, 1993; Graves, 1996; Olsen, 1994; Maeda and Furumura, 2013; Komatitsch and Vilotte, 1998; Bouchon and Sánchez-Sesma, 2007; Manolis and Beskos, 1988; Tu *et al*., 2006; Bao *et al*., 1998; Breuer *et al*., 2014). FD methods, in particular, have been widely used for large-scale simulation owing to their simplicity in model preparation and parallel code implementation and optimization. For studies presented in this thesis, we applied a very efficient and scalable FD method, AWP-ODC.

Sampling of the earth model at a increased resolution requires a decrease in grid spacing (dh) to achieve a higher maximum frequency (f_{max}), since numerical methods need a certain number of points per minimum wavelength (PPW) to maintain sufficient numerical accuracy (i.e.

$PPW = \frac{V_{min}}{dh \times f_{max}}$), where V_{min} is the minimum seismic velocity in the model. As dh decreases, the computational requirement increases. For example, decreasing dh by a factor of two requires 2^3 times the memory and 2^4 times the computational resources for a regular mesh. Therefore, the size of the simulation domain, f_{max}, and the availability of computational resources are the major limiting factors when evaluating whether 3D deterministic simulation is a feasible option.

1.3 Current status of 3D deterministic simulation

Due to the computational cost, early large-scale 3D numerical simulations in models of southern California were limited to f_{max} of 0.5-1 Hz (e.g., Olsen, 2000; Olsen *et al*., 2006; Day *et al*., 2008; Olsen *et al*., 2009; Graves *et al*., 2011). In addition, the simulations simplified certain model features, e.g., eliminating support for surface topography, or neglecting the very low near-surface seismic wave speeds, to limit the use of resources. Fortunately, many of the complex model features contribute limited effects on the ground motions at low frequencies. For example, Day *et al*. (2008) confirmed that eliminating the very low near-surface seismic wave speeds has negligible effects on ground motions for frequencies below 0.5 Hz.

More recently, improved computing speeds have allowed deterministic simulations to resolve f_{max} up to 1.5-2 Hz (Cui *et al*., 2010; Olsen and Mayhew, 2010), and GPU-accelerated computation has further helped increase f_{max} of elastodynamic simulations to 7.5-10 Hz (Cui *et al*., 2013; Withers *et al*., 2018a; Withers *et al*., 2018b). In addition, extensive numerical development has enabled modeling of the effects of frequency-dependent anelastic attenuation (i.e., Withers *et al*., 2015) and surface topography (O'Reilly *et al*., 2021). Along with the discontinuous-mesh feature that allows for mesh coarsening at greater depth (Nie *et al*., 2017), lower near-surface seismic speeds can now be included when achieving higher f_{max} without significantly increasing the memory use. These code developments have paved the way for simpler and more accurate deterministic wave propagation simulations with high frequencies. The available computing

power now accommodates frequency bands relevant for the most vulnerable buildings ($f \geq 1$ Hz).

Validation is critical to establish confidence in simulation results. For example, intensity measures for ground motion synthetics generated from numerical simulations of scenario earthquakes can be compared against GMPEs (Olsen *et al*., 2009; Roten *et al*., 2012; Withers *et al*., 2018a; Withers *et al*., 2018b), and simulations of recorded events can be validated directly against observed strong motion data. As an example, Taborda and Bielak (2013) and Taborda and Bielak (2014) validated their 0-4 Hz 3D numerical simulations of the 2008 M_w 5.4 Chino Hills, CA, earthquake against strong motion data and found a fair agreement below 0.5 Hz, whereas the simulation increasingly deviated from data as frequencies increased. Thus, the useful maximum frequency of the simulation was lower than the numerical f_{max} due to inaccuracies in the earth model, indicating the need for model improvement.

Hu *et al*. (2022b) calibrated the parameters for formulations of near-surface velocity profiles using 0-1 Hz 3D simulations of the 2014 M_w 5.1 La Habra, CA, earthquake, primarily for locations outside the Los Angeles basin where near-surface velocities are poorly constrained in the Southern California Earthquake Center (SCEC) Unified Community Velocity Model (UCVM) version CVM-S.4.26.M01 (Small *et al*. (2017). In addition, Hu *et al*. (2022a) carried out 0-5 Hz numerical simulations for the same event and derived unbiased prediction of observed spectra and broadband peak amplitudes, where their study demonstrated the contributions from and trade-offs between surface topography, near-surface low-velocity layers, frequency-dependent anelastic attenuation, and small-scale heterogeneities. An important result from these studies is that relatively simple models of near-surface geotechnical layers and attenuation are capable of producing broadband spectral responses in agreement with data, given appropriately calibrated parameters.

During strong shaking, weaker soils near the earth's surface may exhibit nonlinear behavior in which the linear stress-strain relationship breaks down, increasingly important as frequency

increases. To capture nonlinear response in numerical calculations, the GPU-enabled version of AWP-ODC finite-difference code provides support for Drucker-Prager (DP) plasticity (Roten *et al*., 2016). In models with DP plasticity, earth material behaves linearly before reaching the yield stress, after which fully plastic yielding occurs. The DP yield stress depends on cohesion (c), friction angle (ϕ), and fluid pressure (P_f). These parameters must be carefully assigned as they define the yield surface. For extreme scenarios or near-fault ground motions, nonlinearity has been shown to reduce ground motion significantly (Roten *et al*., 2014; Roten *et al*., 2018).

1.4 Research objectives of following chapters

Building upon the success of previous work along with the most recent advances on description of subsurface structure, the research presented in this thesis is dedicated to pursuing better constraints on model parameters that are critical for prediction of high-frequency ground motions. Three chapters follow the introduction. The first two chapters describe validation studies, establishing appropriate model calibration procedures for simulations of high-frequency waves. The third chapter demonstrates how state-of-the-art numerical simulation of ground motion can be a powerful tool in seismic hazard analysis.

Chapter 2 presents 0-3 Hz 3D numerical wave propagation simulations of the 2019 M_w 7.1 Ridgecrest, CA earthquake. This study includes a data-constrained source rupture model, and the effects of surface topography, frequency-dependent anelastic attenuation, and a high-resolution fault damage zone velocity structure. The simulations are carried out in a 200 km $\times$ 300 km domain from the near-source area into the greater Los Angeles area. The main objectives of this study are to (1) investigate the effects of the fault damage zone on ground motions, and (2) better constrain the parameters that characterize the anelastic attenuation model for southern California. The model calibrations carried out in this study facilitate successful validation in both time and frequency domains.

Chapter 3 uses the results of Chapter 2 to test the efficacy of a widely-used Community Velocity Model in terms of predicting the basin amplification response in the greater Los Angeles area. Using strong motion recordings from a high-density seismic data sets, quantitative analysis is conducted to validate the simulated site amplifications at both long (6-8 s) and shorter (1-3 s) periods.

Chapter 4 presents a set of 0-7.5 Hz 3D numerical simulations performed to predict the seismic response of the Long Valley Dam in central California for Maximum Credible Earthquake (MCE) scenarios. The seismic response of the dam is modeled by fully-coupled deterministic numerical calculations in a 3D heterogeneous medium, considering high-resolution surface topography and nonlinear soil response. The near-surface structures and attenuation model are calibrated via the same procedure as used for the Ridgecrest earthquake. The simulations are validated against data for both small (M_w 3.7, with a point-source model) and moderately-sized (M_w 6.4, with a finite-fault model) events. Then, we predict nonlinear ground motion response at different locations inside the dam triggered by M_w 6.6 MCE scenarios along the Hilton Creek Fault, to provide critical information for assessing the stability of the dam structure. This study illustrates how deterministic simulations can be used as a tool in the analysis of seismic risk to the built environment.

Chapter 2

Fault damage zone effects on ground motions during the 2019 M_w 7.1 Ridgecrest, CA, earthquake

We have simulated 0-3 Hz deterministic wave propagation in the Southern California Earthquake Center (SCEC) Community Velocity Model (CVM) version CVM-S4.26-M01 for the 2019 M_w 7.1 Ridgecrest earthquake incorporating a data-constrained high resolution fault zone model (Zhou *et al.*, 2022) in order to investigate the effects of the near-fault low-velocity zone (LVZ) on near-source and far-field ground motions. Strong motion data recorded at 161 stations are used to estimate the optimal parameters for the near-surface geotechnical layer (GTL) and frequency-dependent anelastic attenuation in the model domain ($Q_S = 0.1V_S$, and $Q_S(f) = 0.1V_S f^{0.5}$ for frequencies lower and higher than 1 Hz, respectively). The optimized model was used to quantify the individual effects of the fault zone and the GTL on the ground motions. Our results show that the near-fault LVZ included in the fault zone structure significantly perturbs the predicted ground motions in the near-source region, and increases the peak ground velocities in the western Los Angeles Basin (about 200 km from the source). The fault zone

structure improves modeling of the long-period features in the data and lengthens the coda wave trains, in better agreement with observations. On the other hand, a calibrated GTL is the model feature that most significantly improves the spectral energy toward the observed level.

2.1 Introduction

A fault damage zone structure is generally characterized as a low-velocity zone surrounding a fault plane, embedded in host rocks with higher seismic wave speeds. Numerical modeling studies have shown that the velocity contrast at the boundaries of the damage zone can generate trapped waves, an important signature of fault zones (Li and Leary, 1990; Ben-Zion *et al*., 2003; Lewis *et al*., 2005). Fault-zone trapped waves have also been found to increase the near-fault ground motions (Ben-Zion and Aki, 1990; Peng and Ben-Zion, 2006; Spudich and Olsen, 2001), and numerical simulations have been used to reconstruct the near-fault wave field in the presence of a damage structure (Fohrmann *et al*., 2004; Igel *et al*., 2002; Li and Leary, 1990). These studies suggest that fault damage zone structures are capable of significantly modulating the wave field from earthquakes.

In previous numerical studies of fault zone effects, such as Roten *et al*. (2018), Roten *et al*. (2014), and Graves and Pitarka (2016), damage zones have been described generically by reducing the shear-wave velocities by 30-50% within a predefined width (100-400 m), symmetrically around the fault, based on prior observations of fault zones (Cochran *et al*., 2009; Li *et al*., 2004; Vidale and Li, 2003). Due to the lack of constraints, the fault planes in these studies were typically approximated as a simple vertical plane. Existing, widely used Community Velocity Models (CVMs), such as those developed by the Southern California Earthquake Center (SCEC), typically do not resolve fault damage zones. For these reasons, the effects of including detailed fault zone structures on broadband ground motions from simulation studies are not yet fully understood.

To better understand the effects on ground motions from detailed damage zones with

complex spatial variation, efforts have been made to image the velocity structure of fault zones (Allam *et al*., 2014; Li and Leary, 1990; Scott *et al*., 1994; Zhou *et al*., 2022). Specifically, Zhou *et al*. (2022) obtained a 3D high-resolution shear wave velocity model for the region surrounding the faults that ruptured during the 2019 M_w 7.1 Ridgecrest, CA, earthquake, using ambient noise tomography.

Here, we simulate 0-3 Hz 3D wave propagation for the M_w 7.1 Ridgecrest earthquake to examine the effects of the fault damage zone, incorporated into the larger-scale SCEC CVM-S.4.26.M01 (Small *et al*. (2017), hereafter referred to as CVM-S), compared to strong motion records from the event. Specifically, we performed a set of simulations to isolate the contribution of the fault zone structure in the resulting ground motions. In order to estimate the most accurate response of the fault zone, we first calibrated the parameters of the near-surface geotechnical layer (GTL) and frequency-dependent anelastic attenuation parameters using wave propagation distances in excess of 250 km.

The study is arranged as follows. We first introduce our numerical method and describe how we embed the high-resolution fault zone structure into the SCEC CVM-S. Then, we present a novel approach to enrich a finite-fault source model obtained from a kinematic inversion in spectral energy at frequencies above 1 Hz, which we used for our wave propagation simulations. The anelastic attenuation model for the simulations of Ridgecrest earthquake is calibrated and constrained by strong motion data recorded at various distances. Finally, we compare the wavefields simulated with and without the presence of the fault zone structure and demonstrate its contribution to the ground motions in time and frequency domains.

2.2 Velocity Model

2.2.1 Regional model and fault zone structure

We used a 200 km $\times$ 300 km model domain (black rectangle in Fig. 2.1a) with a depth extent of about 150 km. This domain accommodates both the Ridgecrest earthquake source area and part of the greater Los Angeles region to the south. The seismic velocity and density information was extracted from the SCEC CVM-S. The choice of CVM-S is based on the results by Taborda *et al*. (2016) who found that this model generated ground motions with the best fit to data for a series of small earthquakes, as compared to another widely used CVM.

We incorporated the fault zone structure imaged by Zhou *et al*. (2022) in a 50 km by 45 km by 5 km volume (green dashed box in Fig. 2.1 a-b). The fault zone structure was inverted from seismic data recorded by a data set consisting of a coarse regional array and 2D dense arrays across the faults that ruptured during the M_w 6.4 and the M_w 7.1 2019 Ridgecrest events (Catchings *et al*., 2020). Zhou *et al*. (2022) used the Locally Sparse Tomography (LST) technique (Bianco and Gerstoft, 2018; Bianco *et al*., 2019) and performed ambient noise cross correlation to measure Rayleigh wave group velocities and estimate group velocity dispersion curves. It has been noted that the LST method is capable of resolving both smooth and sharp contrasts (Bianco *et al*., 2019; Zhou *et al*., 2022). The 3D shear wave velocity model was then inverted from the Rayleigh wave group velocity dispersion curves. V_S slices from 0 to 5 km depth are shown in Fig. 2.A.1, revealing a heterogeneous low-velocity flower structure.

Since the fault zone model only provides 3D shear-wave velocity (V_S) structure, we used the empirical relations from Brocher (2005) to compute P-wave velocities (V_P) and densities. To ensure smooth transitions between CVM-S and the fault zone model, we adopted the merging method proposed by Ajala and Persaud (2021) with a 15 km horizontal tapering width along the sides and a 600 m vertical transition at the bottom of the fault zone domain. Horizontal slices in Fig. 2.2 reveal higher spatial complexity in the fault zone model surrounding the faults.

Similarly, Fig. 2.3 compares vertical profiles of V_P, V_S and density at station CLC, located inside the fault zone imaging domain (see Fig. 2.1b for location), showing stronger vertical variation in the fault zone model than the CVM-S from the free surface to a depth of 5 km, expected from the higher resolution in the former. The lowest surface V_S within the imaged fault zone model is around 1,100 m/s, as compared with a minimum surface V_S of 1,400 m/s in the same area of the CVM-S. It is important to avoid artificial velocity contrasts between the fault zone model and the CVM-S in order to minimize numerically-induced reflected waves. Both depth slices (Fig. 2.2) and the smooth vertical transition at the bottom of the imaging domain (Fig. 2.3) suggest that our combined model is sufficiently smooth where the two models intersect.

2.2.2 Geotechnical layer (GTL)

V_S of the top $\sim$ 30 m of Earth's crust is often well constrained from borehole and geotechnical data, or can be estimated as a proxy from topographic surface elevation (e.g., Wald and Allen, 2007). Likewise, velocities of the layers below about 1,000 m depth can be constrained by tomographic results. On the other hand, in particular for rock sites, the velocities between these two regions are often poorly resolved, as is the case for CVM-S. Boore and Joyner (1997) used generic models to bridge the gap between data constraints in the two regions, and Ely *et al*. (2010) proposed a scheme that determines the shallow V_S by interpolation ('tapering') between the V_S30 value and the original tomography model at a certain depth (z_T).

To more accurately describe the near-surface seismic velocities in our simulations, we implemented the GTL using the approach by Ely *et al*. (2010) with a z_T of 700 m, following the analysis of Hu *et al*. (2022b). The implementation of the GTL is the last step of the model preparation, after the fault damage zone model is merged with the CVM-S. V_P, V_S, and density in this depth region are all calculated using the taper formulations by Ely *et al*. (2010). However, one important difference from the approach by Ely *et al*. (2010) is that we only modified the

velocities and densities when the existing V_S is higher than that given by the taper, ensuring that the low velocities in the existing model can remain (e.g., low-velocity basin materials in Los Angeles). Fig. 2.4 demonstrates two different cases using 1D profiles below stations inside (CI_CCC) and outside (CI_WMF) the fault zone imaging domain. We used measured V_S30 values when available (Yong *et al*., 2013), whereas values from Wills *et al*. (2015) were assigned to locations without measurement. Fig. 2.5 shows V_S depth slices of the simulation domain after the implementation of the GTL.

2.3 Broadband source model

To describe the fault rupture process of the 2019 M_w 7.1 Ridgecrest earthquake, we used a finite-fault model from kinematic inversion of seismic and geodetic data by Liu *et al*. (2019). Due to limited temporal resolution often characterizing kinematic inversion results, the spectral energy of the source was deficient at frequencies above 1 Hz. In order to obtain a source with realistic spectral content up to higher frequencies, we propose a method to enhance the seismic energy above the highest frequency resolved by the kinematic inversion. The enhancement is done by simply perturbing the moment-rate functions of all the subfaults with noise following a von Karman correlation function. Fig. 2.6 a-c illustrate this spectral enhancement procedure for a single subfault. The same procedure is then repeated with different random seed numbers for all the subfaults. We used grid search to find the characteristic time and standard deviation for the von Karman noise that generated a total moment-rate spectrum with the best fit to the targeted source spectrum of the form

$$M(f) = \frac{M_0}{1 + (f/f_c)^2}, \tag{2.1}$$

where M_0 is the seismic moment, and f_c is the corner frequency (Brune, 1970). The corner

frequency here is 0.055 Hz, computed from the total moment-rate function of the unperturbed source model. Fig. 2.6 d-e compare the total moment-rate functions with and without the enhancement in time and frequency domains. The moment-rate function is essentially unchanged, while the total moment-rate spectrum decays following the targeted spectral shape with a f^{-2} roll-off rate after the enhancement. For the Liu *et al*. (2019) source model, von Karman noise generated with a characteristic time $T_c = 0.11$ s and standard deviation $\sigma = 0.1$ provided the best fit to the targeted source spectrum.

2.4 Wave propagation method

We performed 3D numerical wave propagation simulations using the highly-scalable code AWP-ODC which solves the velocity-stress wave equation with an explicit staggered-grid finite-difference scheme (Olsen, 1994; Cui *et al*., 2010; Cui *et al*., 2013). This GPU-enabled code is fourth-order accurate in space and second-order accurate in time. The code takes advantage of a discontinuous mesh technique with a change in grid spacing by a factor of 3 between domains vertically, which significantly reduces the memory use (Nie *et al*., 2017). The curvilinear mesh is used in the shallowest mesh block of the domain to include the effects of surface topography (O'Reilly *et al*., 2021). In order to minimize computational requirements, we clamp the lowest shear wave velocities at 300 m/s, which affects less than 40% of the model area (see Fig. 2.5). In order to achieve a maximum frequency of 3 Hz with a minimum shear wave speed of 300 m/s using at least 6.7 grid points per minimum wavelength, the smallest grid spacing in our simulations was set to 15 m (O'Reilly *et al*., 2021). See Table 2.1 for technical details of the numerical simulations. For completeness, we added an approximation of the effects of the material with V_S less than 300 m/s as a post-processing step to the 3D synthetics, although generally negligible in our case, following the approach of Hu *et al*. (2022b).

2.5 Data processing

The ground motions of the M_w 7.1 Ridgecrest event have been well recorded by networks of densely distributed seismic stations throughout the simulation domain. We use acceleration data from HN (broadband accelerograms) channels at stations under network codes CI and NP via the IRIS data fetch tool through the web portal of the Southern California Earthquake Data Center (SCEDC) at Caltech (http://service.scedc.caltech.edu). The poles and zeros for each channel were used to remove the instrument response, and the acceleration waveforms were integrated once to get velocity waveforms. Baselines of the near-fault records (stations shown in Fig. 2.1b) were corrected using the method proposed by Wang *et al*. (2011). Prior to the validations, all observed and simulated data were bandpass filtered between 0.02 - 3 Hz using two forward passes of (causal) 2nd-order Butterworth filter. In total, 161 stations were included in our analysis.

2.6 Calibrating the $Q(f)$ model

A popular procedure for parameterizing the Q model, adopted in many earlier numerical studies, consists of using linear or polynomial relationships between Q and the local V_S (Olsen *et al*., 2003; Pitarka *et al*., 2021; Taborda and Bielak, 2013; Taborda and Bielak, 2014). As frequency increases beyond about 1 Hz, strong motion data in some regions indicate that the seismic attenuation becomes frequency dependent (Aki, 1980; Raoof *et al*., 1999; Phillips *et al*., 2014; Wang and Shearer, 2017), which can be captured by numerical schemes (Withers *et al*., 2015). AWP-ODC supports frequency-dependent attenuation that follows a power-law description:

$$
\begin{aligned}
Q_s(f) &= Q_{s,0}, \quad f < f_0, \\
Q_s(f) &= Q_{s,0}\left(\frac{f}{f_0}\right)^{\gamma}, \quad f \geq f_0,
\end{aligned}
\tag{2.2}
$$

where the transition frequency f_0 is 1 Hz, $Q_{S,0}$ is a constant Q_S value, and the power-law exponent γ controls the rate of increase for the Q_S value above 1 Hz (Withers *et al*., 2015). Following the format of Olsen *et al*. (2003), we assumed a constant Q_S to local V_S ratio, which is $\frac{Q_{s,0}}{V_S} = k$, and therefore, the parameters to be estimated here are k and γ in Eq. (2.2). Here we assumed $Q_P = 2Q_S$, following Olsen *et al*. (2003). The 0-5 Hz simulations by Hu *et al*. (2022a) found optimal ranges of $k = 0.075 - 0.1$ and $\gamma < 0.6$ for the greater Los Angeles area. As our model area is larger and includes an additional, large section of the Sierra Nevada Mts, we first examined two end-member models with $k = 0.075, \gamma = 0$ and $k = 0.1, \gamma = 0.5$, which approximately represent lower and upper bounds of the optimal range found by Hu *et al*. (2022a).

2.6.1 Goodness-of-fit measure

To quantitatively evaluate our trial Q models, we measured the goodness-of-fit (GOF) of the observed and simulated Fourier amplitude spectra (FAS) by computing the natural logarithm of the observation-to-model velocity Fourier amplitude spectral ratios between 0.02 - 3 Hz for all the sites, that is

$$
GOF_{FAS}(f) = \ln\left(\frac{FAS_{obs}(f)}{FAS_{model}(f)}\right), \tag{2.3}
$$

where $FAS_{obs}(f)$ and $FAS_{model}(f)$ are Fourier amplitude spectra of the observed and the simulated velocity waveforms, respectively. Prior to computing the spectral ratio, both $FAS_{obs}(f)$ and $FAS_{model}(f)$ were smoothed using a Savitzky-Golay filter (Savitzky and Golay, 1964) with a 0.5

Hz window length to avoid large fluctuations. After computing GOF_{FAS} separately for all three components at the 161 stations, we computed the mean GOF_{FAS} and the corresponding standard deviation at each frequency to quantify model performance. From the definition of GOF_{FAS}, positive values indicate under-prediction and vice versa. In addition, an error value was computed as a summary of the mean GOF_{FAS} curve over the entire frequency range, defined as

$$Error = \frac{\sum_{i=1}^{N_f} |\mu_i|}{N_f}, \tag{2.4}$$

where μ_i is the mean GOF_{FAS} at frequency point i.

Fig. 2.7 compares the GOF_{FAS} of the two Q models, showing that the model with $k = 0.1$ and $\gamma = 0.5$ produces the least biased result. The differences between two models increases with frequency on all three components, and the GOF_{FAS} effectively distinguishes the two end-member models. Validation using peak ground accelerations (PGAs) confirms the assessment that was obtained using the FAS (Fig. 2.8). Comparison of GOF_{FAS} for different γ values in Fig. 2.9 reveals that values of the power-law exponent γ between 0.4-0.6 all produce reasonable fit to the data. Fig. 2.10 compares GOF_{FAS} for $Q_{S,0}/V_S$ of 0.075 and 0.1 while fixing γ at 0.4, suggesting that $Q_{S,0} = 0.1V_S$ is preferred and better resolved by data than γ.

2.7 Effects on ground motions from the fault zone structure

The calibration of the attenuation model described in Section 2.6 included the CVM, the fault zone structure, and the GTL. We then carried out a series of additional simulations to investigate the individual effects of the fault zone and the GTL. A simulation with the CVM-S ("CVM") without GTL or the damage zone was carried out as a reference model. We then added the Zhou *et al*. (2022) fault zone model to the CVM ("CVM+FZ"), to understand the contribution of the fault zone alone. Finally, a simulation with the CVM and the GTL ("CVM+GTL") was

performed, representing the effects of GTL.

First, we examine the contributions from the fault zone structure and the GTL on the ground motions in the near-source region. Fig. 2.11 compares GOF_{FAS} for models CVM and CVM+FZ in the green box in Fig. 2.1, and it shows that adding the fault zone structure slightly lowers the misfit values on all three components (by $\sim$30%). We can clearly see the contribution of the fault zone at frequencies lower than 0.5 Hz over the GTL. However, a much larger reduction in misfit is obtained by adding the GTL due to the enhancement of spectral energy at frequencies above 0.5 Hz (the CVM+GTL model in Fig. 2.12). Despite the fact that fault zone effects appear small from the GOF_{FAS} perspective, they can be clearly seen in the time domain. In the following, we analyze waveform comparisons between synthetics and data at select stations where the differences are profound, including sites inside (see stations CCC and CLC in Figs. 2.A.3 and 2.A.4) and outside (see stations SLA, WBM, and WVP2 in Figs. 2.A.5 to 2.A.7, respectively) the Zhou *et al*. (2022) imaging domain. When comparing synthetic waveforms for models CVM and CVM+FZ at these stations, it is clear that the fault zone structure improves the modeling of the longer-period features as well as the coda waves in the data, while the comparisons of models CVM+FZ and CVM+FZ+GTL show that the GTL further enhances the high-frequency energy and prolongs the coda wave trains. When comparing the models CVM+FZ and CVM+GTL, stations CCC and WBM in Figs. 2.A.8 and 2.A.9 nicely demonstrate the improvements that the fault zone structure causes in the low frequencies. Our findings suggest that both the fault zone structure and the GTL improve the fit to the data.

Fig. 2.13 demonstrates significant differences in the surface velocity wavefield for the simulations with (CVM+FZ+GTL) and without (CVM+GTL) the fault zone structure. When including the fault zone, the wave fronts exhibit a more complex pattern surrounding the ruptured faults with higher amplitudes compared to the model without the fault zone. The differences can be attributed to waves generated by the velocity contrasts around the faults inherent in the imaged fault zone structure (Fig. 2.A.1). The spatial complexities in the fault zone structure leads

to less coherent wave fronts and longer-lasting wave energy near the causative fault, explaining the prolonged coda wave trains in the synthetic waveforms. The increased particle velocities are found at locations above the near-fault LVZ at 1 km below the surface (see V_S contour in Fig. 2.13a and caption). The snapshots also show that the fault zone amplification effects can propagate away from the near-source region to further distances, sending SH-waves amplified by the near-fault LVZ to the south (see fault-parallel velocity in Fig. 2.13).

Figs. 2.14 and 2.15 clearly illustrate the contributions of both the fault zone and the GTL. The simulation using the original CVM generates the smallest peak-ground velocity (PGV) and peak ground acceleration (PGA) values, where adding the fault zone alone (CVM+FZ) slightly increases the values near the faults, especially the elevated ground motions near the southeastern tip of the fault, caused by the materials with lower wave speeds in the fault zone model. On the other hand, implementing the GTL alone (CVM+GTL) increases both PGVs and PGAs more significantly over a broader area around the northern portion of the fault due to low surface V_S in the China Lake area. The predicted PGVs and PGAs for models CVM+GTL and CVM+FZ+GTL are overall reasonably close. However, one exception is the southeastern end of the fault, where the large observed PGVs and PGAs can only be reproduced by the complete model description (CVM+FZ+GTL), as confirmed by the large velocity pulse in the data at station CI_CCC (see Fig. 2.A.8 for waveform comparison).

Comparison of snapshots from simulations with models CVM+FZ+GTL and CVM+GTL further from the source shows additional evidence that the fault zone generates a more complicated wavefield, as the trapped waves generated within the LVZ continue to contribute wave energy after the termination of the source rupture (see Fig. 2.16). The surface wave trains with amplitude and duration amplified by the LVZ can be seen at distances along the paths to the Ventura basin and to the eastern parts of the Los Angeles basin. The snapshots also reveal that the fault zone increases the coda duration in the synthetic time series (Figs. 2.A.10 to 2.A.15). A record section of synthetic velocity time series between the epicenter and station GOU clearly differentiates the

model with and without the fault zone in terms of the ability to generate strong surface waves (indicated by the dashed line) present in the data (Fig. 2.18). While the fault zone structure does not significantly impact the PGAs, the PGVs are notably increased within the Los Angeles basin Fig. 2.17.

2.8 Discussion and conclusions

We have performed 0-3 Hz 3D deterministic wave propagation simulations of the 2019 M_w 7.1 Ridgecrest, CA earthquake in a 200 km x 300 km domain and estimated the parameters k and γ for $Q_S(f) = Q_{S,0} f^{\gamma}$, where $Q_{S,0} = kV_S$. Constrained by the data recorded by dense deployments of seismic stations, we first used FAS GOF (GOF_{FAS}) to estimate the optimal parameters for $Q(f)$, and we find that $k = 0.1$ and $\gamma = 0.5$ best explain the observations. $k = 0.1$ is consistent with the low-frequency Q models estimated by Olsen *et al*. (2003), Olsen *et al*. (2009), Savran and Olsen (2019), Pitarka *et al*. (2021), Withers *et al*. (2015), Hu *et al*. (2022a), and Hu *et al*. (2022b), and the $Q(f)$ model is within the range determined by Hu *et al*. (2022a). Furthermore, the range of γ estimated in this study is similar to those from seismic observations in southern California. For example, our results are in agreement with the inverted value of 0.4 from the study by Lin and Jordan (2018) using P and S waves spectra, $0.5 \leq \gamma \leq 0.8$ from Song and Jordan (2013) constrained by local earthquake data when considering elastic scattering, and $\gamma = 0.45$ by Raoof *et al*. (1999) obtained from fitting the spectra of earthquake ground motion records.

Using the calibrated $Q(f)$ model, we analyzed the effects of the fault zone model on strong ground motions during the 2019 M_w 7.1 Ridgecrest earthquake. Our analysis shows that the fault zone model perturbs the predicted ground motions in both near-source and far-field regions. For the entire region, the fault zone model primarily improves the fit to the data between 0.1-0.3 Hz, reducing the envelope misfit (Kristeková *et al*., 2006; Kristeková *et al*., 2009) by 10-15% on all three components (Fig. 2.19). When considering the SCEC CVM-S as reference, our

simulations indicate that the fault zone structure improves modeling of the long-period features in the data and lengthens the coda wave trains in better agreement with observations. The presence of the fault zone structure generates trapped waves and increases near-source ground motions, which is consistent with earlier findings (Ben-Zion and Aki, 1990; Peng and Ben-Zion, 2006; Li and Leary, 1990; Ben-Zion *et al*., 2003; Lewis *et al*., 2005).

The addition of a calibrated GTL was the model feature that most significantly improved the spectral energy toward the observed level over a broad frequency range, as compared to the effects of the fault zone model by Zhou *et al*. (2022). However, even though the fault zone generates weaker effects on the ground motions in the FAS domain as compared with those from the GTL, the former generates unique signatures in the time domain. We therefore conclude that including both the fault zone structure and the GTL reduce the misfit between data and synthetics.

Acknowledgements

This research was supported through the Southern California Earthquake Center (SCEC; Contribution Numbers 20157 and 21111). SCEC is funded by the National Science Foundation (NSF) Cooperative Agreement EAR-1600087 and the U.S. Geological Survey (USGS) Cooperative Agreement G17AC00047.

Chapter 2, in full, is a reformatted version of a paper currently in preparation for submission for publication: Yeh, T.-Y. and Olsen, K.B. (2022), Fault damage zone effects on ground motions during the 2019 M_w 7.1 Ridgecrest, CA, earthquake. The dissertation author was the primary investigator and author of this paper.

Tables and Figures

Table 2.1: Simulation domain

Domain		
Length		200.87 km
Width		304.55 km
Depth		149.61 km
Southwest corner		$-119.50000^o, 34.00000^o$
Northwest corner		$-118.14120^o, 36.50876^o$
Southeast corner		$-117.52448^o, 33.25866^o$
Northeast corner		$-116.11682^o, 35.74564^o$
Spatial resolution		
Grid spacing	15 m	Free surface to 11.97 km below sea level
	45 m	11.87 to 24.78 km below sea level
	135 m	24.47 to 149.61 km below sea level
Maximum frequency		3 Hz
Minimum V_S		300 m/s
Points per minimum wavelength		6.66
Temporal resolution		
Time step		0.0008 s
Simulation time		180 s
MISC		
Geotechnical tapering depth		700 m

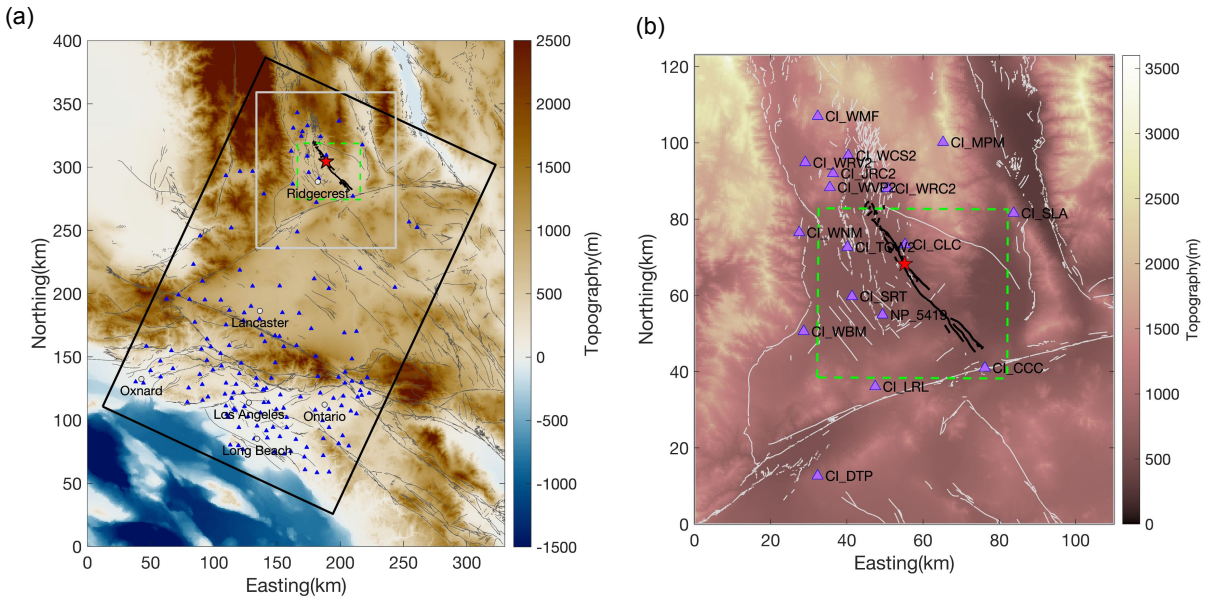

Figure 2.1: (a) Model domain (black rectangle) for the simulations. Blue triangles show locations of stations providing seismic recordings of the 2019 Ridgecrest M_w 7.1 earthquake. The green dashed box depicts the domain where the fault zone structure was imaged by Zhou *et al*. (2022). Thick black traces are faults that ruptured in the 2019 M_w 7.1 Ridgecrest earthquake. (b) Near-source region inside the gray square in (a), where purple triangles show the locations of stations used for analysis of near-source ground motions.

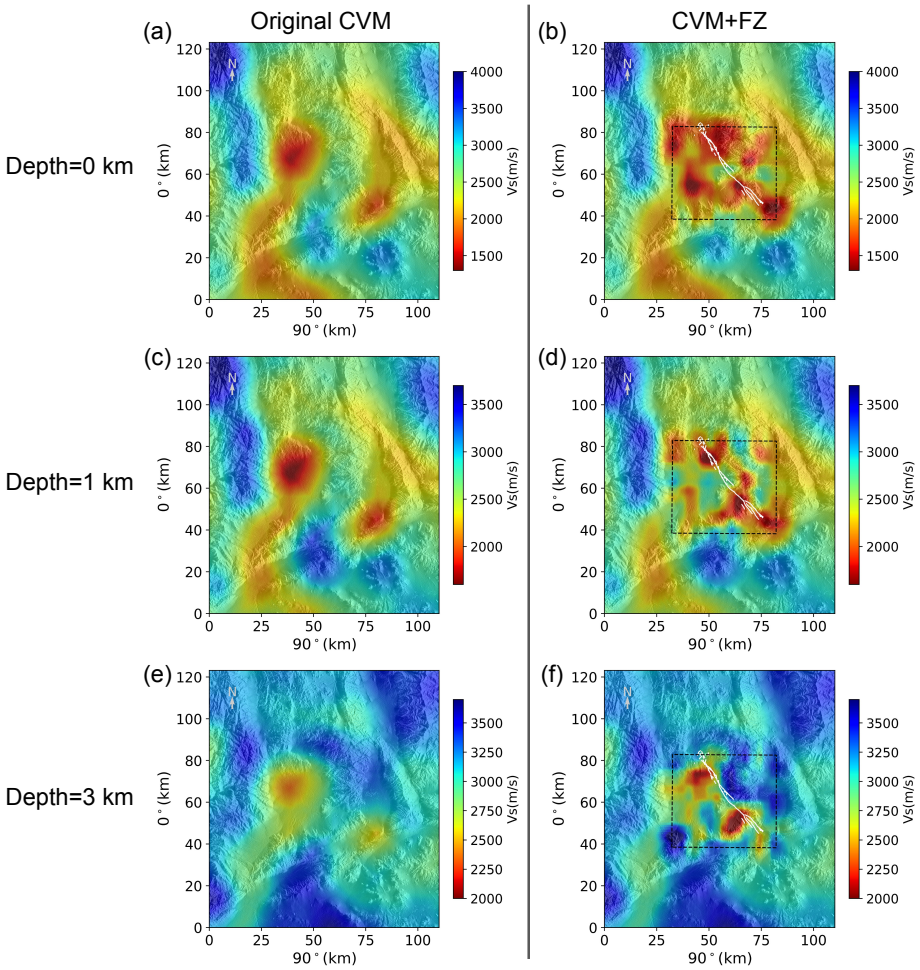

Figure 2.2: Comparison of horizontal slices of V_S inside the region shown by Fig. 2.1b at different depths without (left column) and with (right column) incorporating the fault zone structure. The black dashed box depicts the imaging domain of the fault zone model. Note that the slices do not include the GTL.

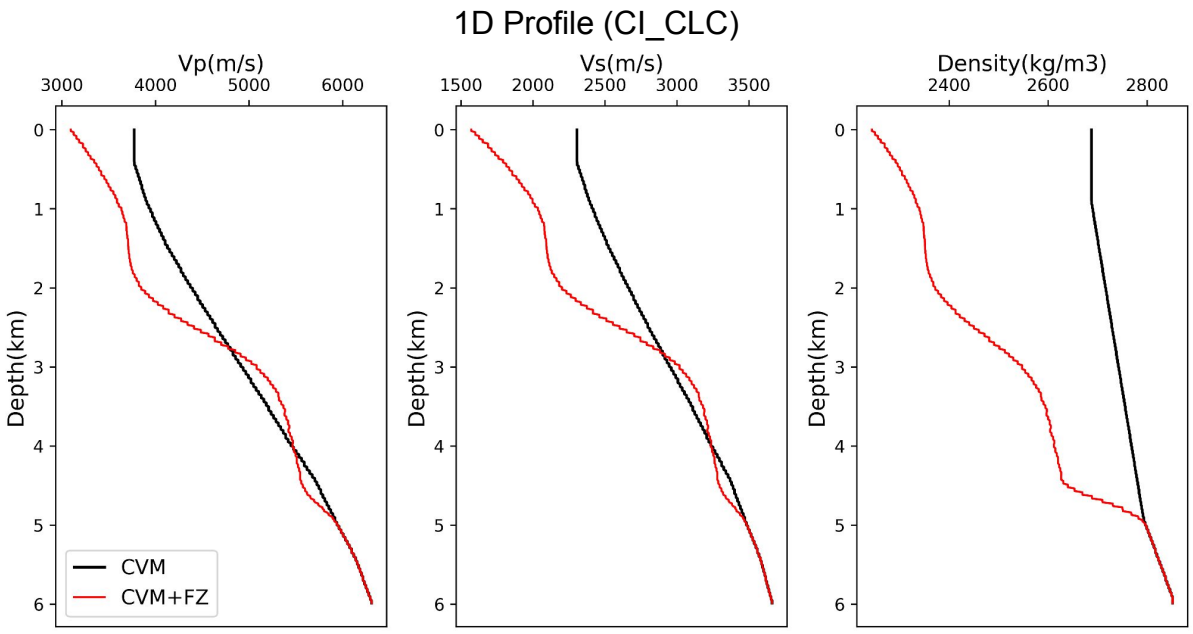

Figure 2.3: Comparison of V_S profiles beneath station CLC which is inside the fault zone imaging domain (see Fig. 2.1b for location). The black curves show the model with CVM-S, and red traces depict the model including the fault zone structure.

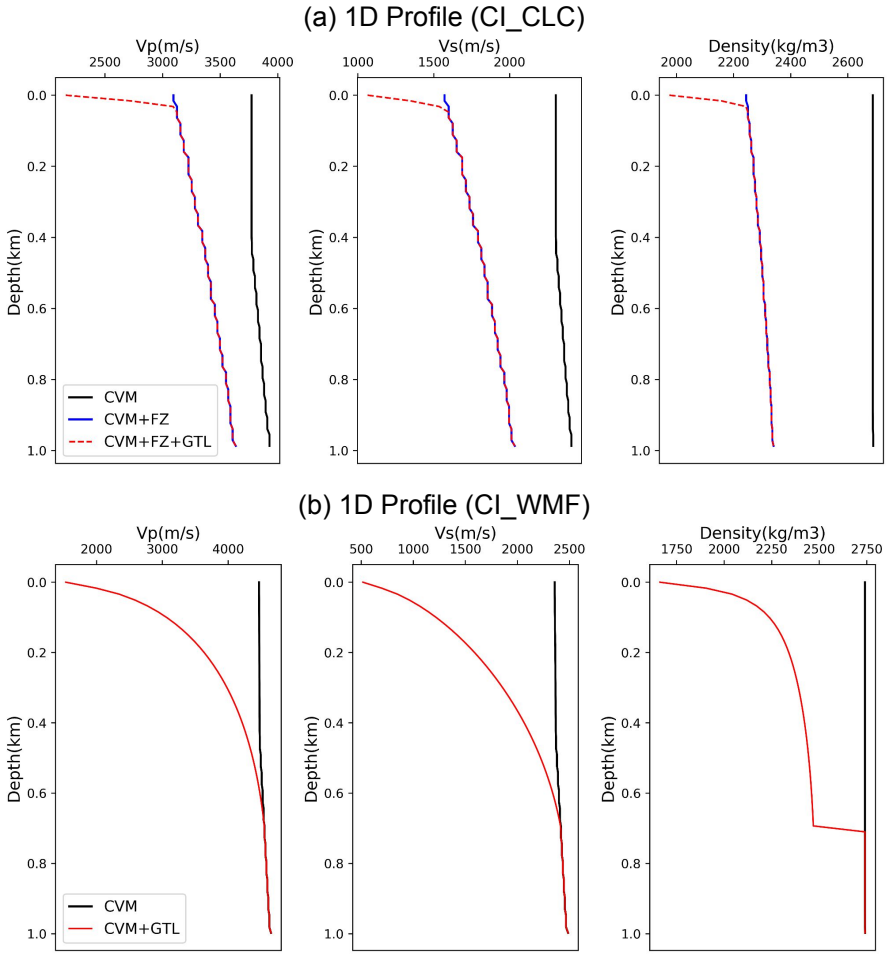

Figure 2.4: Near-source profiles (0 - 1 km) after implementation of the GTL beneath station CLC (top) and WMF (bottom) which are inside and outside the fault zone imaging domain, respectively. See Fig. 2.1b for locations.

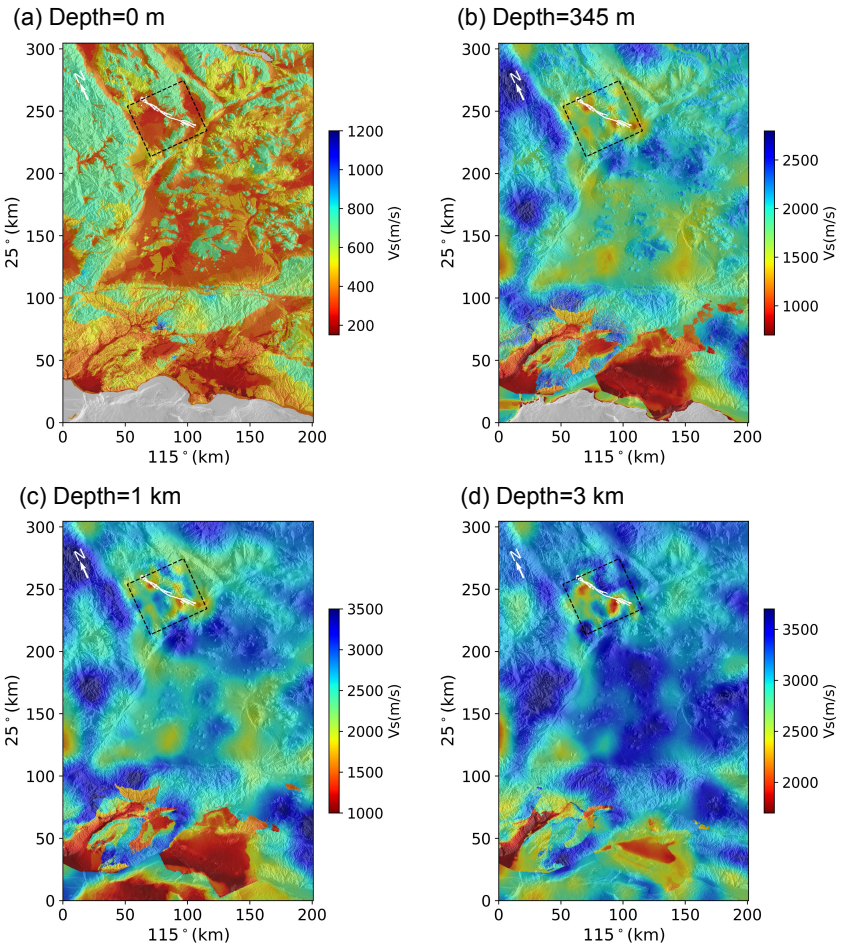

Figure 2.5: V_S slices in the modeling domain (black rectangle in Fig. 2.1a) at different depths, including the fault zone structure and the GTL. The black dashed box depicts the imaging domain of the fault zone.

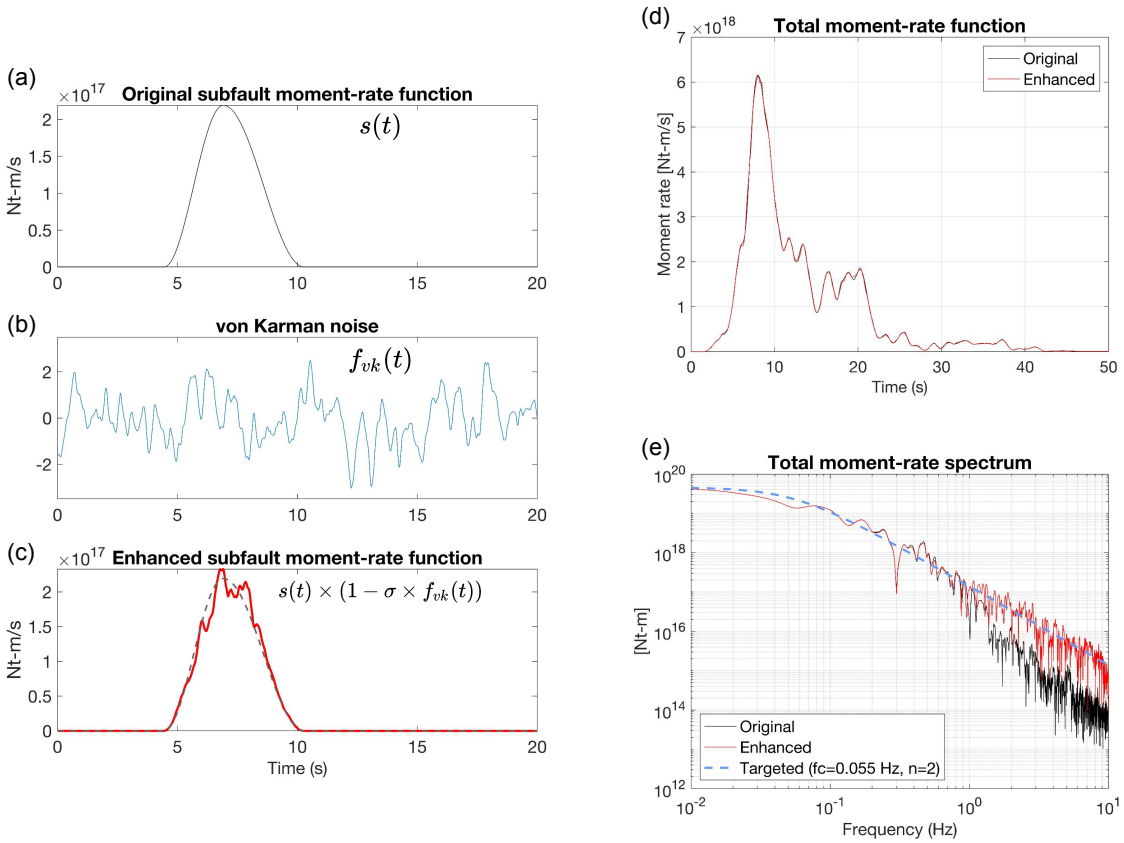

Figure 2.6: Enhancement of spectral energy for the source model from the kinematic source inversion. (a) Moment-rate function for one subfault. (b) Von Karman correlated noise with correlation length of 0.1138 s. (c) Perturbed slip-rate function with $\sigma = 0.1$. (d) and (e) compare the total moment-rate functions in the time and the frequency domain, respectively. Targeted total moment-rate spectrum is shown by the blue dashed curve in (e).

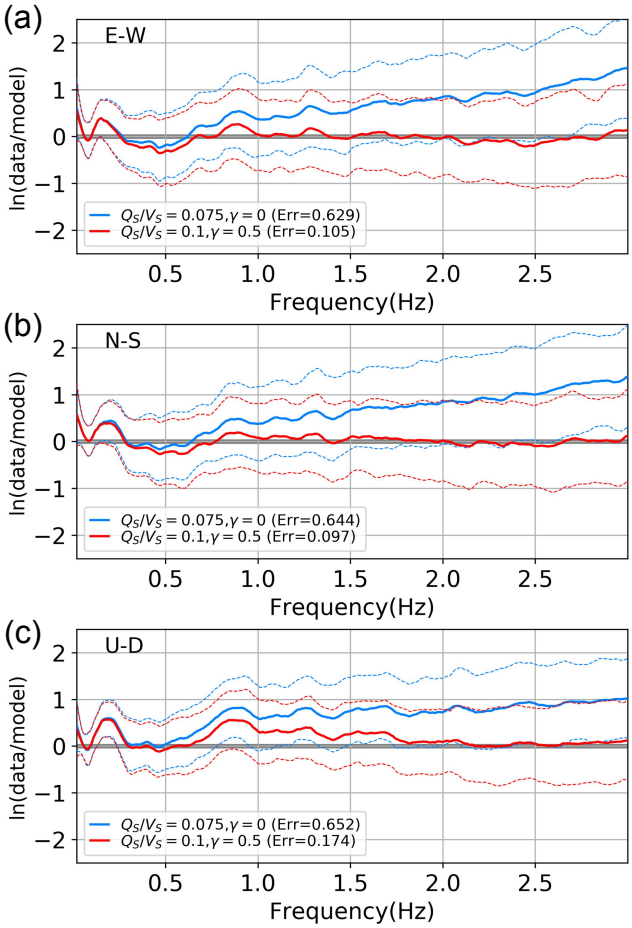

Figure 2.7: Comparison of FAS GOF for simulations with two end-member Q models, namely (blue) $k = 0.075$, $\gamma = 0$, and (red) $k = 0.1$, $\gamma = 0.5$, including the fault zone. Thick solid curves depict the mean GOF_{FAS}, and dashed lines show the corresponding standard deviation.

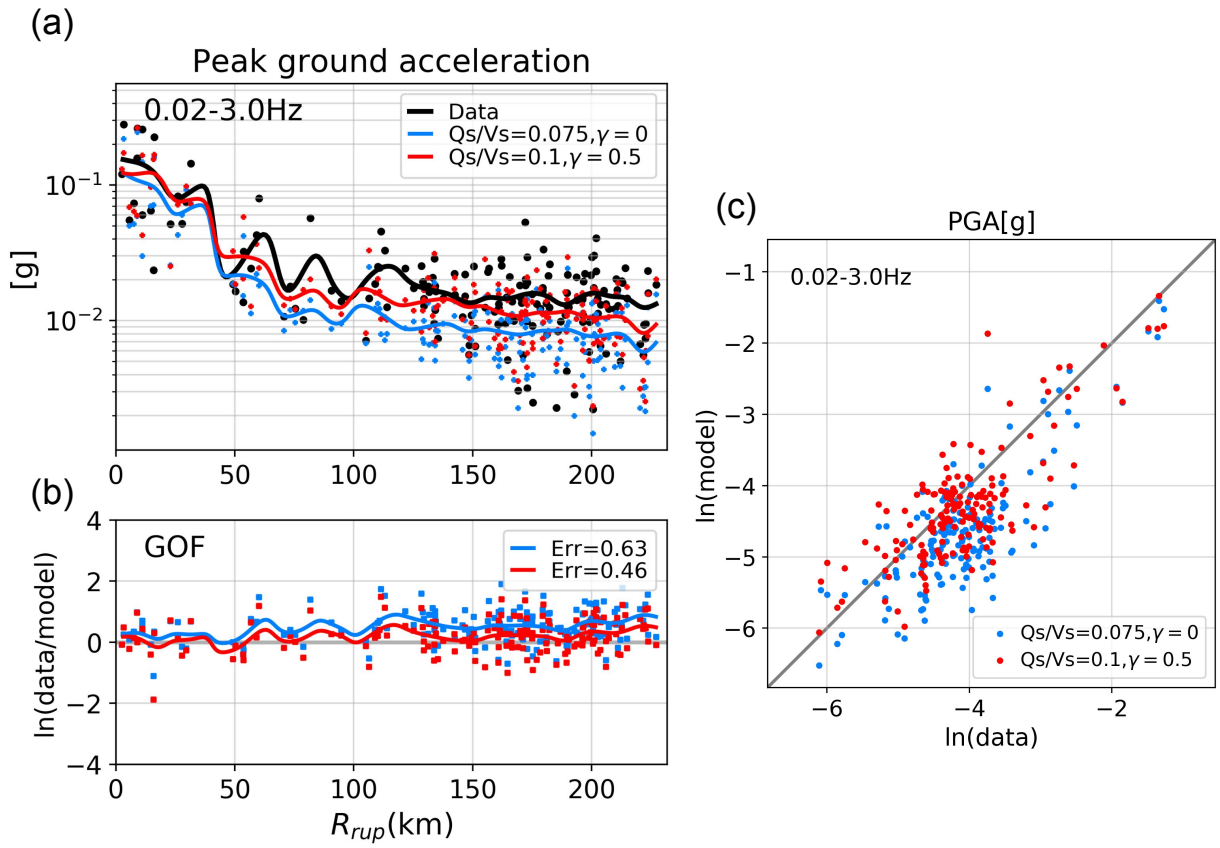

Figure 2.8: Comparison of simulated PGAs for Q models with (blue) $Q_S = 0.075 V_S f^0$ and (red) $Q_S = 0.1 V_S f^{0.5}$ against data within 0.02-3 Hz. (a) PGVs as a function of shortest distance to the fault (R_{rup}). (b) Data-to-model ratio as a function of R_{rup}. (c) Scatter plot of observed versus simulated values (natural logarithmic scale). Thick lines in (a) and (b) are Gaussian-weighted averages of the corresponding data points with $\sigma = 5$ km.

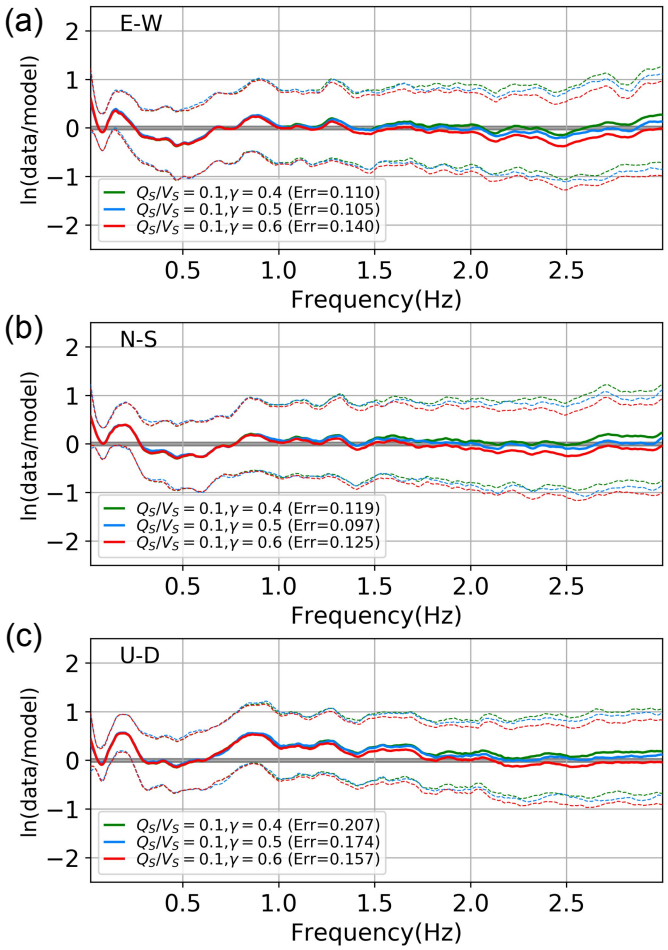

Figure 2.9: Comparison of FAS GOF for simulations including the fault zone and Q models with $k = 0.1$ and γ=0.4 (green), 0.5 (blue), and 0.6 (red). Thick solid curves depict the mean GOF_{FAS}, and dashed lines show the corresponding standard deviation.

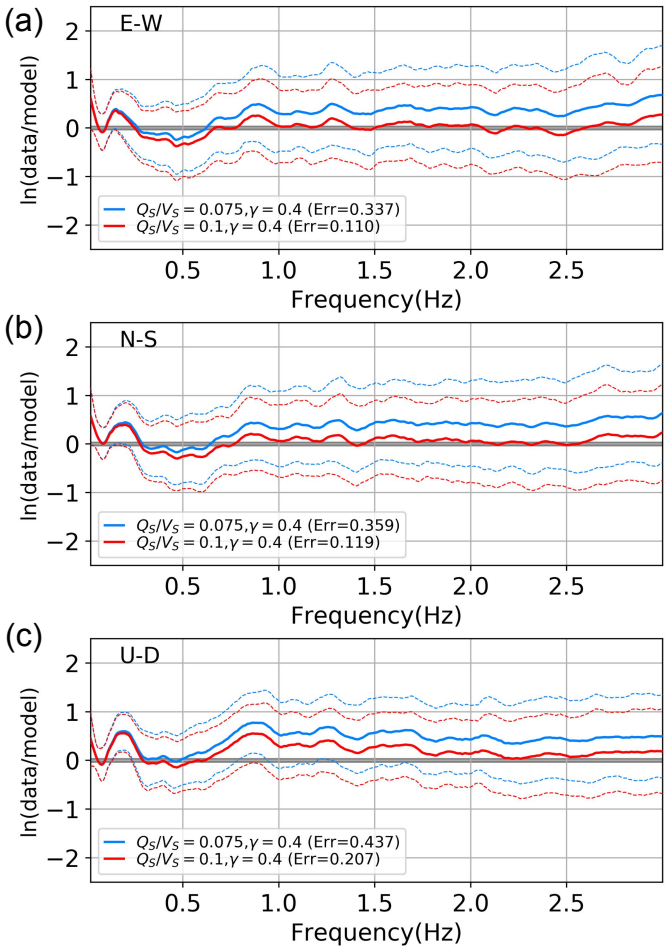

Figure 2.10: Comparison of FAS GOF of simulations with $Q_{S,0} = 0.075V_S$ and $Q_{S,0} = 0.1V_S$ with $\gamma = 0.4$. Thick solid curves depict the mean GOF_{FAS}, and dashed lines show the corresponding standard deviation.

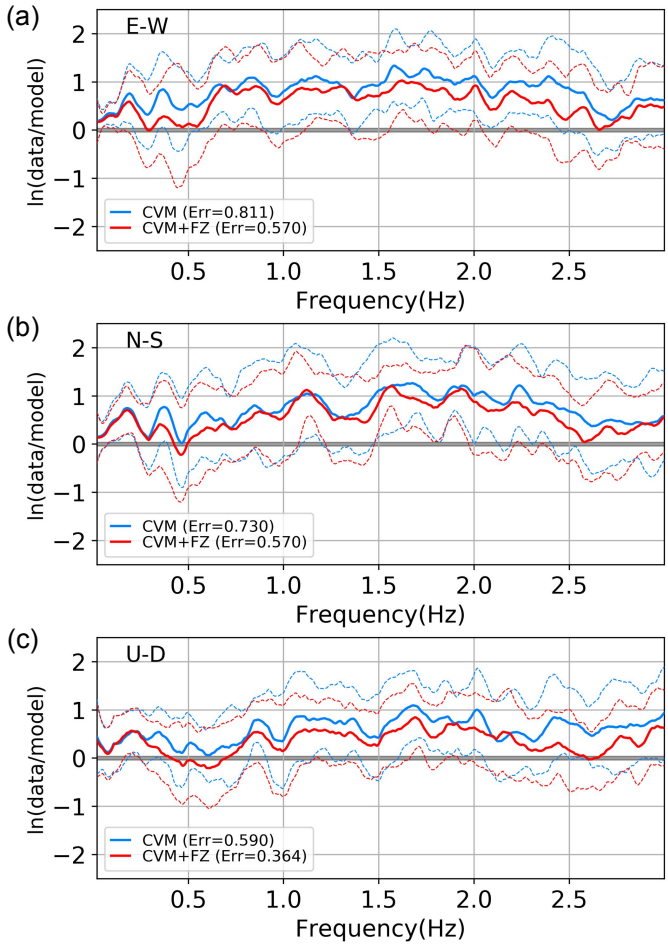

Figure 2.11: Comparison of FAS GOF for simulations with (blue) CVM and (red) CVM+FZ. Thick solid curves depict the mean GOF_{FAS}, and dashed lines show the corresponding standard deviation.

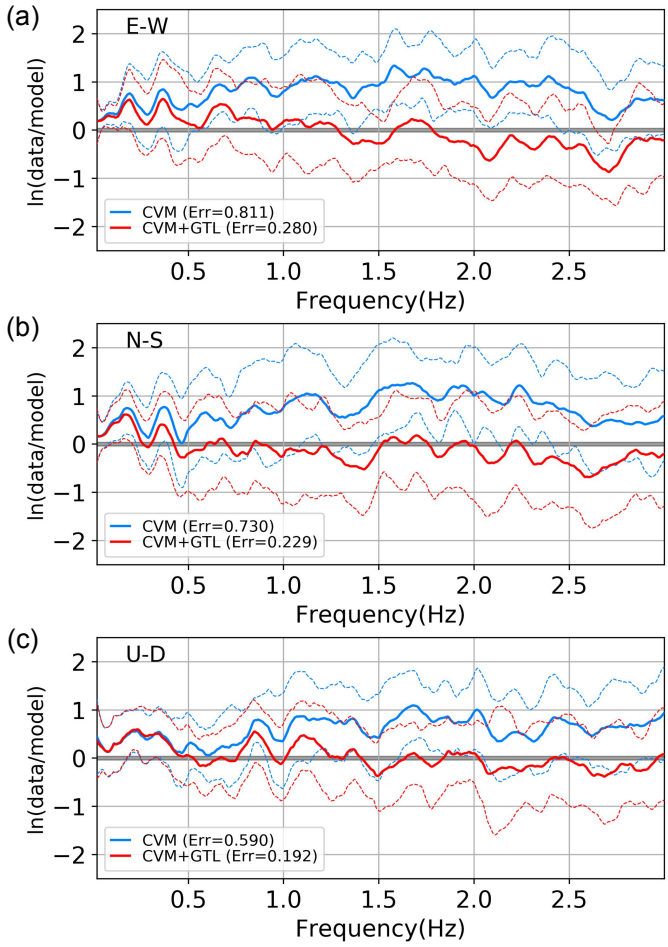

Figure 2.12: Same as Fig. 2.11, but for simulations with (blue) CVM and (red) CVM+GTL.

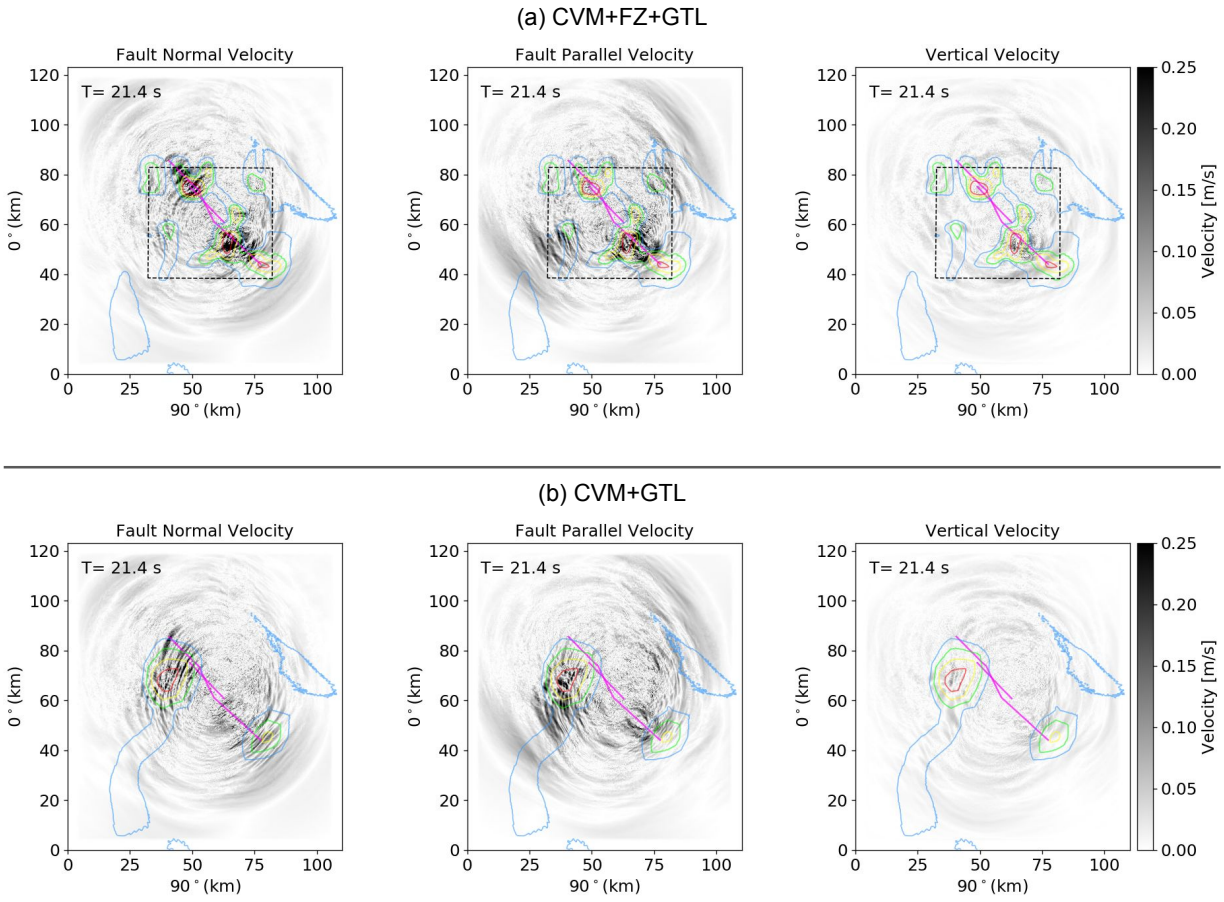

Figure 2.13: Snapshots of absolute particle velocity along (left) fault normal, (center) fault parallel and (right) vertical directions in the near-fault region (Fig. 2.1b) for simulations with (top) CVM+ GTL and (bottom) CVM+FZ+GTL. The magenta lines depict the fault trace used for simulating the M7.1 Ridgecrest event. Red, yellow, green and blue contour lines depict contours for V_S of 1700, 1900, 2100, and 2300 m/s, respectively, at 1 km below free surface in the corresponding models.

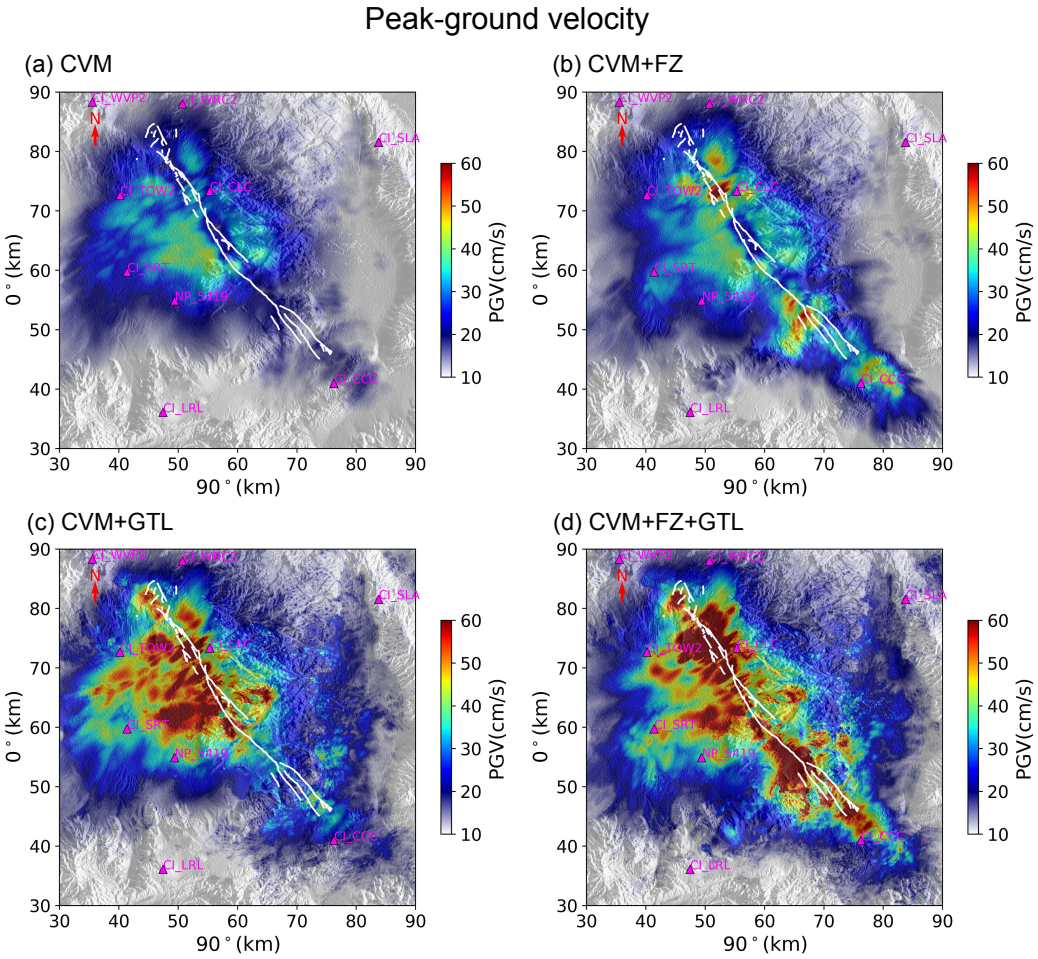

Figure 2.14: PGVs in the near-fault region (see Fig. 2.1b for location) for models (a) CVM, (b) CVM+FZ, (c) CVM+GTL, and (d) CVM+FZ+GTL. White lines depict fault traces used for the simulation of the M7.1 Ridgecrest event.

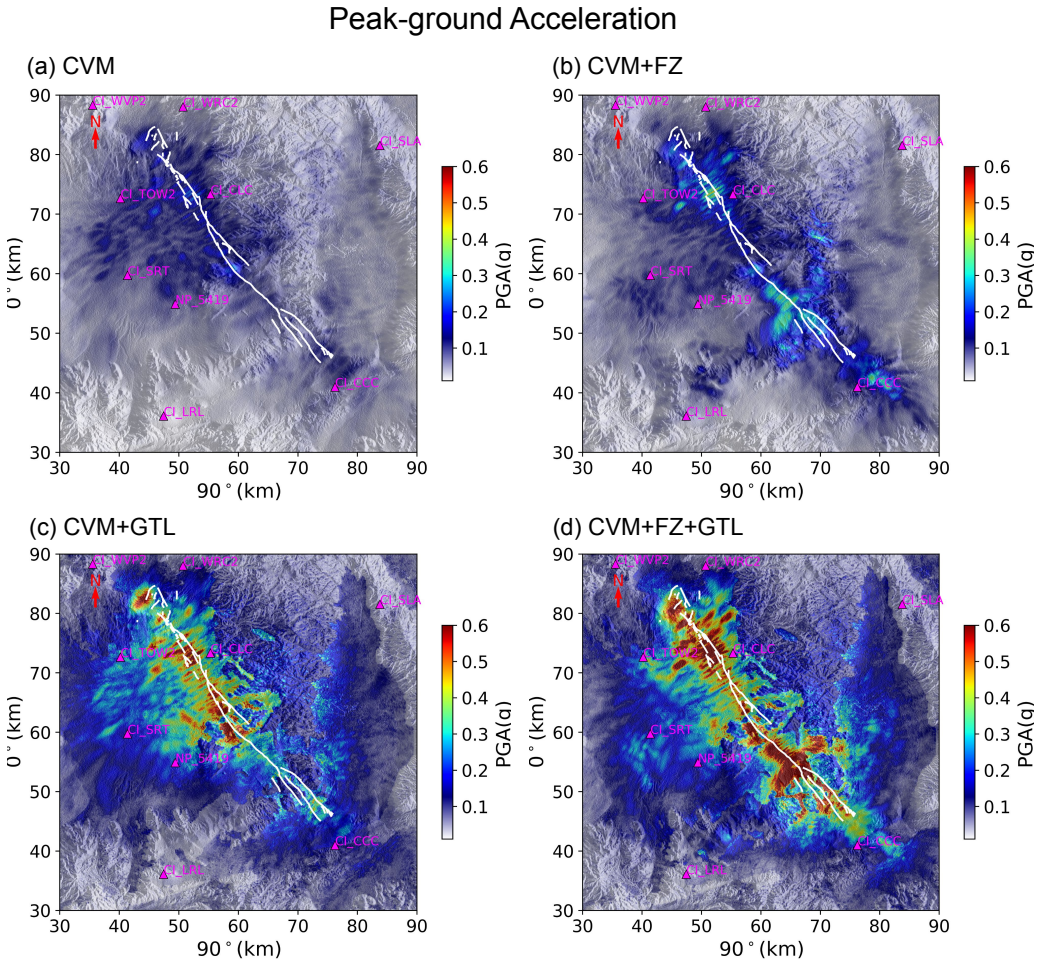

Figure 2.15: Same as Fig. 2.14, but for PGA.

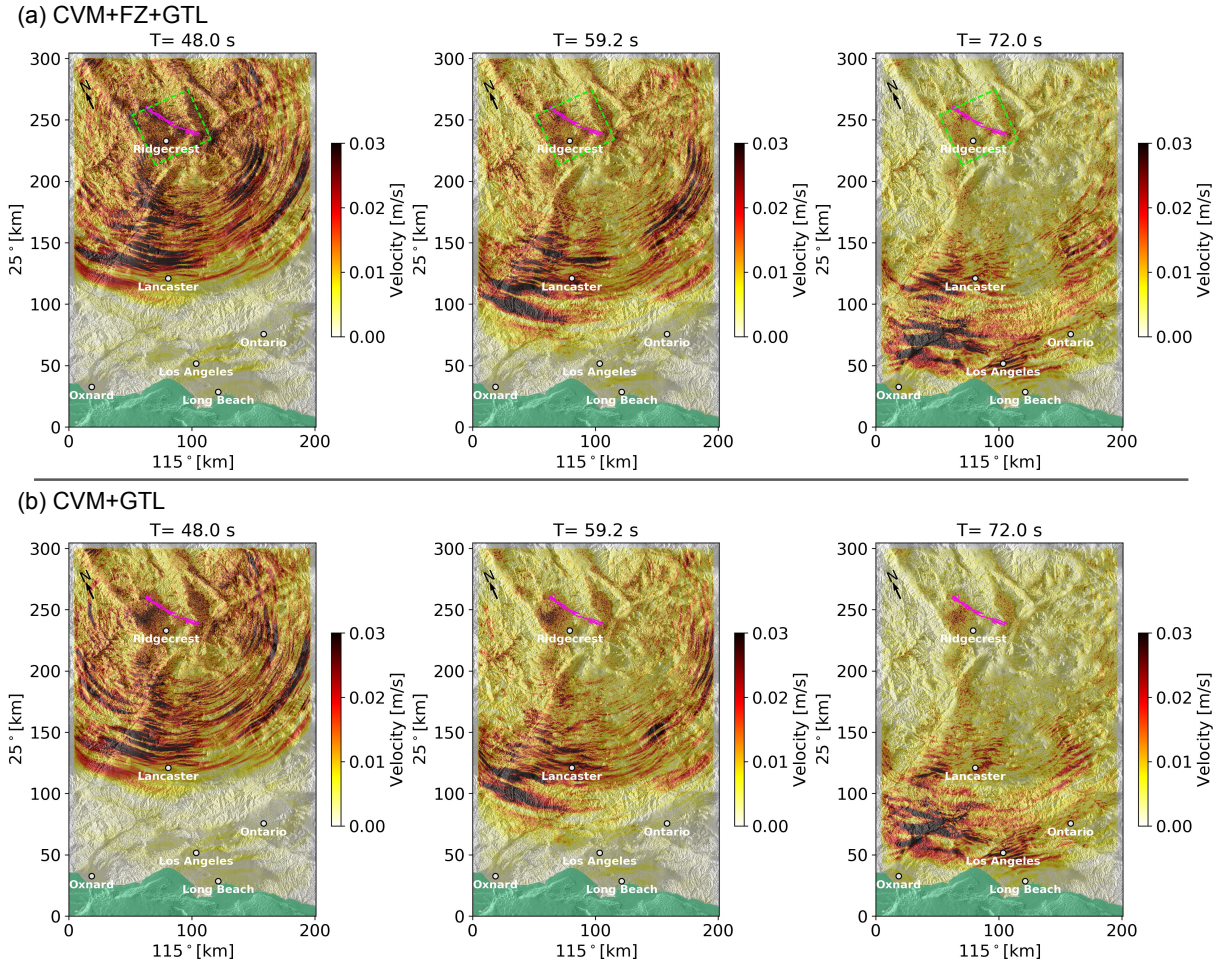

Figure 2.16: Snapshots of norm of particle velocity (a) with and (b) without the fault zone model. The green dashed box is the domain where the fault zone structure was imaged.

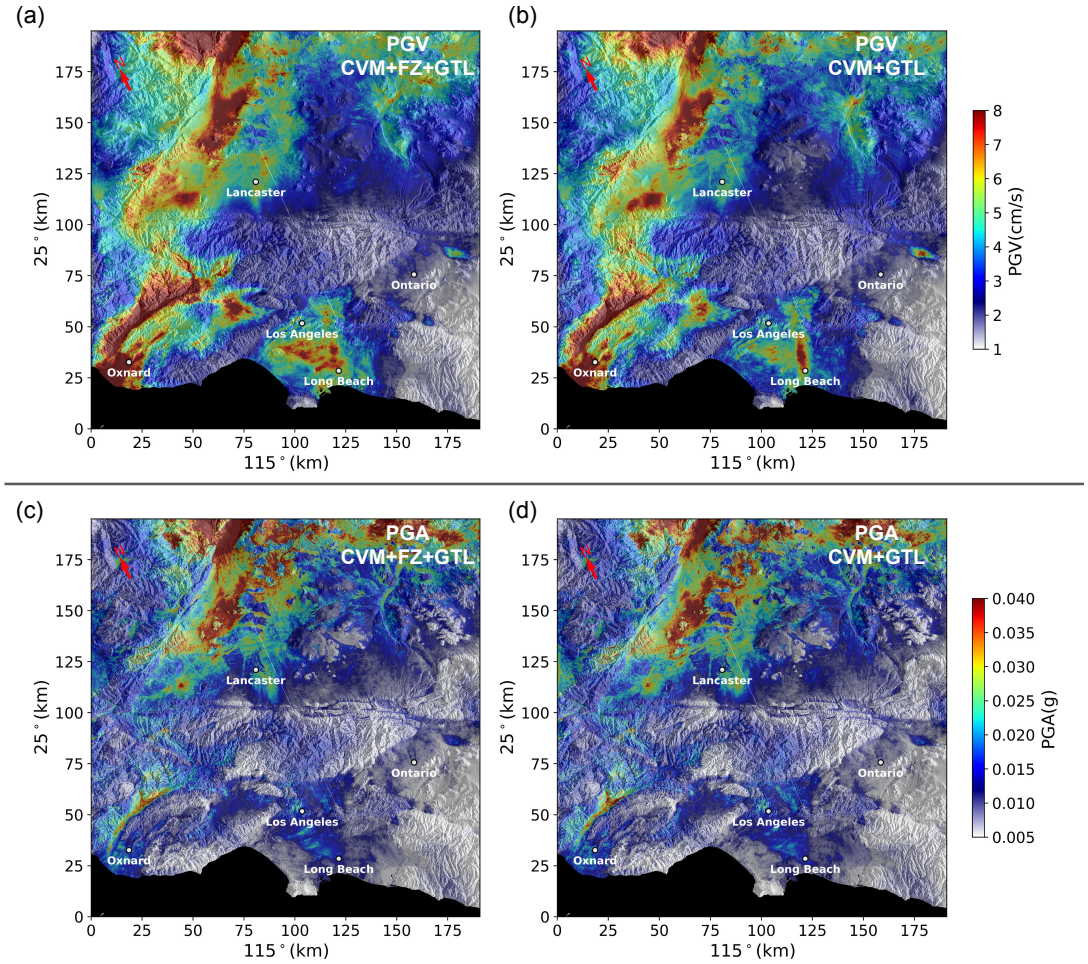

Figure 2.17: PGVs (top row) and PGAs (bottom row) in the southern portion of the simulation domain with (left column) and without (right column) the fault zone structure included.

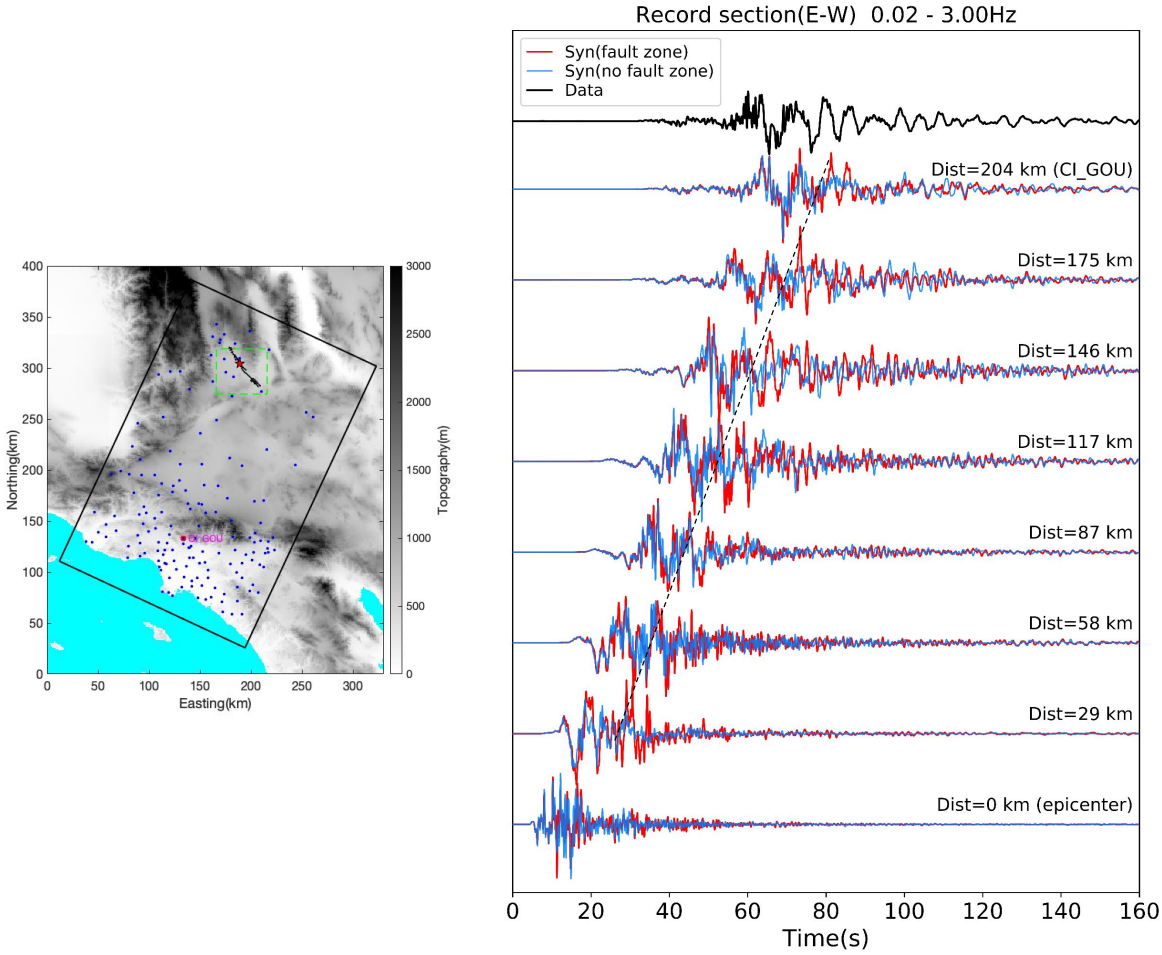

Figure 2.18: Record section of the E-W component of synthetic velocity waveforms computed (red) with and (blue) without the fault zone, as compared with the data at station GOU (see map on the left for location). The synthetics are normalized by the maximum amplitude of the waveforms computed with the fault zone. The dashed line indicates a wave speed of ~ 3.2 km/s.

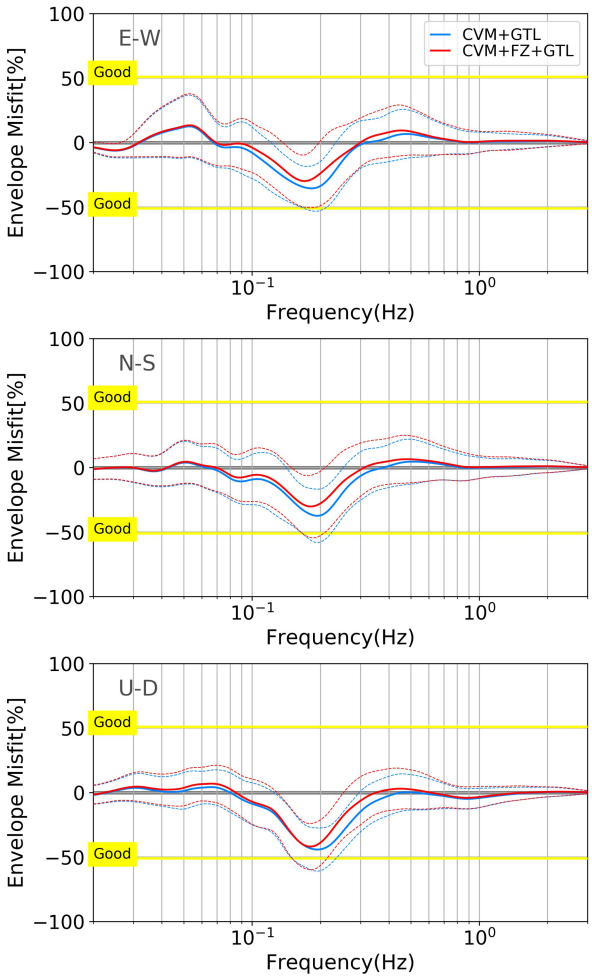

Figure 2.19: Three-component envelope misfit between simulations (red) with and (blue) without the fault zone and data at frequencies between 0.02 - 3 Hz, computed using the TF-misfit package by Kristeková *et al*. (2006) and Kristeková *et al*. (2009). The yellow lines mark the range of good fit to data, as described in Kristeková *et al*. (2009).

Appendix

2.A Appendix to Chapter 2

2.A.1 Supplementary figures for Chapter 2

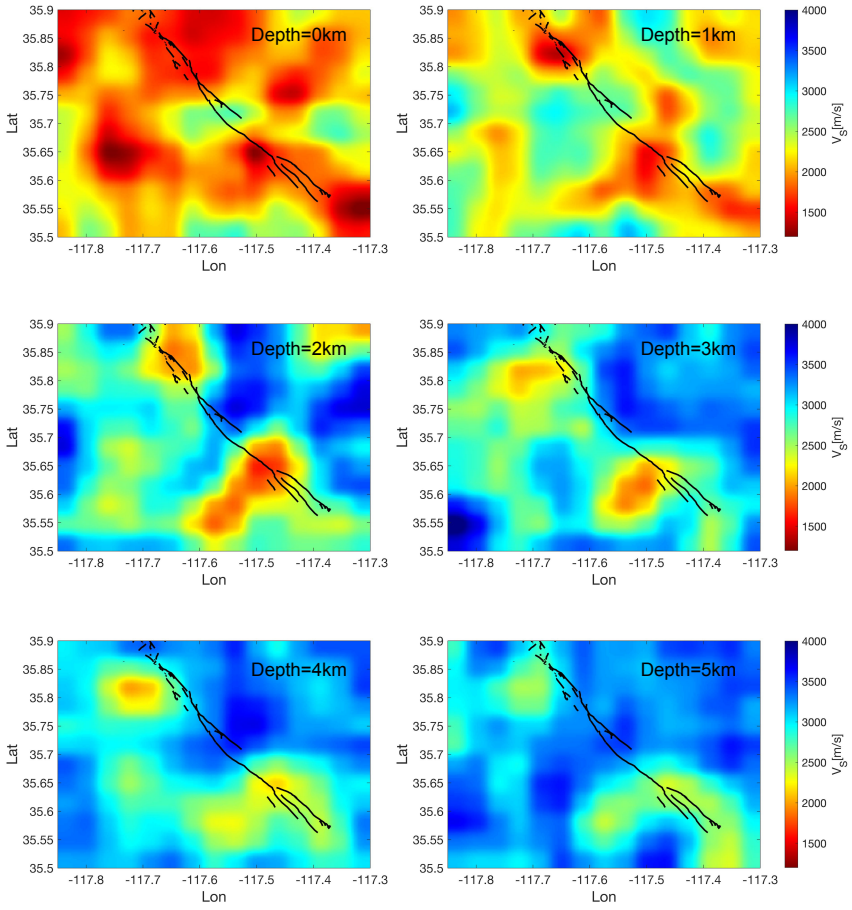

Figure 2.A.1: V_S slices from 0 - 5 km depth below the surface in the fault zone model imaged by Zhou *et al*. (2022). Black traces depict the surface rupture of the faults that ruptured during the 2019 M_w 7.1 Ridgecrest event.

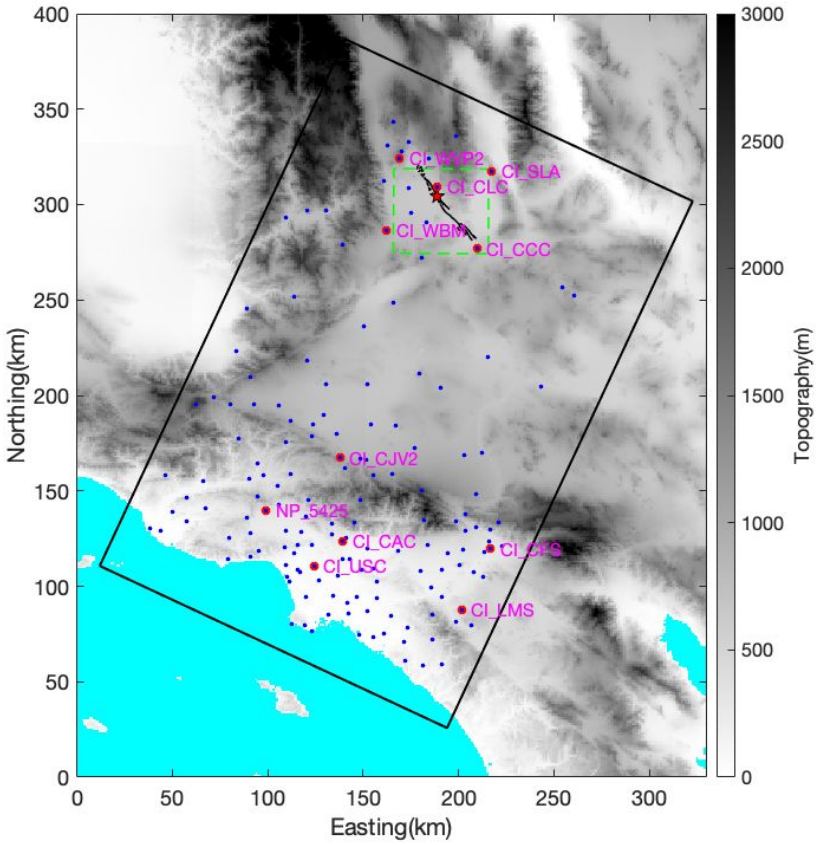

Figure 2.A.2: Map showing station locations. Red circles with station names depict stations used for waveform comparisons. Green dashed box shows the domain where the fault zone structure was imaged.

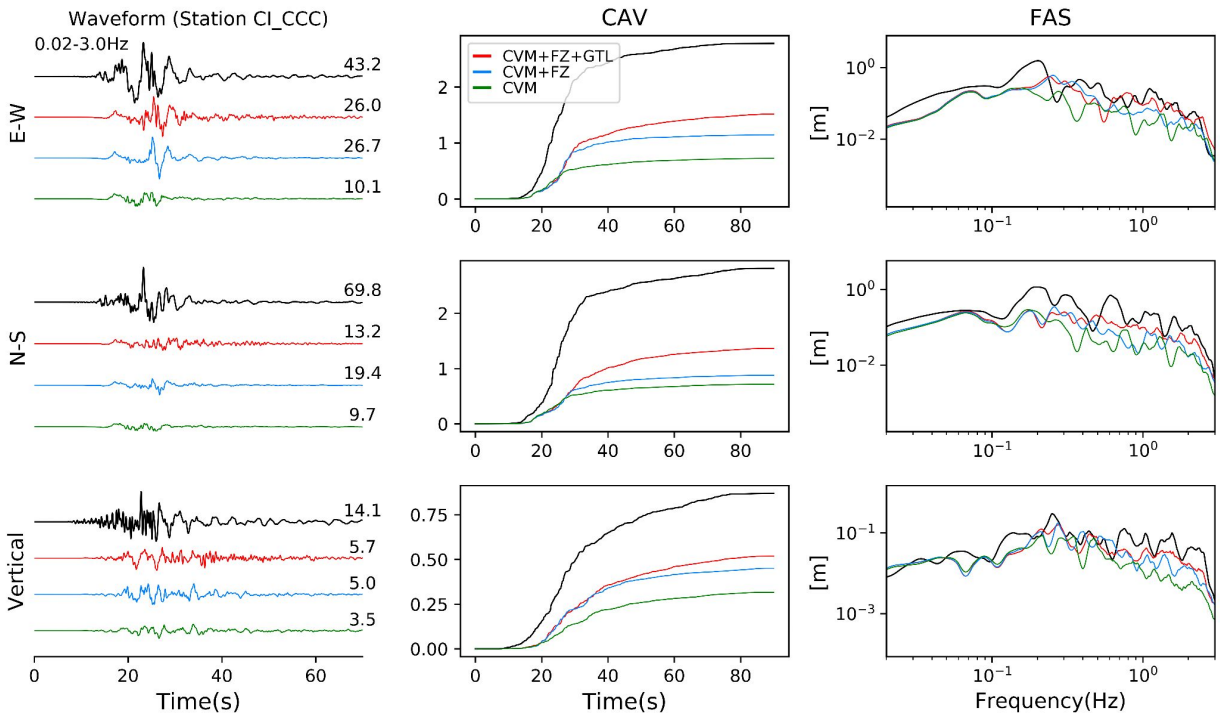

Figure 2.A.3: Comparison of observed and simulated (left) waveforms, (center) CAV, and (right) FAS for station CCC (see Fig. 2.1b for location). The data shown by black traces are compared with simulations with (red) CVM+FZ+GTL, (blue) CVM+FZ, and (green) CVM.

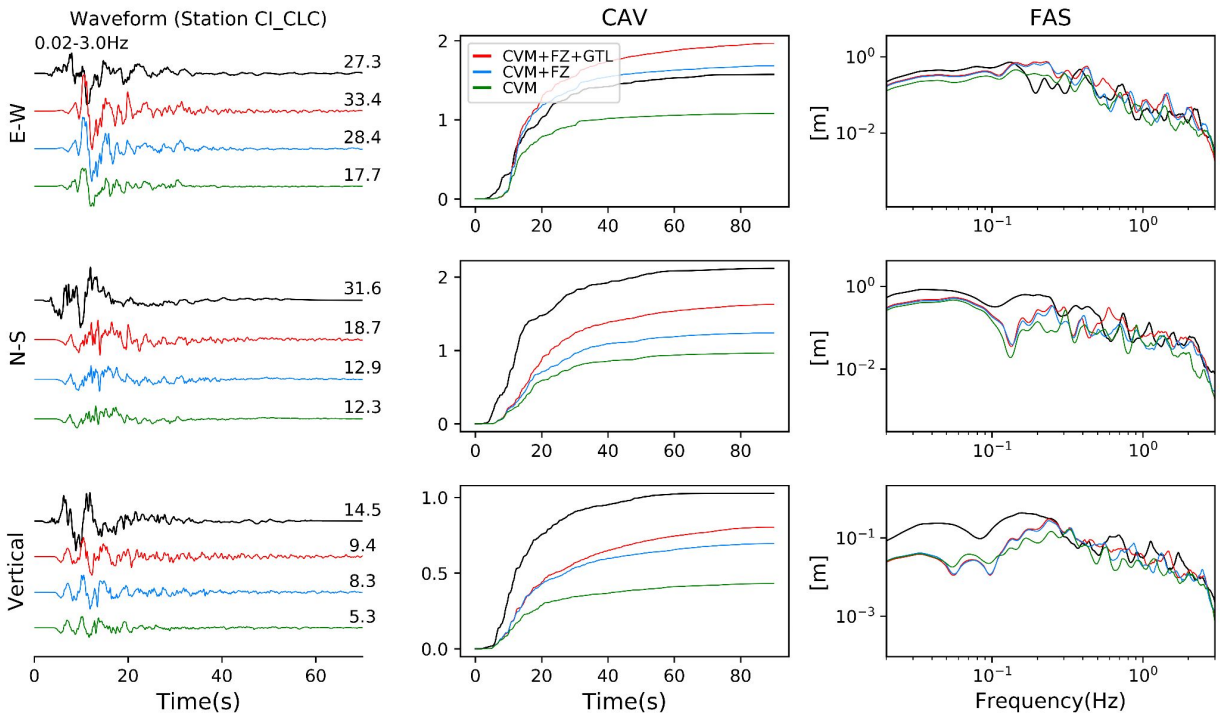

Figure 2.A.4: Same as Fig. 2.A.3, but for station CLC (see Fig. 2.1b for location).

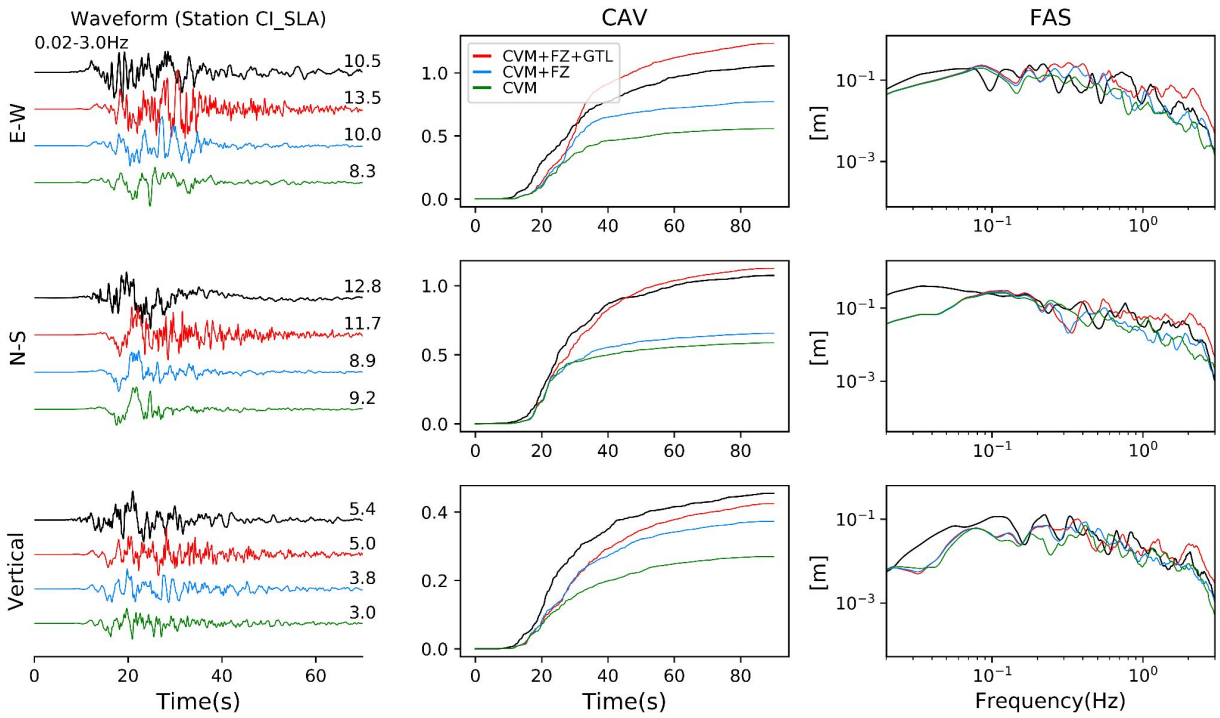

Figure 2.A.5: Same as Fig. 2.A.3, but for station SLA (see Fig. 2.1b for location).

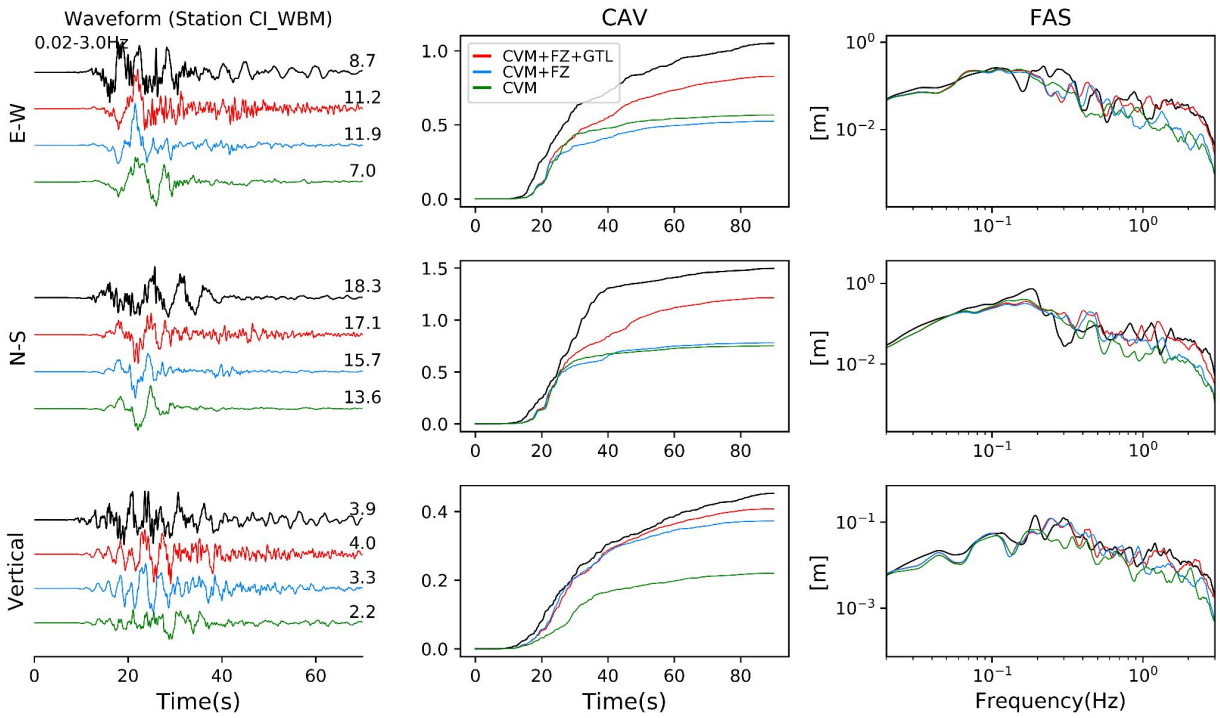

Figure 2.A.6: Same as Fig. 2.A.3, but for station WBM (see Fig. 2.1b for location).

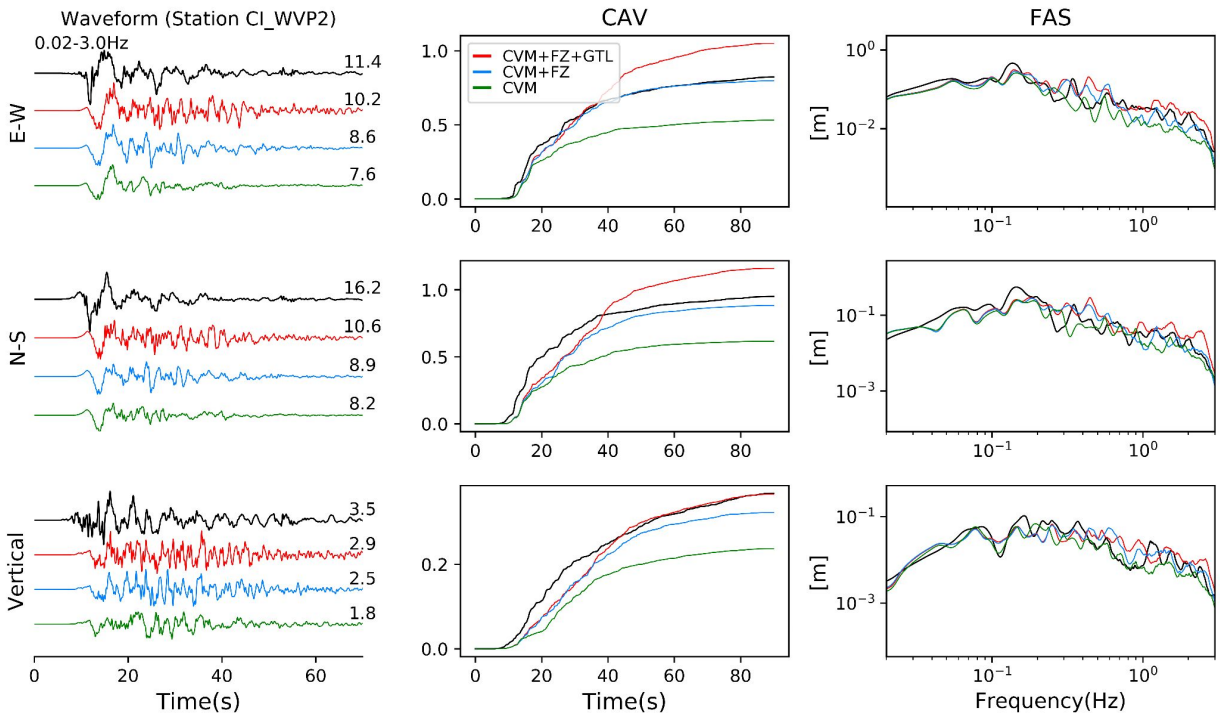

Figure 2.A.7: Same as Fig. 2.A.3, but for station WVP2 (see Fig. 2.1b for location).

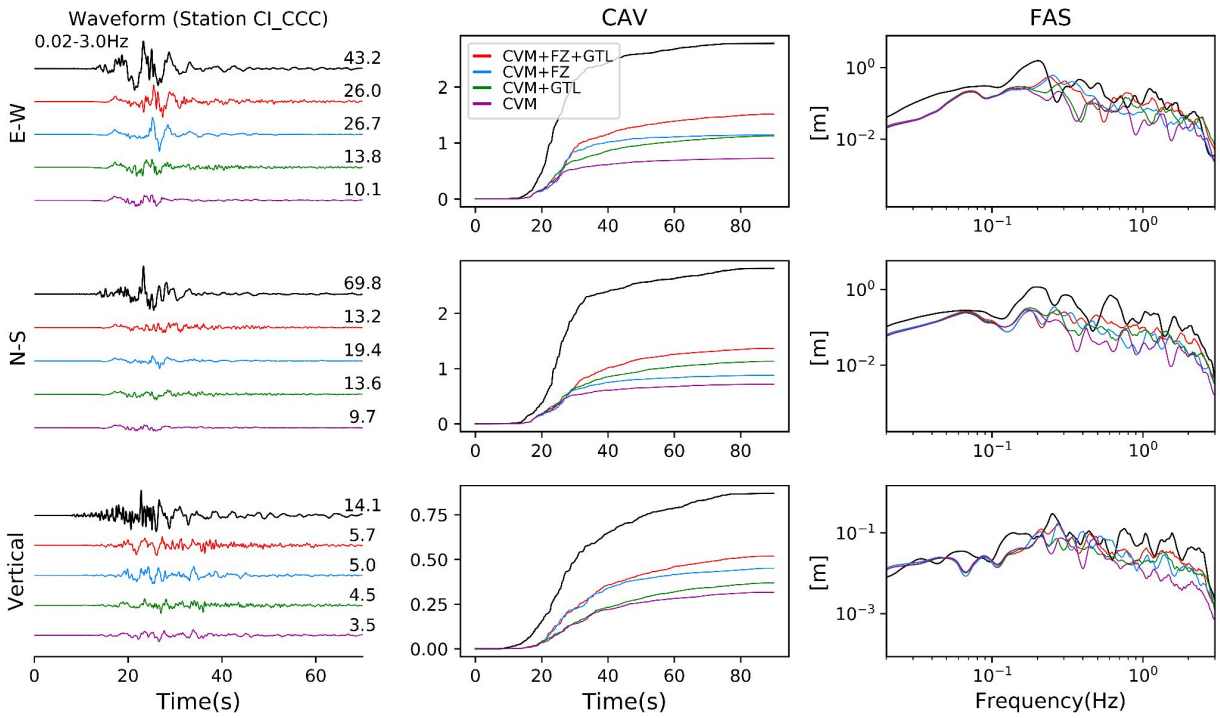

Figure 2.A.8: Same as Fig. 2.A.3, but adding the CVM+GTL model into the comparison.

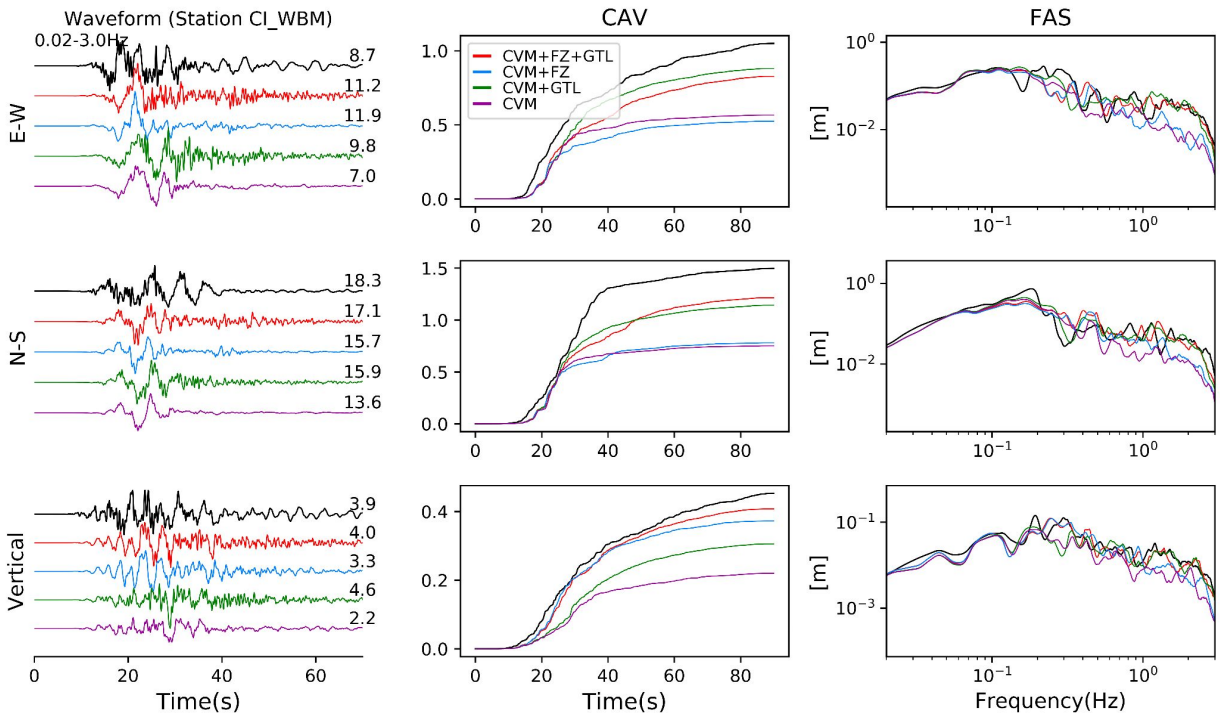

Figure 2.A.9: Same as Fig. 2.A.6, but adding the CVM+GTL model into the comparison.

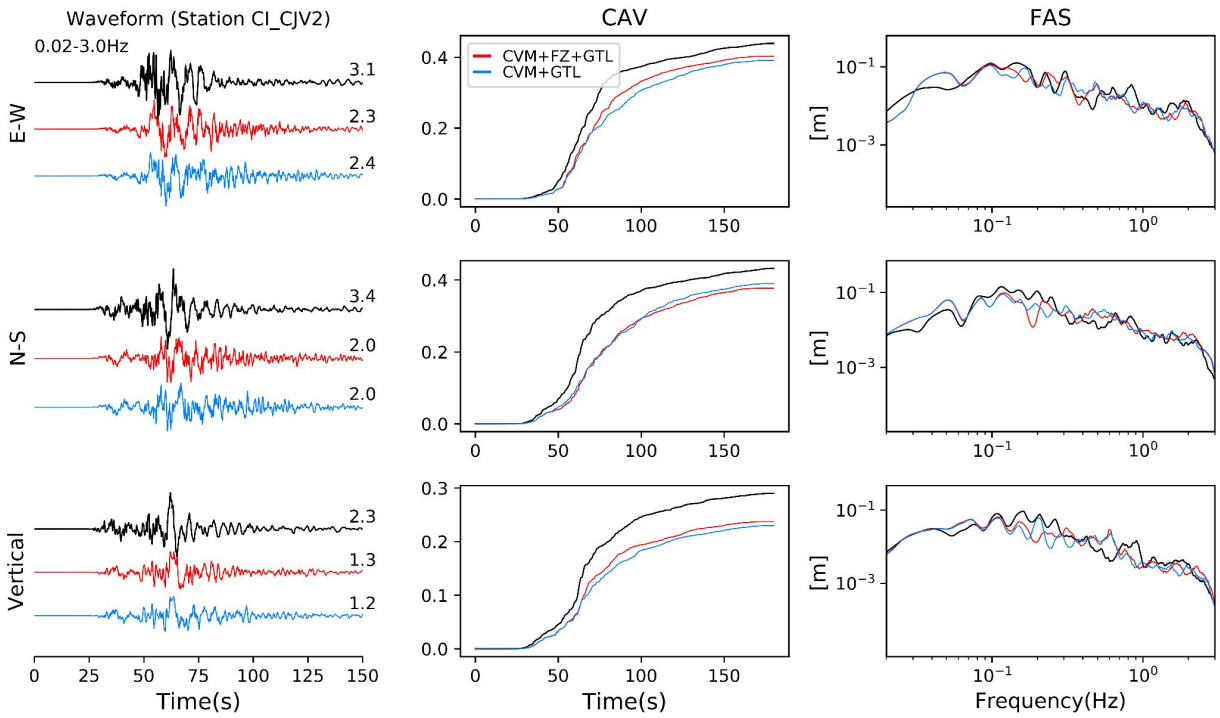

Figure 2.A.10: Comparison of observed and simulated (left) waveforms, (center) CAV, and (right) FAS for station CJV2 for models (red) with and (blue) without adding the fault zone. See Fig. 2.A.2 for location.

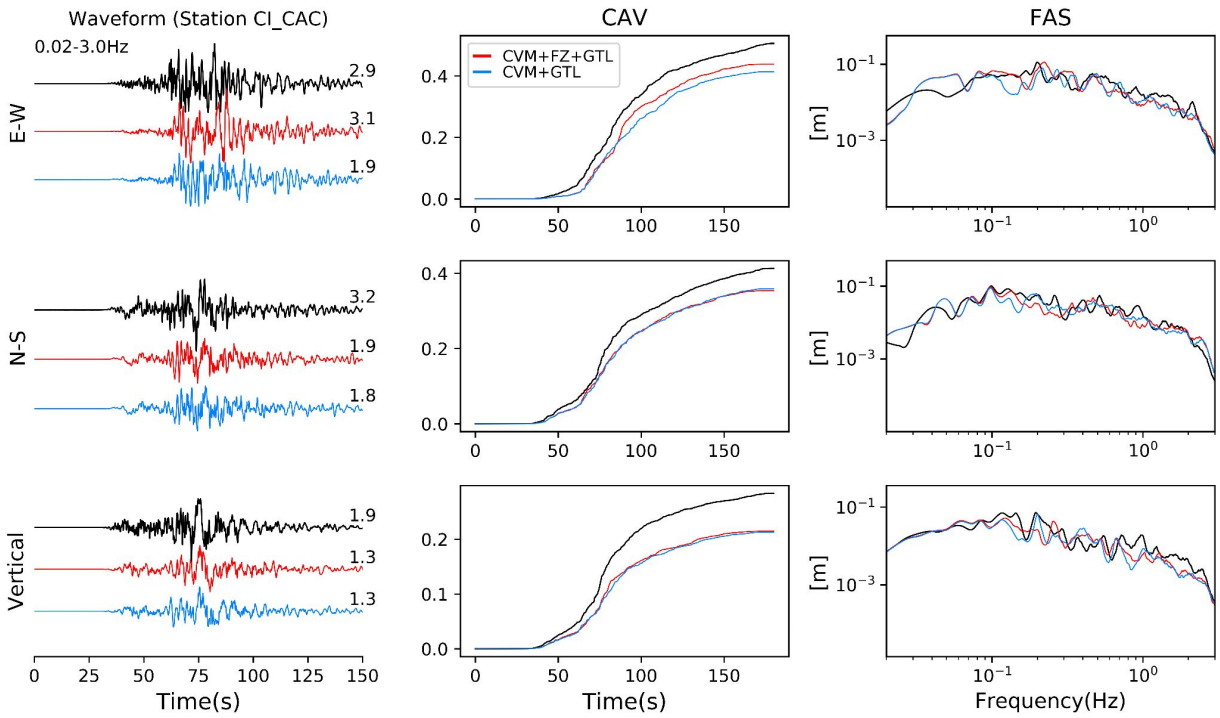

Figure 2.A.11: Same as Fig. 2.A.10, but for station CAC (see Fig. 2.A.2 for location).

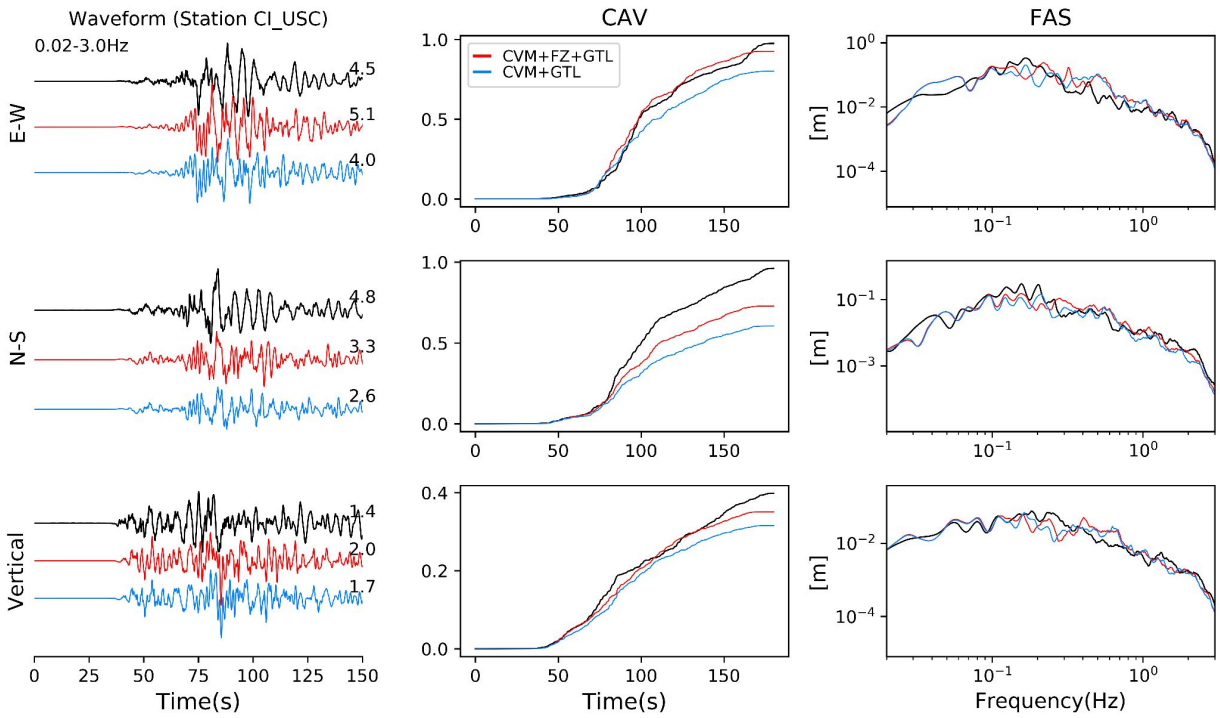

Figure 2.A.12: Same as Fig. 2.A.10, but for station USC (see Fig. 2.A.2 for location).

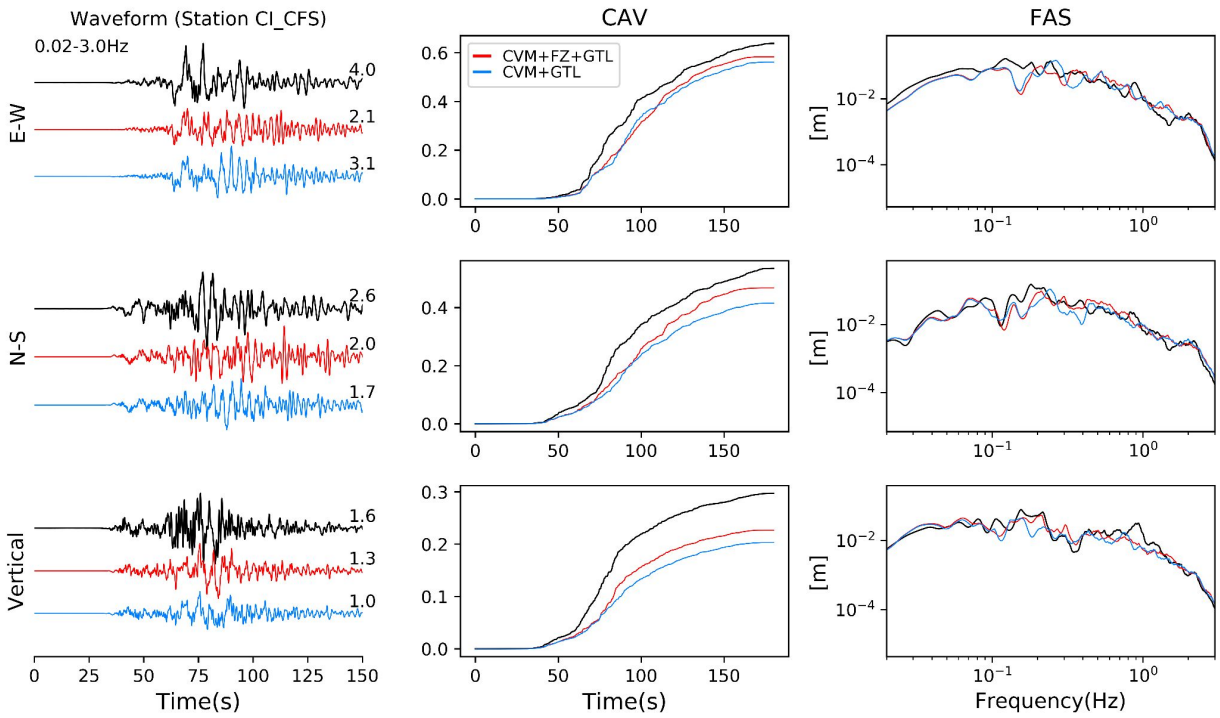

Figure 2.A.13: Same as Fig. 2.A.10, but for station CFS (see Fig. 2.A.2 for location).

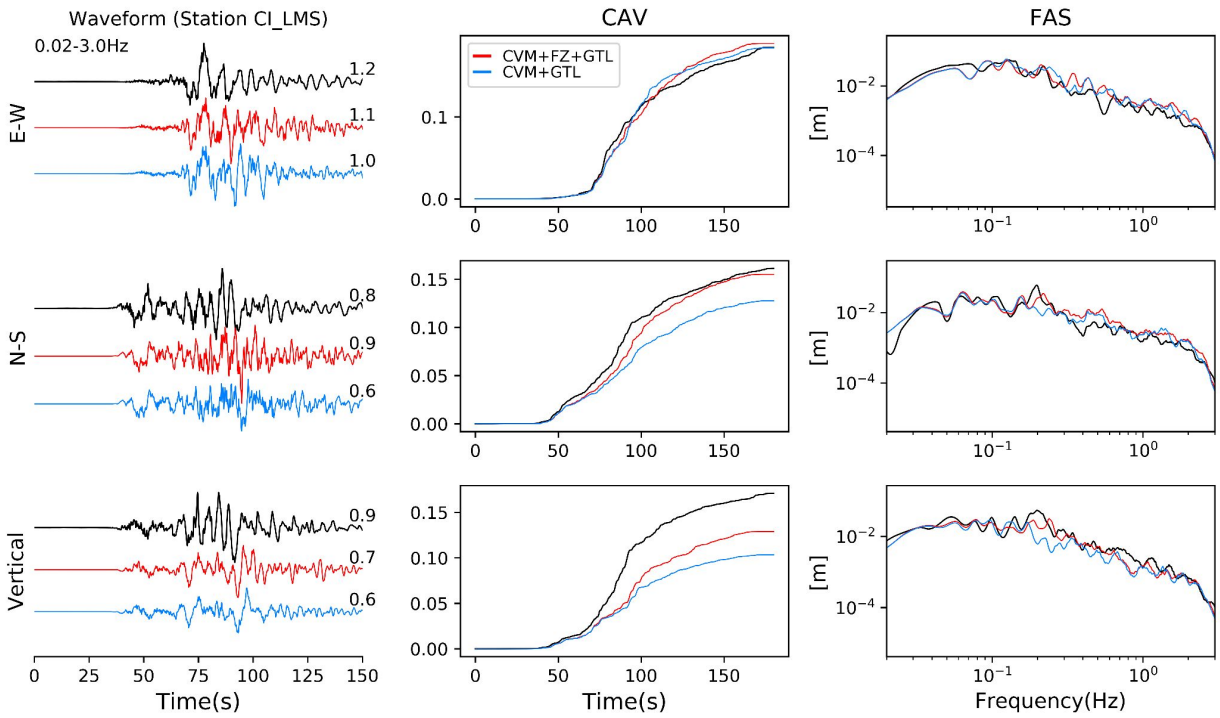

Figure 2.A.14: Same as Fig. 2.A.10, but for station LMS (see Fig. 2.A.2 for location).

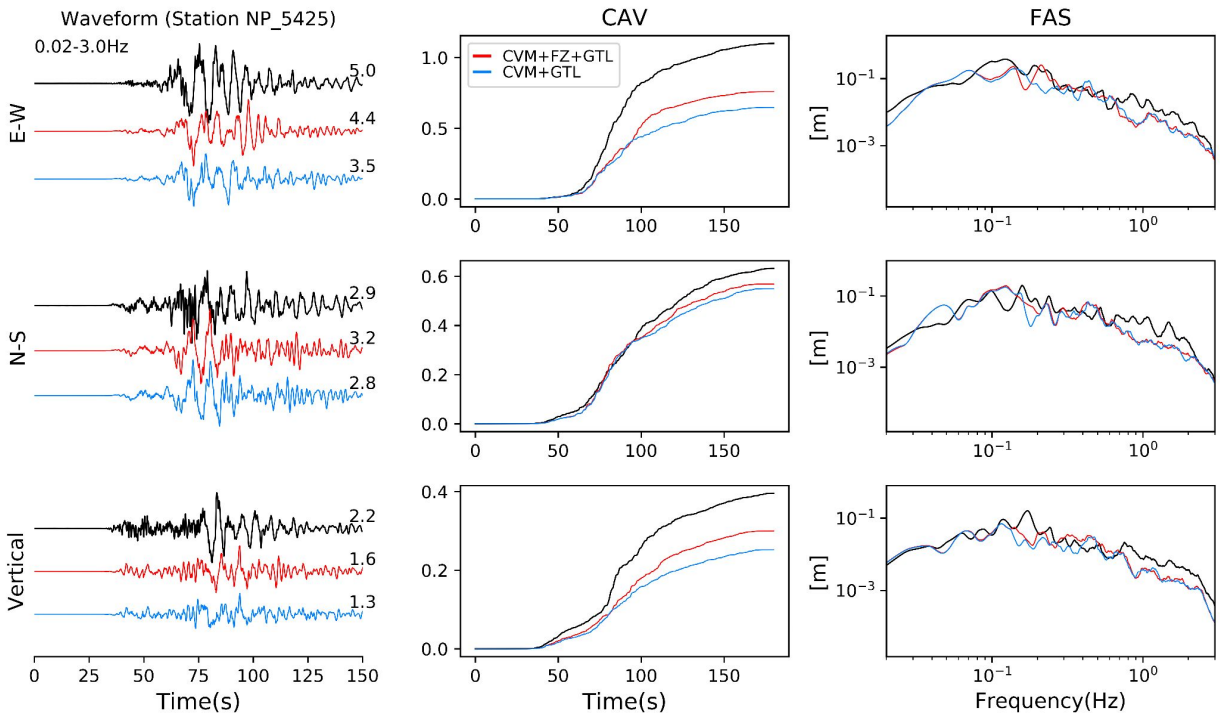

Figure 2.A.15: Same as Fig. 2.A.10, but for station 5425 (see Fig. 2.A.2 for location).

Chapter 3

Simulation and validation of basin amplification effects in Los Angeles during the 2019 M_W 7.1 Ridgecrest, CA earthquake

We have used 0-3 Hz deterministic ground motion simulations of the 2019 M7.1 Ridgecrest, CA, earthquake, to test the accuracy of the Southern California Earthquake Center (SCEC) Unified Community Velocity Model (UCVM) CVM-S4.26.M01 (CVM-S) for prediction of seismic amplification in the Los Angeles basin. The simulated basin amplification was validated against observations using spectral accelerations (SA) at different periods as well as Effective Amplitude Spectra (EAS). The numerical simulations are able to capture the average values as well as the spatial complexity of the observed basin amplification observed at periods of 1 s, 6 s and 8 s. We find the largest misfits between observed and simulation at 1 s and 3 s periods, while the model performs very well for 6 s and 8 s periods. Using simple 1D transfer functions, we show that deepening of the basin structure is capable of reducing the misfit between observed and simulated amplification for spectral accelerations at periods of 3 s and longer.

3.1 Introduction

The amplification and extended duration of seismic waves caused by sedimentary basins (hereafter referred to as "basin effects") have been an important, yet challenging issue to address for seismic hazard assessment. For example, amplification caused by basin structure can severely damage infrastructure, as exemplified by the strong ground motions recorded in Mexico City during the 1985 M8 Michoacan earthquake. Here, amplification factors of 3-7 at periods around 3 second were reported, severely damaging many buildings in the city (Bard *et al*., 1988; Campillo *et al*., 1989; Campillo *et al*., 1988). The main cause of the large amplification in Mexico City was the lake sediments underneath the city. Despite the fact that the earthquake source was far from the basin (approximately 350 km), the relatively thin lake-bed sediments with extraordinarily low S-wave velocities amplified the waves significantly.

In general, basin effects are known to be the result of a complex set of factors including basin-edge amplification, focusing and entrapment of waves, and the earthquake source rupture (Olsen, 2000; Day *et al*., 2008; Kawase, 1996; Lee *et al*., 2009). Basin shape, low-velocity sediment layers, and wave interactions at basin edges all contribute to the basin effects (Brissaud *et al*., 2020). Depending on the 3D structure of and the location inside the basin, the dominant resonant frequency and amplification factor can vary substantially (Fäh *et al*., 1994). For densely populated metropolitan areas like the greater Los Angeles (LA) basin where many important facilities of different scales have been built, understanding the characteristics of the local basin effects is critical for earthquake risk mitigation. Toward this goal, our study here aims to investigate the basin effects in the greater Los Angeles area using a state-of-the art deterministic wave propagation simulation method, well calibrated models, and very high density strong motion observations.

Numerical simulations with well-constrained 3D velocity structure have been a useful approach to gain better understanding of these complicated basin amplification effects. For

example, simulations using 3D velocity structures have demonstrated significant long-period effects from the basin structures (Olsen, 1994; Olsen *et al*., 1995; Olsen *et al*., 1995; Frankel, 1993). Simulations of northwest-propagating ruptures on the southern San Andreas fault suggested that waveguide effects caused by inter-connected basins may cause large ground motions in LA (Olsen *et al*., 2006; Olsen *et al*., 2008; Olsen *et al*., 2009; Graves *et al*., 2008). These simulations resulted in highly variable spatial patterns of ground shaking amplitude and duration throughout the basin, and efforts have been made to understand the cause. For example, a numerical study by Olsen (2000) found that different rupture types and source locations can lead to factor-of-two differences in the predicted amplification of peak ground velocity. This suggests that all earthquake scenarios of concern need to be considered in order to estimate a robust mean basin amplification response for probabilistic seismic hazard analysis.

Correlation between amplification and depth to basement has been identified in both observations and simulations (Olsen, 2000; Day *et al*., 2008; Choi *et al*., 2005). To account for the effects from source variability, Day *et al*. (2008) conducted a parametric analysis with synthetic waveforms computed by a suite of numerical simulations for various rupture scenarios. They then derived a source-averaged amplifications model for the LA basin as a function of period and depth to the $V_S = 1.5km/s$ isosurface, which serves as a simple representation of basin amplification that can be easily deployed in empirical ground motion prediction models. Considering simple models of this kind, recent empirical ground motion prediction equations (GMPEs) are able to capture complicated basin effects to some extent without the need to perform costly numerical simulations (Boore *et al*., 2014; Chiou and Youngs, 2008; Campbell and Bozorgnia, 2008). This is useful in general engineering practices with a lack of direct seismic observations for nearby large earthquakes. Unfortunately, large uncertainties in the hazard assessment result from the smoothing intrinsic to the GMPE parameterizations. In addition, source-averaged basin amplification models do not predict variations corresponding to different source scenarios, which poses limitations on the application of GMPE-based approaches.

Due to recent advances on computing speeds, numerical methods, and access to computational resources, 3D seismic hazard assessment including basin effects using physics-based ground motion simulations have significantly improved. For example, the resolution and accuracy of crustal models for southern California have evolved remarkably over the past two decades. The Southern California Earthquake Center (SCEC) Unified Community Velocity Model (UCVM) provides the reference models CVM-S4.26.M01 and CVM-H v15.1 (CVM-S and CVM-H, respectively from here on) for southern California, including near-surface geotechnical layers (GTLs) from various geophysical surveys in the LA basin (Small *et al*., 2017; Lee *et al*., 2014; Shaw *et al*., 2015). Hu *et al*. (2022b) improved the representation of the near-surface velocity structures outside of the basin where the GTL is not well constrained in the CVM-S. Considering the calibrated GTL, Hu *et al*. (2022a) simulated 0-5 Hz ground motions of the 2014 La Habra earthquake and estimated the range of parameters for $Q(f)$ for the greater LA area important for modeling high-frequency waves ($\geq$ 1 Hz) (Withers *et al*., 2015).

Several dense seismic networks operate in southern California, including the Southern California Seismic Network (SCSN), the California Strong Motion Instrumentation Program (CSMIP), and the Community Seismic Network (CSN) providing an average station spacing of 0.5 km in the LA basin (Clayton *et al*., 2015). Kohler *et al*. (2020) analyzed a a high-density data set recorded by SCSN, CSMIP, and CSN, and measured the amplifications for ground level sites in the LA basin at 4 periods between 1 - 10 s relative to the averaged combined horizontal spectral accelerations of three bedrock reference sites for the 2019 M_w 7.1 Ridgecrest earthquake. This was the first time basin amplification was directly observed on such high spatial resolution in the greater LA area. Due to the high-density nature of the seismic stations, the authors were able to identify a coherent spatial pattern in long-period (longer than 3 s) amplifications somewhat correlated with the depth to basement and with a weak correlation to the local V_{S30}.

Our study aims to test the accuracy of the SCEC CVM-S to predict ground motion amplification in the LA basin by comparing seismic recordings to the result of numerical simulations of

the M_w 7.1 Ridgecrest earthquake. Here, we include the lessons learned in Chapter 2 from a series of long-range ($\geq$250 km) numerical simulations of the 2019 M_w 7.1 Ridgecrest, CA earthquake, constraining $Q(f)$ and GTL parameters covering a broad domain in southern California. In addition, we included the data-constrained fault damage zone structure by Zhou *et al*. (2022) which was shown to significantly improve prediction of ground motions in the LA basin Chapter 2.

After the introduction, we provide a description of the study domain and the numerical model used to simulate the wavefield. It is followed by a section explaining how we define the basin amplification factor and how the measurement is carried out for a data set consisting of 393 stations operated under the SCSN and CSN networks. After the same procedure is repeated for both observed and synthetic waveforms, we discuss the differences between the observed and simulated response at different periods. The final section summarizes our findings and the limitations of our study, and suggests improvements to the CVM-S.

3.2 Modeling approach

3.2.1 Simulation method

We have simulated deterministic 3D wave propagation of the 2019 M_w 7.1 Ridgecrest, CA, earthquake, using the GPU-enabled, highly scalable, fourth-order-accurate staggered-grid finite-difference code AWP-ODC (Cui *et al*., 2013). AWP-ODC benefits from a discontinuous mesh (DM) structure, where the grid spacing varies by a factor of 3 between meshes along the vertical direction (Nie *et al*., 2017). The DM structure with 3 times increase in grid spacing between meshes allows AWP-ODC to increase grid spacing at depth as velocities increase, resulting in considerable savings in memory and computational cost compared to a uniform-grid mesh, for a realistic basin model. AWP-ODC supports frequency-dependent attenuation, following a power-law description:

$$
\begin{aligned}
Q_s(f) &= Q_{s,0}, \quad f < f_0, \\
Q_s(f) &= Q_{s,0}\left(\frac{f}{f_0}\right)^{\gamma}, \quad f \geq f_0,
\end{aligned}
\tag{3.1}
$$

where the transition frequency f_0 is 1 Hz, $Q_{S,0}$ is a constant Q_S value, and γ controls the rate of increase for the Q_S value above 1 Hz (Withers *et al*., 2015). In Chapter 2, $Q(f) = Q_{S,0}/V_S = 0.1$ with $\gamma = 0.5$ was found to be the most suitable attenuation model for the simulation domain which produces unbiased Fourier amplitude spectra and peak ground accelerations in all distance ranges up to 3 Hz. We used $Q_p = 2Q_s$ for the simulation, following Olsen *et al*. (2003).

In the shallowest mesh, calculations are performed on curvilinear grids, which enable accurate description of the topographic elevation (O'Reilly *et al*., 2021). Our simulations used the southern California digital elevation model (DEM) of 3-arc-second resolution (model can be accessed via https://www.ngdc.noaa.gov/). We simulated wave propagation in an area of extent 200 km x 300 km, and 150 km in depth, which includes the greater LA basin (Fig. 3.1). The domain is rotated by 25^o clockwise in order to reduce memory requirements. We furthermore set V_S of material with V_S of 300 m/s or less to 300 m/s ('clamped' in the following), in order to limit computational resources. Following the approach of Hu *et al*. (2022b), we added an approximation of the effects of the material with V_S less than 300 m/s as a post-processing step to the horizontal motions of 3D synthetics, which we found negligible in this case. To achieve a f_{max} of 3 Hz, the shallowest mesh has a horizontal grid spacing of 15 m, where the vertical grid spacing varies with local topographic elevation due to the curvilinear stretching. Two coarser-grid meshes with grid sizes of 45 m and 135 m were introduced at around 12 km and 24 km depths below sea level, respectively. Table 3.1 tabulates the details about the numerical model setup for this study.

3.2.2 Velocity model

In order to assemble the velocity model for the Ridgecrest earthquake simulations, we first queried velocity and density information from the CVM-S (Small *et al*., 2017). Then, we incorporated the fault zone velocity structure in the region around the faults that ruptured during the 2019 Ridgecrest earthquake series, imaged by Zhou *et al*. (2022) (Fig. 3.1). To ensure a smooth transition between the fault zone model and the surrounding CVM-S, we used the method by Ajala and Persaud (2021) with a tapering zone of 15 km width along the side boundaries and 600 m along the bottom. We calculated V_P and density, not available from the noise tomography imaging by Zhou *et al*. (2022), using the empirical relations by Brocher (2005).

To more accurately account for the near-surface structure, we followed Hu *et al*. (2022b) and modified the velocity and density structures in the top 700 m of the model (the geotechnical layer, GTL). This approach uses the local V_{S30} information (Wills *et al*., 2015) along with the formulation proposed by Ely *et al*. (2010) to generate near-surface velocity profiles for a given background velocity model. Incorporating the GTL is the last step of model preparation, after the Zhou *et al*. (2022) fault zone model was merged with the CVM-S. This GTL tapering approach only replaces the material properties when the V_S computed using Ely *et al*. (2010) is smaller than the existing value, such that existing low-V_S material, generally limited to more well-constrained basin sediments, remains in the model.

3.2.3 Kinematic finite-fault rupture model

The source of the 2019 M_w 7.1 Ridgecrest earthquake was described by a finite-fault rupture model derived from kinematic inversion of seismic and geodetic data (Liu *et al*., 2019). While constrained by strong motion data, the frequency content of the source inversion model was limited to frequencies below 0.5 Hz. In order to use the source model up to 3 Hz in the simulations, we enhanced the spectral energy of the slip-rate functions on each subfault by superimposing von

Karman correlated noise, such that the resulting total moment-rate function follows a f^{-2} fall-off rate. This technique was applied in Chapter 2, and details are provided in Section 2.3.

3.2.4 Calculation of site amplification

We examined a data set of 393 stations, consisting of 49 CI (Southern California Seismic Network) and 6 NP (United States National Strong-Motion Network) stations accessed via the Southern California Seismic Network (SCSN) and 338 stations from the Community Seismic Network (CSN), located in the study area shown by the red box in Fig. 3.1. Note that only ground level stations were used. The high density of the CSN stations significantly enhances the resolution of the basin effects. It is worth noting that Kohler *et al*. (2020) verified the consistency of the data sets recorded by the different networks.

We computed the site amplification factors from both observed and synthetic acceleration data for each site using the same data processing procedure, described as follows. The observed waveforms were first lowpass-filtered with a corner frequency of 3 Hz to be consistent with the filter applied to the moment-rate functions of all the subfaults prior to the numerical simulation. Before calculating the SA, a Butterworth bandpass filter with corner frequencies of 0.07 and 3 Hz was applied to both observations and synthetics. After these steps, 2%-damping spectral accelerations (SAs) were computed at 1, 3, 6, and 8 s periods. The SA here refers to the combined response of the two horizontal components rotated to find the maximum value. The orientation associated with the maximum horizontal SA at each site was also reported, to show the dominant direction of the response.

At a given period, the amplification factor at a given site was derived by computing the ratio of SA with respect to the averaged value of all the reference sites, as

$$A_i(T) = \frac{Sa_i(T)}{Sa_{ref}(T)}, \tag{3.2}$$

where T is the period, $A_i(T)$ and $Sa_i(T)$ are the amplification factor and SA at station i, respectively, and $Sa_{ref}(T)$ is the averaged SA of all the reference sites. This measurement was done for both observed and simulated acceleration waveforms at all included sites.

We use 8 SCSN stations as reference sites which are located slightly outside the LA basin, namely CI_SPF, NP_5081, CI_HLL, CI_KIK, CI_GOU, CI_PDU, CI_CHN, and CI_PASC (locations shown by magenta circles in Fig. 3.1b). The use of multiple reference sites minimizes source and local site effects in the spectral ratio and reduces the sensitivity of the results to the choice of reference.

Despite our slightly different definition for site amplification and a larger set of reference sites, the spatial patterns and the orientations associated with the amplifications that we measured from observations are in excellent agreement with Kohler *et al*. (2020)'s calculation for all the analyzed periods. On the other hand, our different choice of reference sites generates slightly lower amplification values than those by Kohler *et al*. (2020).

We follow Kohler *et al*. (2020) and Cruz and Miranda (2017) in using amplification factors computed for SAs based on 2% damping, which they argued are more representative for mid-size and high-rise buildings, as compared to the more commonly used 5% damping. For completeness, we also calculated the 5%-damped spectral accelerations (see Figs. 3.A.1 and 3.A.2) which are reasonably similar to the results for 2% damping.

While we have focused on SAs in our analysis above, site amplification can be estimated based on other metrics. For additional insight, as the Fourier amplitude spectrum (FAS) - based ground motion models recently have become more widely used, we also calculated basin amplifications estimated based on the effective amplitude spectrum (EAS) (Goulet *et al*., 2018). The details of the calculation of the EAS-based amplification can be found in Section 3.A.1. EAS is independent of the orientation of the two orthogonal horizontal components of ground motion records and can be derived directly from the FAS without the need for choosing a damping value (Boore, 2003; Goulet *et al*., 2018; Kottke *et al*., 2021). In addition, EAS and FAS do not

include the intrinsic spectral smoothing of SAs, resulting in a more straightforward evaluation of the differences between data and simulations. The EAS-based amplification results for all the analyzed periods are provided in Figs. 3.A.3 and 3.A.4.

3.3 Los Angeles basin amplification

In this section, we present the amplification patterns extracted from our simulations and observations, and quantitatively validate the simulations against data recorded at all stations shown in Fig. 3.1 (red box).

3.3.1 Amplification patterns

Fig. 3.2 shows the amplification factors for SA-1s, SA-3s, SA-6s and SA-8s. The short-period basin effects are expected to be more sensitive to the small-scale features such as the local site characteristics (V_{S30}) or topography, which generate a complex pattern with relatively short spatial correlation distance. This is the case for both observed (Fig. 3.2, left) and simulated (Fig. 3.2, right) amplifications, which exhibit large fluctuations over the studied domain at 1 s period (a-b in Fig. 3.2). Similar complexity can be observed in the orientations of maximum SA for both observations and the simulation. At 3 s period, some spatial coherency is noticeable in the northern part of the LA basin, with an E-W aligned band of higher amplification along the northeastern wall of the basin, as well as near the deepest part of the basin (c-d in Fig. 3.2). However, the simulation overpredicts SA-3s along the eastern wall of the basin, in particular near the deepest part of the basin (white box in Fig. 3.2d). This bias may indicate that the basin structure in CVM-S is too shallow, as discussed in section **Discussion and conclusions**.

For the longer-period amplifications (6-8 s), a clear spatial pattern coherent with the basin structure is evident, much smoother than that for the short-period results. Both amplification

maps from data and simulation for 6 and 8 s periods reveal a large amplification hot spot along the southwestern wall of the LA basin, which is near the southwest corner of the dense CSN network (Fig. 3.2 c-d and e-f). The predicted amplification at 6 s period near the central basin is slightly higher than observations (near the southern edge of the CSN network in Fig. 3.2f, where the larger overprediction at 3 s was found, see Fig. 3.2d). In agreement with Kohler *et al*. (2020), we notice that the location of the amplification hot spot is close to but does not exactly match the deepest part of the basin for both data and simulation.

Similar to the amplification, the spatial pattern of the orientations of the maximum horizontal SAs becomes more spatially coherent as the period increases from 3 s to 8 s. The dominant NW-SE trend of the orientations for SA-8s matches the polarization direction of SH waves considering the azimuth of the source relative to the basin, likely caused by long-period surface wave amplification along the basin structure.

3.3.2 Quantitative validation

To quantify the errors of the model predictions, we use the mean absolute percent error, given by

$$Error = \frac{1}{N_{sta}} \left(\sum_{i=1}^{N_{sta}} \left| \frac{A_{o,i} - A_{s,i}}{A_{o,i}} \right| \right) \times 100\%, \tag{3.3}$$

where $A_{o,i}$ and $A_{s,i}$ are amplification factors measured from observed and synthetic waveforms at the i-th station, respectively. Table 3.2 summarizes the misfits between predicted and observed site amplification factors for different periods computed using Eq. (3.3). While fitting the observations well at longer periods (6-8 s), the simulation overpredicts the amplifications at 3 s period along the northeastern edge of the basin all the way into the central basin (Fig. 3.2d). As can be seen in Fig. 3.3b, the simulation has a clear trend of overprediction by a factor of 1.5-2 at 3 s period, decreasing to 1.2 at 6 s period. See Section 3.4 for a discussion on possible causes of this

overprediction.

The amplification values exhibit a decreasing trend with V_{S30} in both observations and simulation as shown in Fig. 3.4, but with large scatter for all the selected periods. This trend is larger for the simulation as compared to the data for SA-1s and SA-3s, but similar for SA-6s and SA-8s. The large scatter complicates extraction of clues to the misfit between the SA amplification for simulation and data, in particular for SA-1s. For SA-3s, the sites with V_{S30} less than about 500 m/s appear to be amplified by more than a factor of 1.5. However, as trends in V_{S30} are not expected to affect the longer periods, V_{S30} is likely a proxy for other parameters, such as basin depth.

We find a positive correlation between site amplification in terms of SA and the depth to the V_S=2.5km/s isosurface (as a proxy to the depth to the basement) at periods of 3 s and longer, whereas neither data nor simulation support significant correlation to the basin depth at 1 s period (Fig. 3.5). However, the increase in amplification versus depth of the basin appears to saturate at about 2000-3000 m depth for SA-3s, SA-6s, and SA-8s. This saturation was also found for the source-averaged parametric model for basin amplification derived by Day *et al*. (2008) and Olsen (2000) for peak ground velocity. We note that using a different isosurface (e.g., V_S =1.5 km/s) for this analysis yields a similar trend since depths to different isosurfaces in the CVM-S are highly correlated (see Fig. 3.A.5).

3.4 Discussion and conclusions

The strong motion data recorded by high-density seismic networks for the 2019 M_w 7.1 Ridgecrest event presents an unique opportunity to test how well numerical simulations can replicate the observed basin amplifications. Toward this goal, we have performed state-of-the-art 0-3 Hz 3D numerical wave propagation simulations using a 3D velocity model extracted from the SCEC CVM-S with a high-resolution fault zone model around the Ridgecrest area, surface

topography, a GTL, and a well-calibrated $Q(f)$ model.

We find that the accuracy of the SCEC CVM-S in terms of long-period SA amplification varies with period. Our analysis with three types of site amlification factors shows that the model error is the largest at 3 s period (46% error for 2%-damped spectral acceleration), whereas the model performs very well for 6 s and 8 s periods with misfits less than $\sim$ 20%. The average misfit for 1 s period SA amplification is between those for 3 s and 6-8 s, with highly complex spatial variation. We also calculated the LA basin amplification for SAs with 5% damping, a widely-used metric among structural engineers, as well as EAS (details in Section 3.A.1). Both metrics generate amplification misfits that are similar to or smaller than (specifically at a period of 3 s) those for SA with 2% damping, as summarized in Table 3.2 (see Figs. 3.A.1 and 3.A.2 for 5%-damped spectral acceleration, and Figs. 3.A.3 and 3.A.4 for EAS).

The amplification factors estimated in this study for the 2019 M_w 7.1 Ridgecrest event are in reasonable agreement with previous numerical studies for the LA basin (Olsen, 2000; Day *et al.*, 2008). For example, the amplification factors we calculated based on 5%-damped spectral acceleration are near the lower range of the estimates from Day *et al.* (2008)'s source-averaged parametric model for periods longer than 3 s (see Figure 9 in Day *et al.* (2008)). Reasons for the different SA amplification values include that our estimate only represents a single source as opposed to a suite of 60 scenarios by Day *et al.* (2008). In addition, an older version of CVM-S (Magistrale *et al.*, 2000) was used in Day *et al.* (2008), with significant differences in basin depths. However, the most likely reason for the smaller amplification values with depth obtained in our study is the different approaches used to estimate the amplification factors. The reference values used by Day *et al.* (2008) for calculating their amplification were obtained from simulations in a 1D model with unrealistically large surface velocities, due to the lack of a GTL. The omission of a GTL may have biased the reference values low and the amplifications high.

Simulating the same event, a recent study by Muir *et al.* (2022) pointed out that 3D numerical simulations through the SCEC CVM-S and CVM-H were not able to accurately predict

the observed basin amplifications in the 0.1-1 Hz range. However, by combining the CVM-S with the most recent results on anelastic attenuation and GTL parameters (Hu *et al*., 2022b; Hu *et al*., 2022a; Withers *et al*., 2015), we have shown that our numerical simulations generate satisfactory fit to the observed amplification, with the vast majority of the predicted amplification values within a factor of two of those for the observations (Fig. 3.3). The larger scatter in the simulated amplification for SA-1 s is likely caused by inaccuracies in the the small-scale structures (on the scale of tens to hundreds of meters), despite the use of an abundance of constraints in the GTL of the CVM-S (Small *et al*., 2017).

The largest misfits between the simulated and observed SA amplification in Los Angeles for the M_w 7.1 Ridgecrest event occur at a period of 3 s. Similar overprediction of amplification has been reported by Muir *et al*. (2022) in their predicted amplifications for SA-4 s (the shortest period analyzed in their study), also using CVM-S. A period of 3 s and an average shear wave speed of 1,400 m/s in the basin corresponds to a wavelength of 4.2 km, which is on the scale of the deeper structure of the LA basin itself. Therefore, the overprediction of the SA amplification at 3 s period may be alleviated by improving the velocity structure on a length scale of of 1-5 km. The recent imaging of the LA basin structure carried out by Muir *et al*. (2022), suggesting slower basin material with further deepening (up 2 km) of the deepest part of the basin, agrees with this assessment. In fact, the region where our simulation overpredicts the SA-3s amplification coincides surprisingly well with the locations where their inversion result suggest deeper basin depths (see Figure 11b in their study).

In order to test the hypothesis that deeper LA basin depths in the CVM-S can improve the prediction of amplifications, we further analyzed the velocity structure in the area inside the white rectangle in Fig. 3.2d. We extracted V_S profiles beneath the stations inside the white box in Fig. 3.2d, and perturbed these profiles by multiplying a linear scaling function,

$$V_S^{new}(z) = V_S^{current}(z)(1+zk), \tag{3.4}$$

where z is depth in meters and k is a constant. We examined a slower (deeper) and a faster (shallower) basin model by setting $k = -0.00002$ and $k = 0.00002$, respectively. Vertically-incident SH-wave transfer functions were computed for both current and perturbed V_S profiles, which we used to form the correction functions that approximate the responses of a slower and a faster basin model. To demonstrate the overall effects of the two different perturbations, Fig. 3.6 compares the harmonic average of all the V_S profiles and the corresponding transfer function, along with those for the slower and faster versions of the average model for comparison. The transfer functions in Fig. 3.6b clearly show that a deepening of the basin can lower the spectral energy, and therefore potentially reduce the prediction errors at 3 s period, while the model the with shallower basin has the opposite effect. The correction functions for the individual sites were then applied to the two horizontal components of the synthetic waveforms in the frequency domain to approximate the response of the slower and faster models. The site amplifications calculated after the correction are shown in Fig. 3.7. The slower model reduces the overpredicted amplification for SA-3s by the current model and improves the fit to the data at both short and long periods. In contrast, the faster model consistently increases the amplifications at all periods, deviating from the data even further. This simple analysis suggests that a slower (deeper) LA basin structure can improve prediction of the LA basin amplification, in agreement with Muir *et al*. (2022).

It is encouraging that numerical simulations are able to replicate the overall Los Angeles basin amplification generated by the 2019 Ridgecrest M_w 7.1 event. The basin response, however, has been found to vary with source scenarios (Olsen, 2000; Day *et al*., 2008; Choi *et al*., 2005). For that reason, we recommend that the results based on the single simulation presented in this study be extended to more events of various magnitudes and source azimuth with respect to the LA basin. While improving the crustal structure is beyond the scope of this project, our 1D analysis shows that refinement of the basin structure can improve the prediction of amplification. We recommend additional 3D simulations to further investigate how an improved crustal model

can better simulate the LA basin response, for example, using the basin structure imaged by Muir *et al*. (2022).

Finally, while amplification from simulation and data generally show similar trends with basin depth and V_{s30}, the scatter along these trends is large. As also pointed out by Kohler *et al*. (2020), this scatter complicates the use of the regressions for defining correction factors in ground motion prediction equations (GMPEs). The large scatter associated with these relations suggests an over-simplified parameterization of the correction factors. Thus, such correction terms must be applied with caution.

In summary, we have evaluated the accuracy of the SCEC CVM-S in terms of prediction of basin response in the greater LA area for the 2019 M_w 7.1 Ridgecrest, CA, earthquake. Our analysis of basin amplification based on different metrics reveals that numerical simulations using CVM-S including topography and a calibrated GTL and Q model are capable of accurately predicting basin response for the Los Angeles for long periods (6-8 s) which is relevant to mid-to-high rise buildings. The prediction of the amplification at shorter periods (1-3 s) is also reasonable, but may be improved by a more accurate description of small-scale structures near the surface as well as the velocity model of the basin structure.

Acknowledgements

This research was supported through the Southern California Earthquake Center (SCEC; Contribution Numbers 20157 and 21111). SCEC is funded by the National Science Foundation (NSF) Cooperative Agreement EAR-1600087 and the U.S. Geological Survey (USGS) Cooperative Agreement G17AC00047.

Chapter 3, in full, is a reformatted version of a paper currently in preparation for submission for publication: Yeh, T.-Y. and Olsen, K.B. (2022), Simulation and validation of basin effects in Los Angeles during the 2019 M_w 7.1 Ridgecrest, CA earthquake. The dissertation author was

the primary investigator and author of this paper.

Tables and Figures

Table 3.1: Simulation domain

Domain		
Length		200.87 km
Width		304.55 km
Depth		149.61 km
Southwest corner		$-119.50000^o, 34.00000^o$
Northwest corner		$-118.14120^o, 36.50876^o$
Southeast corner		$-117.52448^o, 33.25866^o$
Northeast corner		$-116.11682^o, 35.74564^o$
Spatial resolution		
Grid spacing	15 m	Free surface to 11.97 km below sea level
	45 m	11.87 to 24.78 km below sea level
	135 m	24.47 to 149.61 km below sea level
Maximum frequency		3 Hz
Minimum V_S		300 m/s
Points per minimum wavelength		6.7
Temporal resolution		
Time step		0.0008 s
Simulation time		180 s
MISC		
Attenuation model		$Q_S(f) = 0.1V_S$, for $f \leq 1Hz$ $Q_S(f) = 0.1V_S f^{0.5}$, for $f > 1Hz$ $Q_P = 2Q_S$
Geotechnical tapering depth		700 m

Table 3.2: Error of model prediction

Amplification type	**Period**			
	1 s	3 s	6 s	8 s
Spectral acceleration 2%-damped	37.2%	46.4%	20.3%	16.5%
Spectral acceleration 5%-damped	39.4%	34.8%	21.9%	16.8%
EAS-acceleration	33.9%	32.9%	20.3%	14.7%

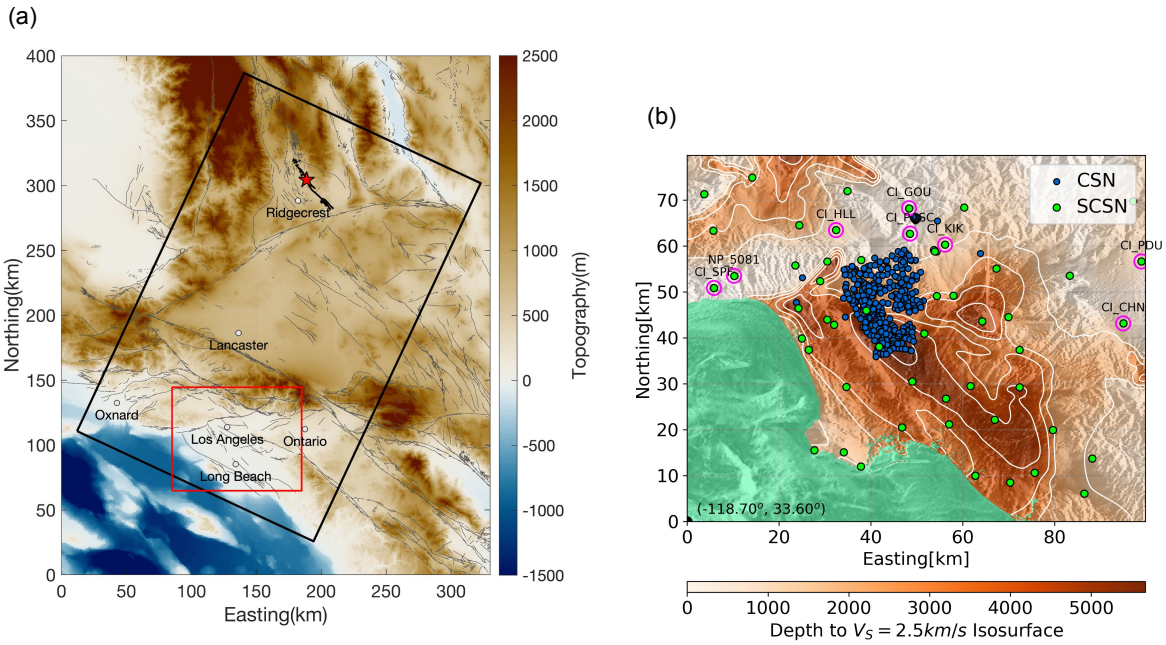

Figure 3.1: (a) Simulation domain (black rectangle) for the 2019 M_w 7.1 Ridgecrest, CA, earthquake. The red asterisk is the epicenter location of the earthquake. Thin gray lines depict Quaternary faults, where the faults that ruptured during the 2019 M_w 7.1 Ridgecrest event are highlighted with a thicker black trace. (b) Blow-up of the region inside the red rectangle on the left where basin amplification is analyzed, showing the station locations of the SCSN (green) and the CSN (blue) network, respectively. Stations marked by magenta circles are the chosen reference sites. White contour lines show depths to the 2,500 m/s isosurface with a 1,000 m spacing.

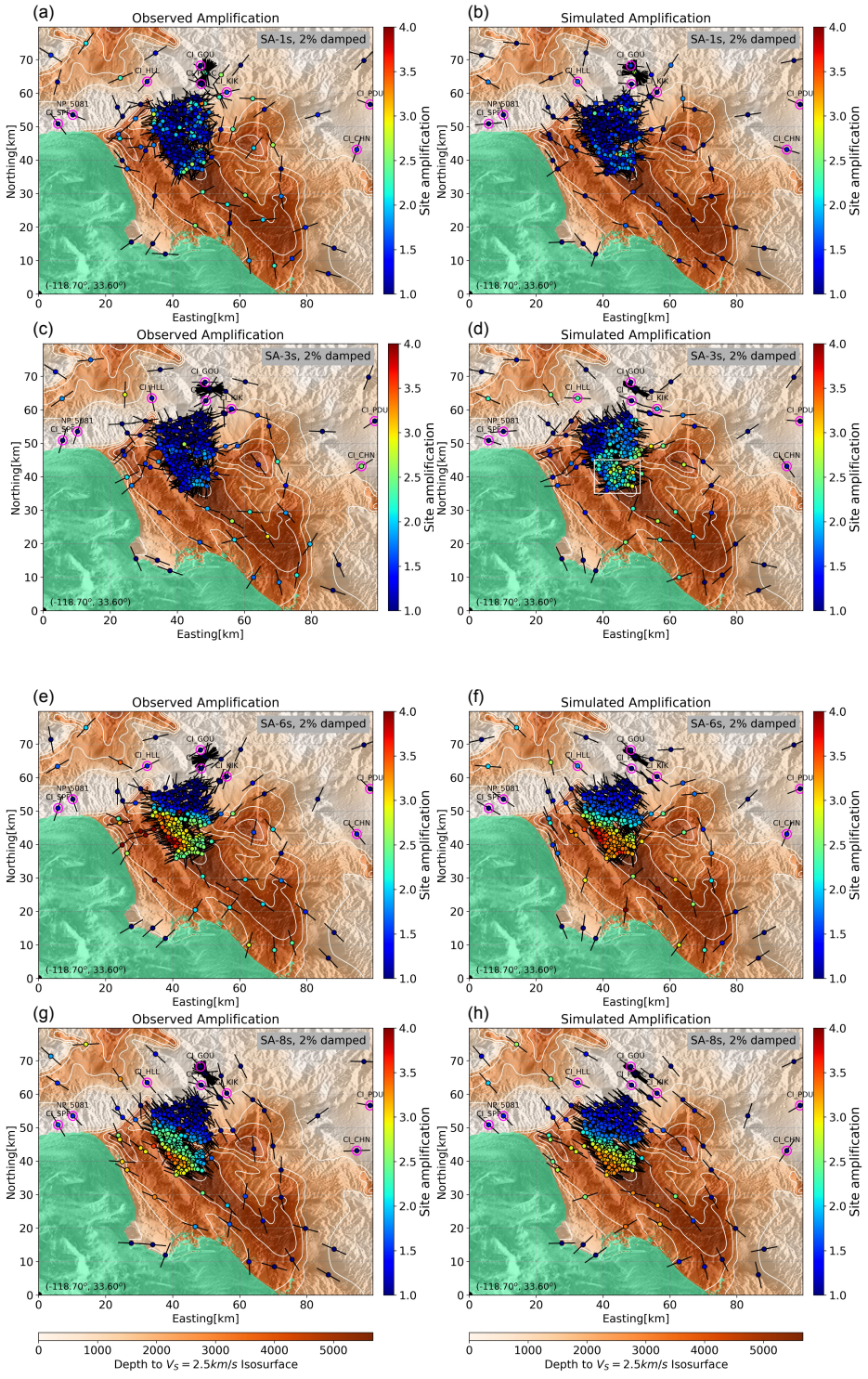

Figure 3.2: Maps showing observed (left column) and simulated (right column) site amplification for 2%-damped SA at 1 s (a-b), 3 s (c-d), 6 s (e-f), and 8 s (g-h) periods. Straight lines depict the orientations associated with the maximum SAs. The white lines show depth contours of the Vs isosurface of 2,500 m/s, with a spacing of 1,000 m.

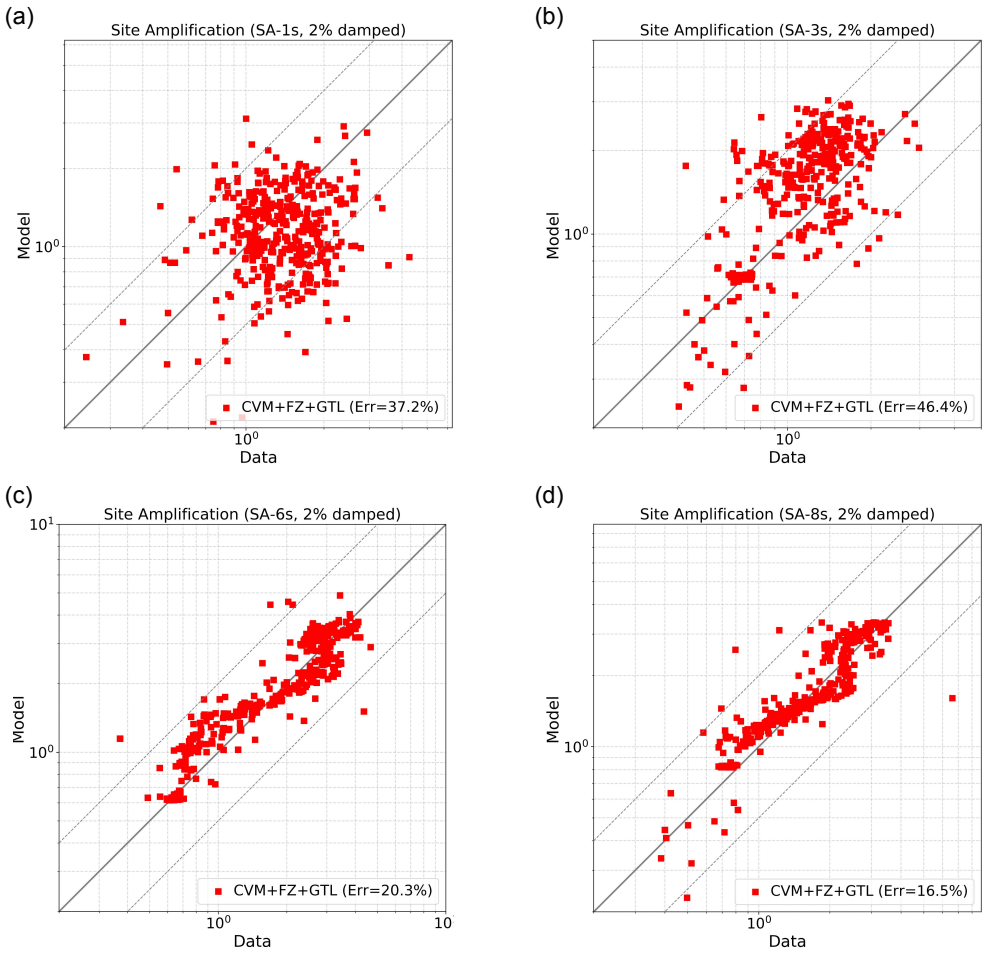

Figure 3.3: Observed versus simulated amplification for 2% damped SAs at 1, 3, 6, and 8 s periods. The dashed lines depict factor-of-two prediction error.

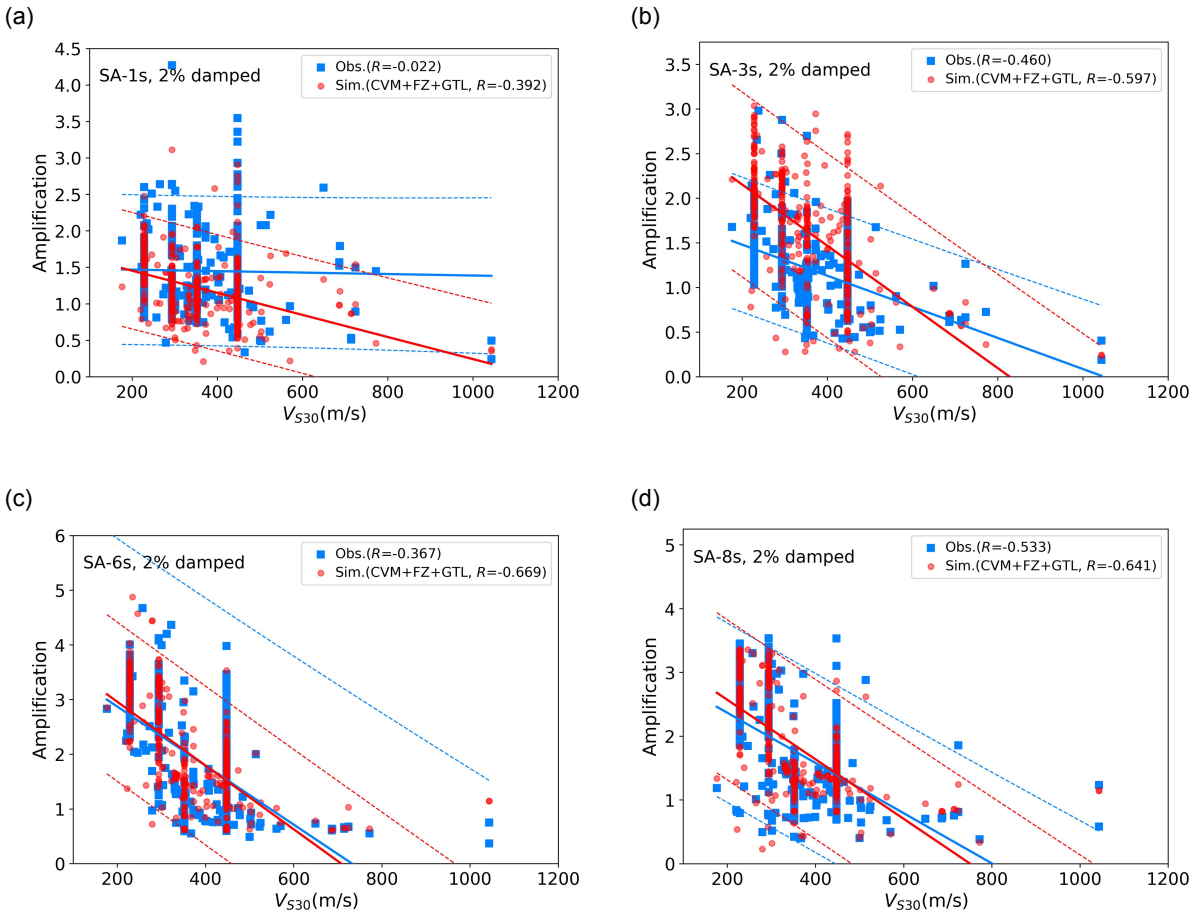

Figure 3.4: Observed and simulated site amplification based on 2% damped SA as a function of local V_{S30} from Wills *et al*. (2015) for different periods. Solid lines are linear regression lines for the observed (blue) and the simulated (red) amplifications where the associated correlation coefficients are provided in the legend, and the dashed lines depict the corresponding 95% confidence intervals.

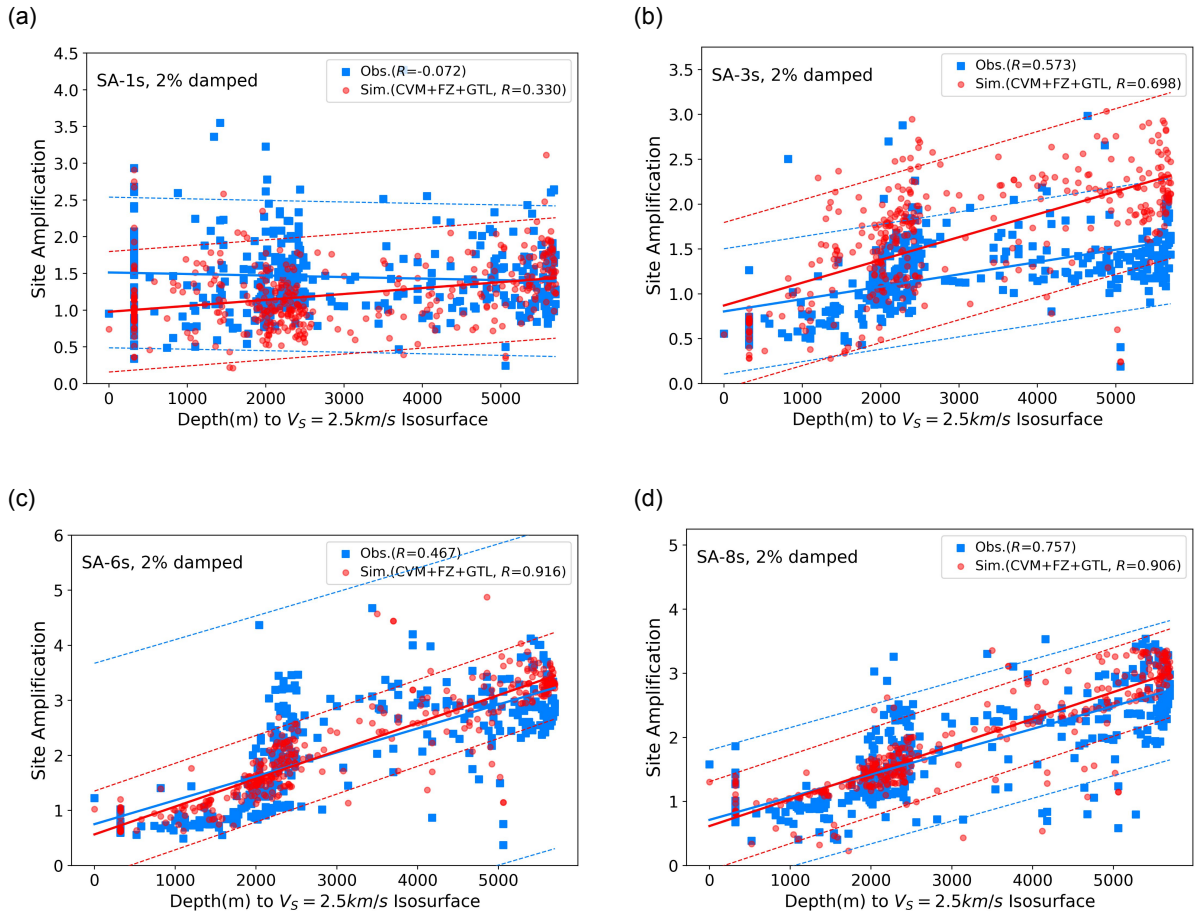

Figure 3.5: Observed and simulated site amplification based on 2% damped SA as a function of depth to the $V_S = 2.5$ km/s isosurface for different periods. Solid lines are linear regression lines for the observed (blue) and the simulated (red) amplifications where the associated correlation coefficients are provided in the legend, and the dashed lines depict the corresponding 95% confidence intervals.

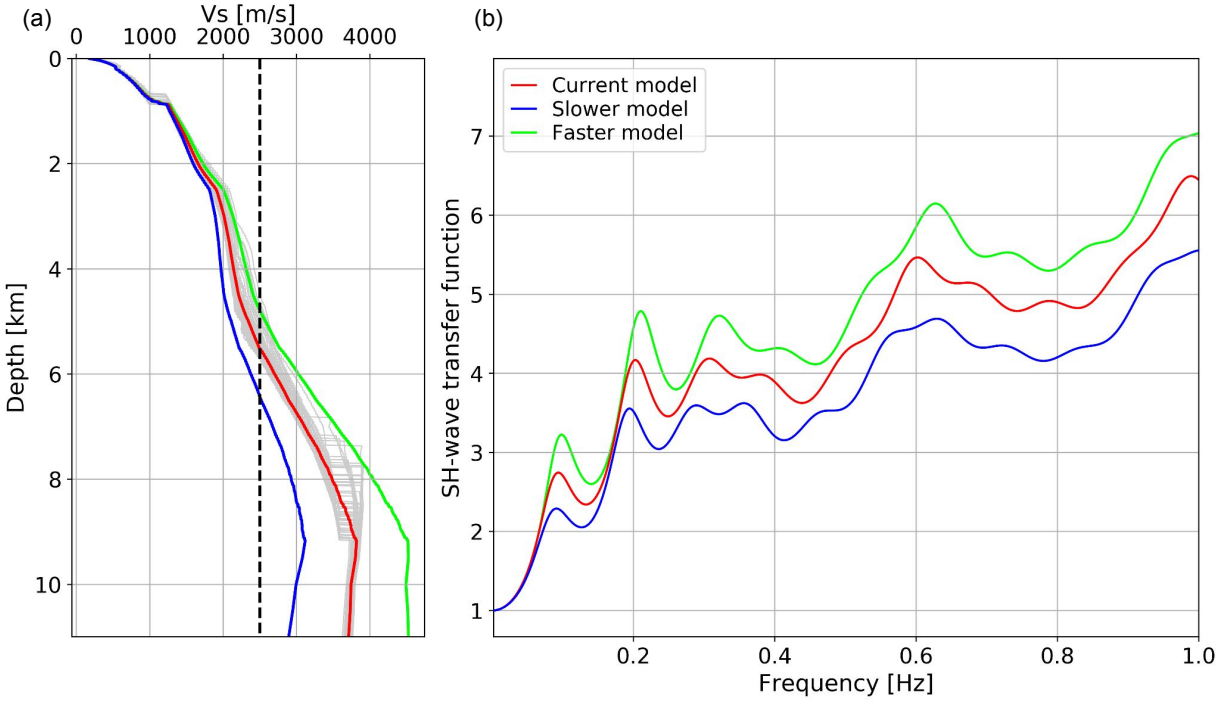

Figure 3.6: Comparison of the V_S profile for the central LA basin extracted from CVM-S along with (a) slower and the faster perturbations, and (b) the corresponding SH-wave transfer functions. The red V_S profile in (a) is the harmonic average of all the V_S profiles extracted from the current model for the stations (shown in grey in the background) located within the white dashed box in Fig. 3.2d. See Section 3.4 for details on how the slower and faster models were derived.

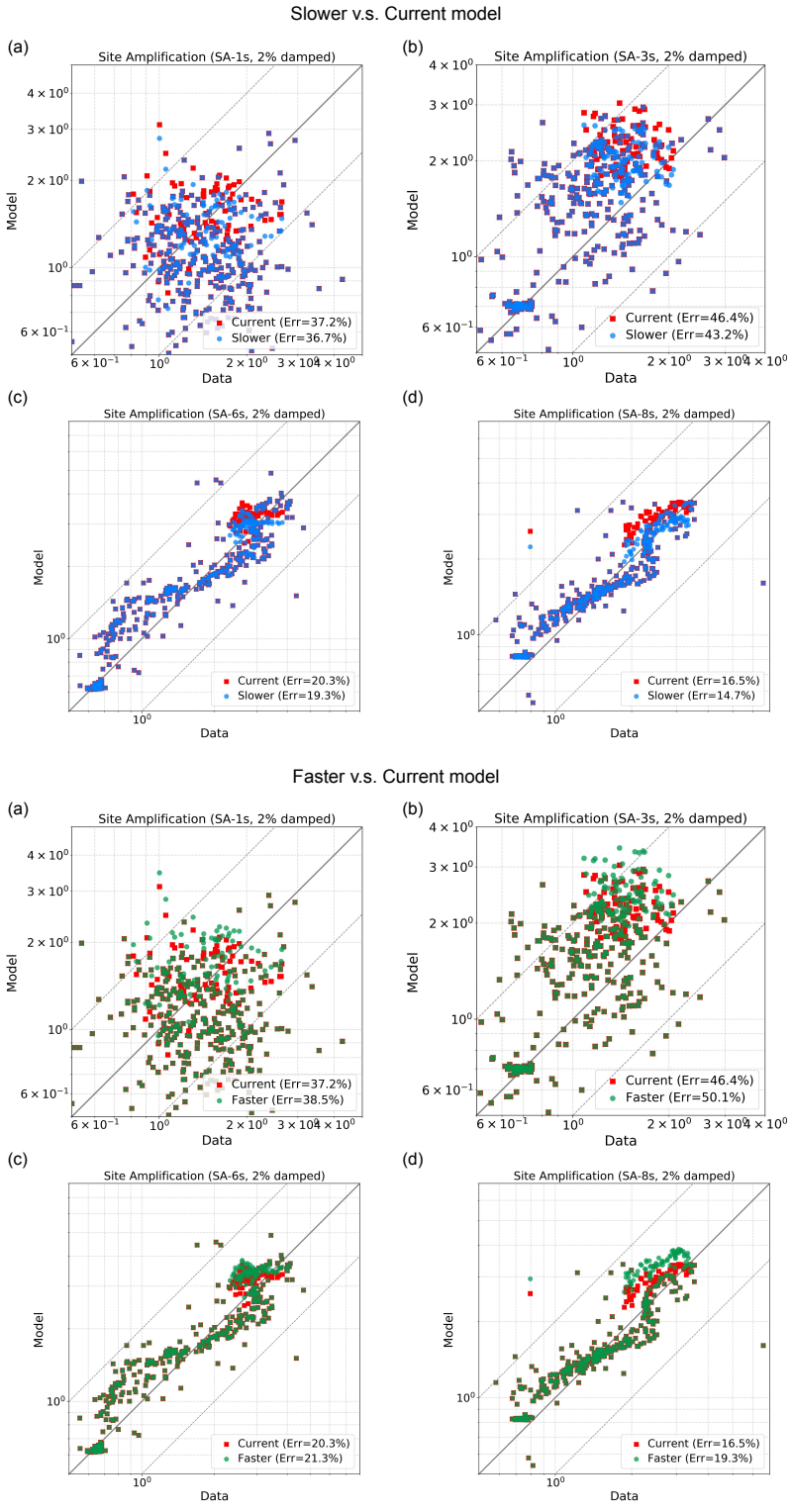

Figure 3.7: Comparisons of site amplification for 2%-damped SA at 1, 3, 6, and 8 s periods predicted for the slower model (a-d) and the faster model (e-h) with respect to the current model.

Appendix

3.A Appendix to Chapter 3

3.A.1 EAS-based amplification

In the section "Los Angeles basin amplification" (Section 3.3), we described the method used to compute site amplification based on spectral accelerations from the two horizontal components. Here, we provide details on the calculation of another type of amplification based on the effective amplitude spectrum (EAS). The EAS-based amplification is defined as

$$EAS(f) = \sqrt{\frac{1}{2}(A_{H1}(f) + A_{H2}(f))} \tag{3.A.1}$$

where $A_{H1}(f)$ and $A_{H2}(f)$ are Fourier Amplitude Spectrum (FAS) of the two horizontal components. Here, the EAS was obtained by computing the root-mean-squared (RMS) value within one-third octave bands (base 10) to reduce the effects of fluctuations around the target frequency. The octave bands corresponding to 1, 3, 6, and 8 s periods are 0.891 - 1.122 Hz, 0.297 - 0.374 Hz, 0.149 - 0.187 Hz, and 0.111 - 0.140 Hz, respectively. The orientation of the largest horizontal ground acceleration for an analyzed frequency is measured in the time domain after band-pass filtering the two horizontal components using the octave band listed above.

3.A.2 Supplementary figures for Chapter 3

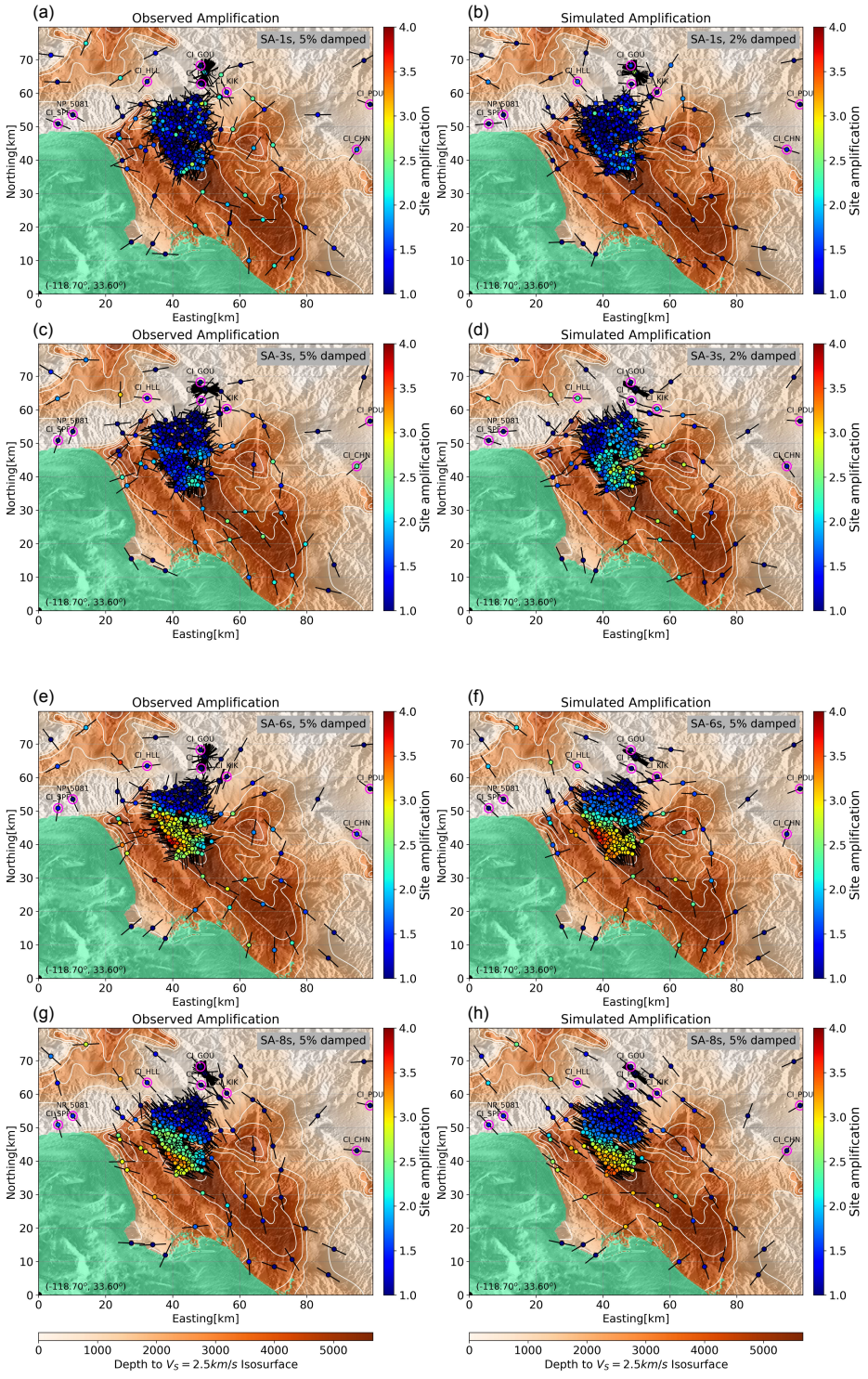

Figure 3.A.1: Maps showing observed (left column) and simulated (right column) site amplification for 5%-damped SA at 1 s (a-b), 3 s (c-d), 6 s (e-f), and 8 s (g-h) periods. Straight lines depict the orientations associated with the maximum SAs. The white lines show depth contours of the Vs isosurface of 2,500 m/s, with a spacing of 1,000 m.

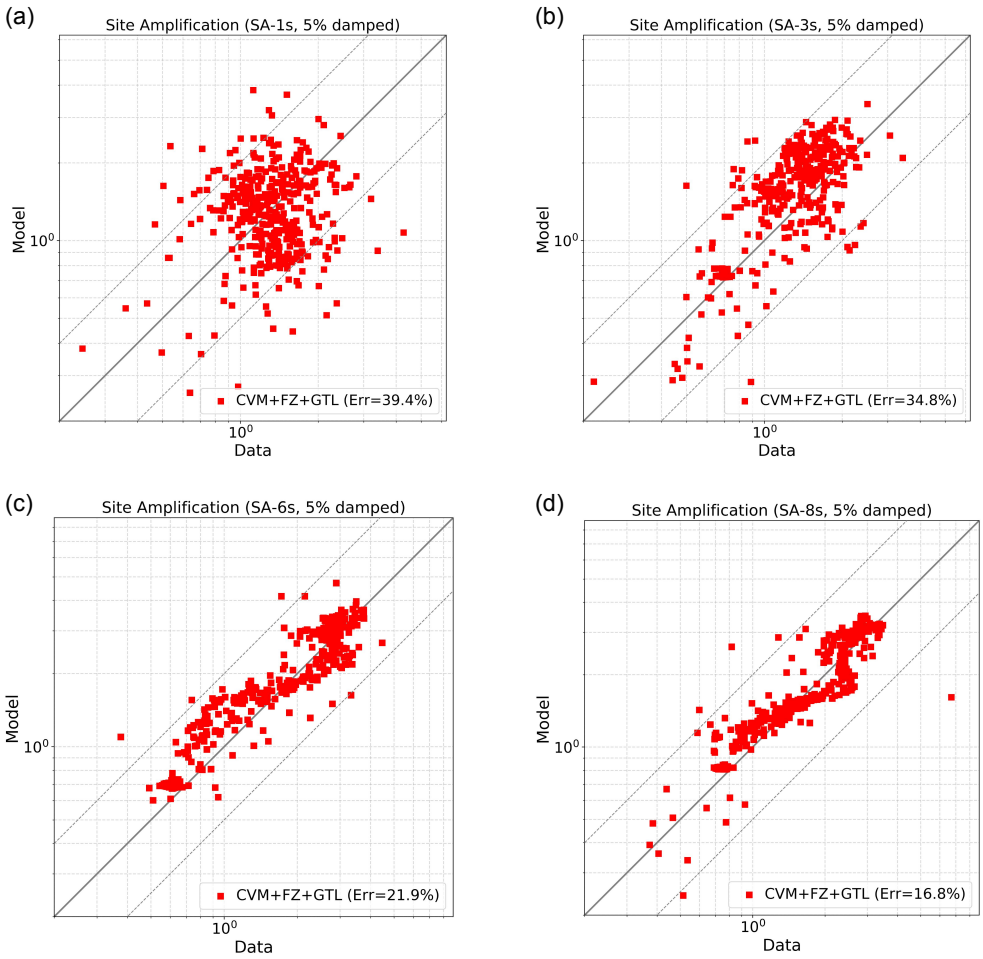

Figure 3.A.2: Observed versus simulated amplification for 5% damped SAs at 1, 3, 6, and 8 s periods. The dashed lines depict factor-of-two prediction error.

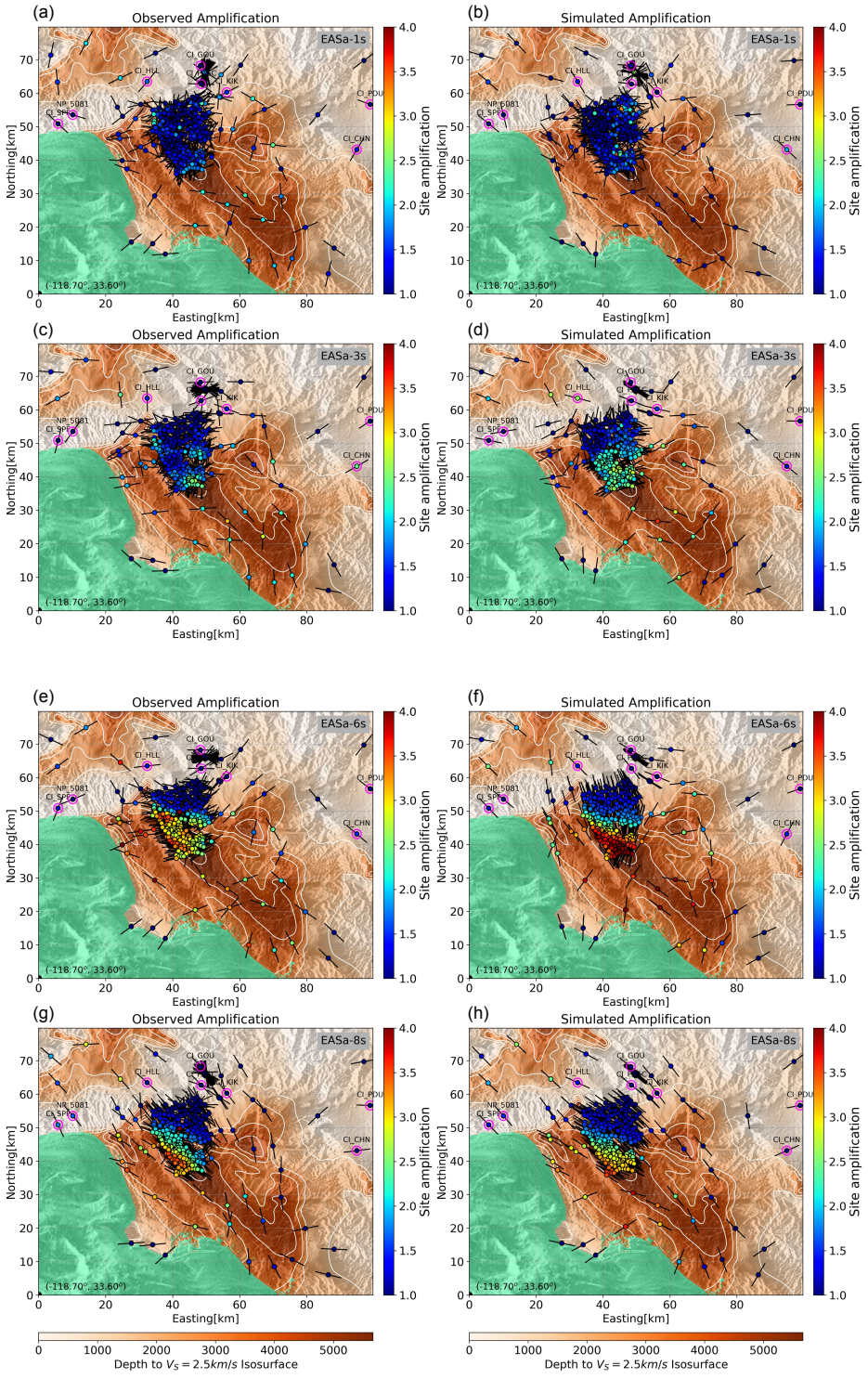

Figure 3.A.3: Maps showing observed (left column) and simulated (right column) site amplification for EAS of horizontal acceleration records at 1 s (a-b), 3 s (c-d), 6 s (e-f), and 8 s (g-h) periods. Straight lines depict the orientations associated with the maximum horizontal ground acceleration for each period.

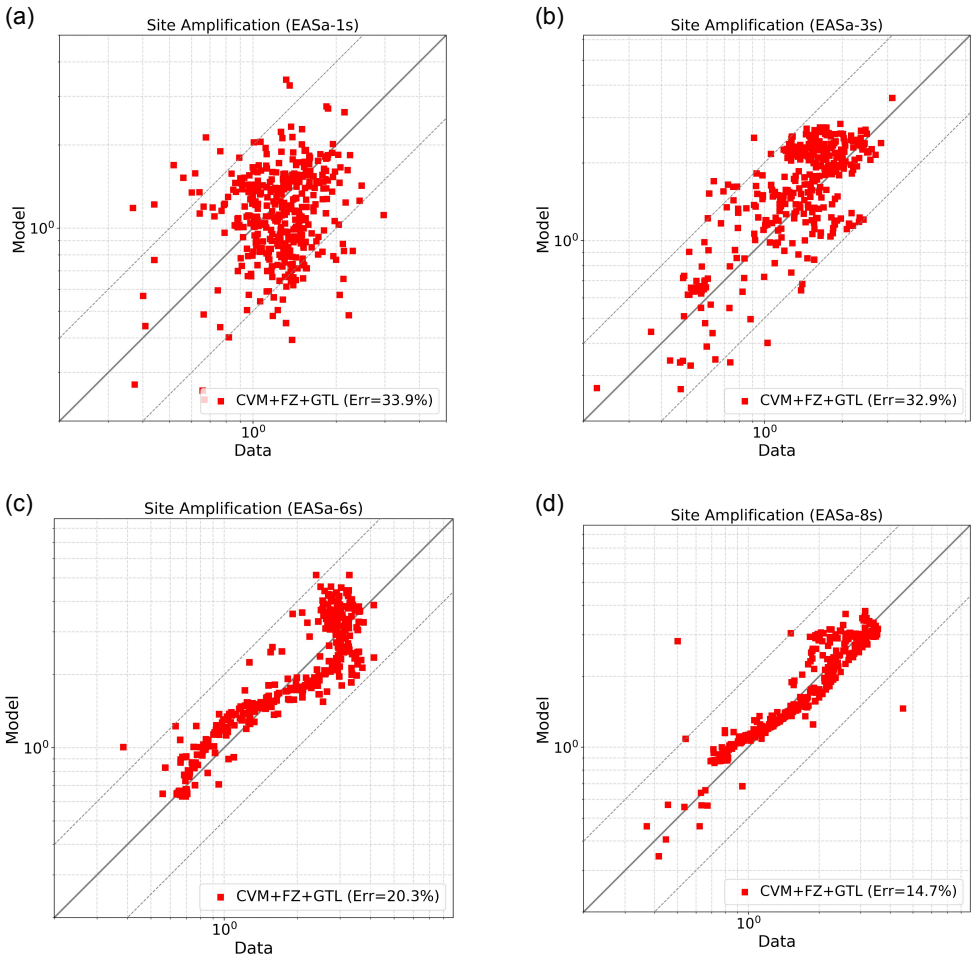

Figure 3.A.4: Observed versus simulated amplifications for EAS of horizontal acceleration records at 1, 3, 6, and 8 s periods. The dashed lines depict the factor-of-two prediction error.

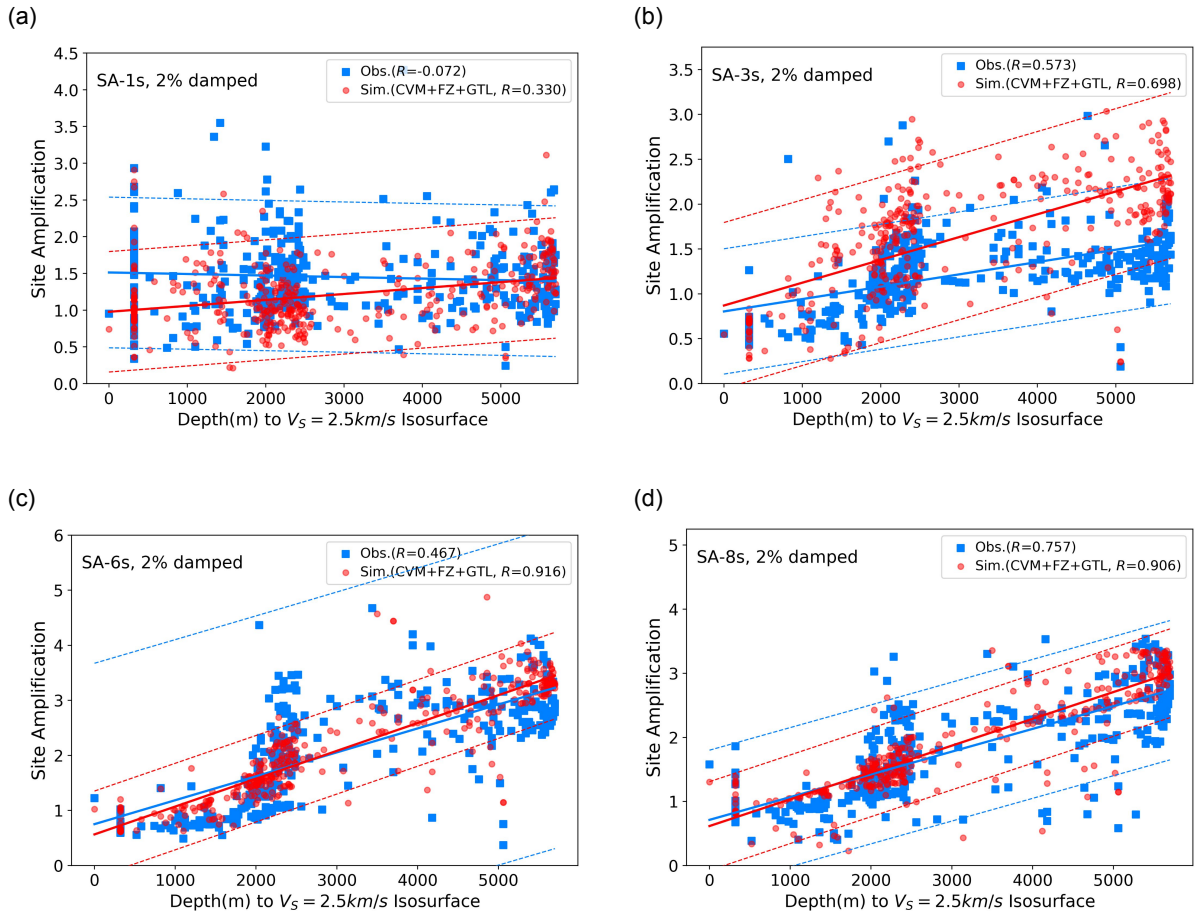

Figure 3.A.5: Same as Fig. 3.5, but where the x-axis is the depth to the V_S=1.5 km/s isosurface.

Chapter 4

Simulation of 0-7.5 Hz deterministic ground motions for Maximum Credible Earthquake scenarios at the Long Valley Dam, CA

Assessment of seismic hazards for embankment dams is a crucial task since failure can have catastrophic consequences. As a case study, we have conducted 3D 0-7.5 Hz deterministic wave propagation simulations to model the seismic response of the Long Valley Dam (LVD) in central California, to estimate peak ground motions and settlements of the dam that can be expected during Maximum Credible Earthquake (MCE) scenarios on the nearby Hilton Creek Fault (HCF). We calibrated the velocity structure, anelastic attenuation model, and the overall properties of the dam via linear simulations of a M_w 3.7 event as well as the 1986 M_w 6.3 Chalfant Valley earthquake constrained by observed ground motions on and around the LVD. We use the Southern California Earthquake Center (SCEC) Community Velocity Model CVM-S4.26M01 superimposed with a geotechnical layer tapered from V_{s30} information from the surface to 700

m depth. We find optimal fit of simulated and observed ground motions at the LVD using frequency-dependent attenuation following a power law, with Q_s/V_S=0.075 for frequencies below 1 Hz (V_S in m/s), and a power-law exponent for frequencies higher than 1 Hz of 0.2. Using the calibrated model for the area, we simulated nonlinear ground motions at the LVD for M_w 6.6 rupture scenarios on the HCF using Drucker-Prager rheology. Nonlinear MCE simulation results show that PGAs higher than 1 g can be expected at the LVD for the southward rupture scenario, which generates the largest ground motion at the dam. Compared with linear ground motion simulation results, nonlinear damping can reduce PGAs predicted for the dam crest by a factor of 2.5. However, the predicted relative displacements of the material inside the dam are relatively small ($\sim 10\ cm$). Larger displacements toward the downstream direction mainly occur around the surface of the dam on the upstream side. The results of the simulations provide useful information for future assessment of structural failure for embankment dams.

4.1 Introduction

Failure of dams during seismic shaking can have devastating societal consequences. While well-designed Earth dams have generally performed well during earthquake ground shaking (FEMA, 2005), catastrophic failures have still occurred due to various reasons, depending on the ground shaking level, structure design, and material properties (FEMA, 2005; Seed *et al.*, 1978). In this work, we have carried out 3D numerical simulations to predict the seismic response of the Long Valley Dam (LVD) for a Maximum Credible Earthquake (MCE). The LVD is a 55-meter high embankment dam located 35 km northwest of Bishop, CA, just east of Sierra Nevada range. The completion of the dam in 1941 created Lake Crowley which has been serving as a storage unit for the Los Angeles aqueduct as well as a flood control unit. The major part of the dam consists of extensive rolled earthfill core (Lai and Seed, 1985). The dam has an array of accelerometers located on the dam crest, downstream wall, and abutment and downstream

bedrock, which provide useful seismic data for studies of seismic response of the dam (Fig. 4.1).

To study the response of an embankment dam under seismic loading, site-specific characteristics must be considered. The seismic response of the LVD has been extensively studied in which the soil behavior was modeled by different approaches. Lai and Seed (1985) accounted for the nonlinear response of the dam materials by using equivalent linear soil properties. Later studies used more rigorous numerical methods (e.g. finite-elements) to simulate the nonlinear hysteretic behavior of the dam materials under cyclic loading with multi-surface plasticity theory (Griffiths and Prevost, 1988; Yiagos and Prevost, 1991; Zeghal and Abdel-Ghaffar, 1992). A potential limitation of the earlier studies is the treatment of the excitation of the dam to estimate the seismic response. Typically, stability analyses for dams use an accelerogram of a historical event, for example, recorded near the downstream base as input motion. Conventionally, the same input ground motion is applied at input nodes along the bottom and sides of the dam, approximating the excitation resulting from a vertically incident plane wave. Such assumption represents an oversimplification, as it does not account for scattering caused by heterogeneities at all scales. In addition, modeling the dam response using existing records usually requires scaling of the amplitudes for different size events, which is now generally a discouraged practice.

The Hilton Creek Fault (HCF) is a significant range-bounding normal fault at the eastern side of the Sierra Nevada. Because it passes just 8 km west of the LVD, it has been identified as a possible source for the MCE that could potentially damage the LVD (Lai and Seed, 1985). Scenario earthquakes on the HCF were also considered in a recent study on earthquake hazards for the Long Valley Caldera-Mono Lake Area by Chen *et al*. (2014). However, the methods used in this study were based primarily on ground motion prediction equations (GMPEs) which provided only peak ground motion amplitudes and spectral accelerations with very limited spatial resolution. In addition, GMPE-based approaches provide only rudimentary control on the effects of source parameters, with no support of physical quantities needed for stability analysis of the dam (e.g., stress, strain, pore pressure effects, etc), or the complete time history of particle

motions (FEMA, 2005). In this study, we utilize the power of supercomputers to address these issues by performing fully-coupled 3D deterministic simulations considering both linear and nonlinear response of the material within the LVD and its surroundings. Our simulation approach enables us to fully account for source, path, and site effects in a single numerical model.

The first part of this study consists of the validation of the velocity model and calibration of the parameters of the attenuation model, geotechnical layer, and 3D structure of the dam. The first validation event is a 2015 M_w 3.7 earthquake located 7 km to the west of the LVD, where we used a point source representation. The second validation used the 1986 M_w 6.2 Chalfant Valley earthquake. We used the Graves and Pitarka (2016) kinematic rupture generator to produce realizations of source models. The second part of this work is to design various rupture scenarios along the HCF which is within 10 km of the LVD, attempting to find the scenario that represents a Maximum Credible Earthquake (MCE) for LVD. The final part of this study is to provide predictions of peak ground motions as well as the relative displacements inside the LVD that can be expected during the proposed M_w 6.6 MCE scenario, considering the nonlinear response of the materials.

4.2 Numerical method

We have carried out the wave propagation simulations in earth models including the LVD up to 7.5 Hz with the 4th order accurate finite-difference code AWP-ODC, with support for surface topography and frequency-dependent attenuation (Olsen, 1994; Cui *et al*., 2010; O'Reilly *et al*., 2021; Withers *et al*., 2015). In order to reduce the computational cost, we used 3 velocity meshes separated vertically with a factor-of-three increase in grid spacing with depth (3.5 m, 10.5 m, and 31.5 m) via a discontinuous mesh approach (Nie *et al*., 2017). We used a minimum shear wave velocity of 175 m/s in the top block, ensuring at least 6.7 points per minimum wavelength (O'Reilly *et al*., 2021).

Support for surface topography is needed to model the seismic response of the LVD. For the validation work of the 2015 M_w 3.7 event, we used the curvilinear grid approach by O'Reilly *et al.* (2021). However, this version of AWP-ODC does not yet support nonlinear soil response calculations. For this reason, we performed the validation with the 1986 M_w 6.2 Chalfant Valley event and simulations of the M_w 6.6 HCF scenarios using a Cartesian grid FD code with a vacuum formulation for the free surface (Randall, 1989; Zahradník *et al.*, 1993; Graves, 1996). These previous studies clearly show that the accuracy of the vacuum formulation is reduced, as compared to explicit free surface formulations. However, we verified the seismic response of the LVD using the vacuum formulation, as compared to those from the curvilinear solution, to ensure that our analysis of the LVD is sufficiently accurate (see Section 4.A.1).

4.3 Velocity model

Our reference model is extracted from the Southern California Earthquake Center (SCEC) Community Velocity Model (CVM) version 4.26-M01 (CVM-S from here on) (Small *et al.*, 2017). It has been shown (Ely *et al.*, 2010; Hu *et al.*, 2022b) that the CVM-S generally causes underprediction of peak amplitudes and coda duration outside the basins, due to unrealistically high near-surface velocities. To alleviate this underprediction, Ely *et al.* (2010) proposed a simple generic overlay-based tapering of time-averaged shear wave velocity (V_S) in top 30 m (V_{S30}) to merge with tomography at a depth of 350 m, which can be applied to any of the velocity models accessible through the SCEC Unified Community Velocity Model (UCVM). Hu *et al.* (2022b) found that applying the taper to deeper depths (700-1,000 m) significantly improved the fit between deterministic synthetics and strong motion data for the 2014 M_w 5.1 La Habra earthquake in the greater Los Angeles area. Following this approach, we estimate the optimal tapering depth for the near-surface material near the LVD in the Sierra Nevada Mts.

For the surface topography, we used the 1m-resolution digital elevation model (DEM)

from the U.S. Geological Survey. This DEM does not provide elevations of areas under water, including part of the upstream face and the entire Lake Crowley. As we needed to include the lake water directly into our simulations, we made the following adjustments to the DEM. First, we removed the lake water from the DEM by manually lowering the elevations of the grids located inside the lake from 2066 m to 2036 m, assuming a flat lake bed and an averaged water depth of 30 m. Secondly, we mirrored the surface elevations of the downstream face to the upstream side with respect to the center line of the crest of the dam (axis of the dam), assuming symmetry of the LVD with respect to the axis of the dam. We then applied Gaussian filters of 7 m resolution to smooth the topography around edges of the area where we removed the lake water, to minimize artifacts introduced by these adjustments. In our calculations, the lake water is modeled as a purely elastic material with V_P=1,050 m/s, V_S=0 m/s, and ρ=1,492 kg/m^3, and the bathymetry of areas under lake water, including the lower portion of the upstream face, are described in staircase fashion.

As expected, CVM-S does not have sufficient accuracy to resolve the velocity structure of the LVD. Earlier studies have modeled the LVD with an extensive rolled earthfill clay core, which constitutes the major portion of the dam structure with a thin layer of more permeable rock-fill shell on top (Lai and Seed, 1985; Yiagos and Prevost, 1991; Griffiths and Prevost, 1988). Based on these studies, we assumed a homogeneous dam for our simulations. We explored different V_S for the homogeneous dam core as well as more complicated descriptions (see Section 4.5.3).

4.4 Anelastic attenuation

In our simulations, we adopted a frequency-dependent attenuation model where Q_s values are given by

$$
\begin{aligned}
Q_s(f) &= Q_{s,0}, \quad f < f_0, \\
Q_s(f) &= Q_{s,0}\left(\frac{f}{f_0}\right)^{\gamma}, \quad f \geq f_0,
\end{aligned}
\tag{4.1}
$$

where the power-law exponent γ, ranging from 0 to 0.9, controls the rate of increase of Q_s above the transition frequency, f_0, set at 1 Hz (Withers *et al*., 2015), and $Q_{s,0}$ is a constant Q_s value. Following Olsen *et al*. (2003), we assumed $Q_{s,0}$ to be proportional to the local S-wave speed, $Q_{s,0} = kV_s$, where k is a parameter specific to the study area. For simplicity, the relationship of $Q_p = 2Q_s$ was assumed throughout this study, following the findings of Olsen *et al*. (2003). The parameters k and γ are estimated in Section 4.5.4.

4.5 Validation I: 2015 M3.7 event

Our first validation event is a M_w 3.7 earthquake from 2015. Due to its small magnitude, it is reasonable to approximate this event as a point source, thereby eliminating uncertainty due to finite fault effects. For this reason, we use this event to constrain the anelastic attenuation parameters for the layers in our model domain. This event has a normal-faulting focal mechanism and is located 7 km to the west of the LVD. The parameters that we used for the simulations can be found in Table 4.2. We use a rotated domain to minimize computational resources when including both the event and the LVD (Fig. 4.2). See Table 4.1 for the configuration of the numerical simulations for the validation. In this analysis we focused on the ground accelerations recorded by strong motion sensors installed on and nearby the dam (structure array 54214, station 54517, and 54933) which are operated under California Strong Motion Instrumentation Program (CSMIP) with a network code CE.

4.5.1 Source description

To describe the source of the M_w 3.7 event, we assume a Brune-type spectral shape (Brune, 1970) with a f^{-2} decay at frequencies above the corner frequency (f_c), given by

$$M(f) = \frac{M_0}{1+(f/f_c)^2}, \tag{4.2}$$

where M_0 is the seismic moment. After Fourier transform of the source spectrum with the constraint of minimum phase, the moment rate function has the following expression in the time domain,

$$M(t) = \frac{t}{T_c^2} e^{\frac{-t}{T_c}}, \tag{4.3}$$

where T_c is the characteristic time controlling the width of the pulse, which depends on the corner frequency $T_c = \frac{1}{2\pi f_c}$. We determined the corner frequency using

$$f_c = k\beta \left(\frac{16}{7} \frac{\Delta\sigma}{M_0} \right)^{\frac{1}{3}}, \tag{4.4}$$

where k is a constant, β is the V_s at the source (3,410 m/s), and $\Delta\sigma$ is the stress drop (Eshelby, 1957; Brune, 1970). Using $k = 0.32$ assuming a circular rupture with a rupture speed of $V_r = 0.9V_s$ (Madariaga, 1976) and a stress drop of 3 MPa (Prejean and Ellsworth, 2001), we get $T_c = 0.0593s$, and $f_c = 2.7Hz$ (Fig. 4.3).

4.5.2 Near-surface geotechnical layer (GTL)

We follow the approach of Hu *et al*. (2022a) and Hu *et al*. (2022b) to calibrate the near-surface velocity structure within our model domain. This calibration entails replacing the velocity model extracted from the SCEC CVM-S, from the free surface to a given tapering depth (z_T) with V_P, V_S, and ρ computed using the formulations of Ely *et al*. (2010) along with local

V_{S30} information. This approach provides a smooth transition between the near-surface velocity structures and the original model. We used the measured V_{S30} values wherever available, and the values from Wills *et al*. (2015) elsewhere.

In order to estimate an optimal value for the tapering depth z_T, we compared simulations for models with GTL implemented with z_T of 350 m, 700 m, and 1,000 m (see Fig. 4.4) to seismic data recorded off the dam (e.g., stations 54517 and 54933). Fig. 4.5 shows that the spectral responses of synthetics computed for the three different values of z_T are indistinguishable with respect to data at station 54933 (see Fig. 4.1 for its location). Based on this analysis, we simply used z_T equal to 700 m in our simulations. This modification resulted in significantly lower V_S values near the surface of the domain as well as a higher degree of spatial complexities compared to CVM-S (Fig. 4.6).

4.5.3 Elastic Properties of the LVD

In order to select the most appropriate values for our analysis, we tested different elastic properties under low-strain conditions for the dam using the M_w 3.7 event, including the homogeneous core and the layered-type structure calculated from the elastic parameters used in the numerical study by Griffiths and Prevost (1988) (see Fig. 4.7). Fig. 4.8 compares the synthetics at the crest center, showing that the presence of a thin shell with low V_S values used in the Griffiths and Prevost (1988)'s modeling overpredicts the observed acceleration amplitudes. On the other hand, our simulations show that using a homogeneous core with V_P=1,000 m/s, V_S=450 m/s, and ρ=2,110 kg/m^3 provides an unbiased prediction of the observed ground motions in both time and frequency domains (Fig. 4.8). Due to its homogeneous nature, this model makes no distinction between core and shell of the dam. We note that this model is fairly close to the actual structure of LVD, as an extensive rolled earthfill clay core constitutes the major portion of the dam structure with a thin layer of more permeable rock-fill shell on top (Lai and Seed, 1985;

Yiagos and Prevost, 1991; Griffiths and Prevost, 1988).

4.5.4 Anelastic attenuation

We carried out a grid search to estimate the values of k and γ described in Section 4.4 that provide the best fit to the strong motion records for the M_w 3.7 event at the LVD. These simulations included the estimated optimal GTL parameters and elastic properties of the dam, with recorded data both on and near the LVD (all sensors shown in Fig. 4.13). As an estimate of goodness-of-fit (GOF) we used the natural logarithm of the observed-to-simulated acceleration Fourier amplitude spectral ratio for all available channels, given by

$$GOF_{FAS}(f) = \ln\left(\frac{FAS_{obs}(f)}{FAS_{model}(f)}\right), \tag{4.5}$$

where $FAS_{obs}(f)$ and $FAS_{model}(f)$ are Fourier amplitude spectra of observed and simualted acceleration waveforms, respectively. Prior to computing the spectral ratio, both $FAS_{obs}(f)$ and $FAS_{model}(f)$ were smoothed with a Savitzky-Golay filter (Savitzky and Golay, 1964) with a 0.5 Hz window length to suppress large fluctuations. We calculated the mean GOF_{FAS} and the corresponding standard deviation at each frequency point between 0.2-7.5 Hz to quantify the model performance. Due to the definition of GOF_{FAS}, a positive value indicates under-prediction and vice versa. In addition, we defined an error value as a summary of the mean GOF_{FAS} over the entire frequency range,

$$Error = \frac{\sum_{i=1}^{Nf} |\mu_i|}{Nf}, \tag{4.6}$$

where μ_i is the mean GOF_{FAS} at frequency point i. The GOF_{FAS} analysis shows a trade-off between the k and γ, where ($k = 0.05$, $\gamma = 0.4$), ($k = 0.075$, $\gamma = 0.2$), and ($k = 0.1$, $\gamma = 0$) result in almost identical GOF_{FAS} curves (Fig. 4.9). Based on this result, we proceeded with an

intermediate model with $k = 0.075$ and $\gamma = 0.2$ in all following simulations.

4.5.5 Validation results

Our numerical simulation was able to generate synthetics that are reasonably close to the data in both time and frequency domains using the point source described in Section 4.5.1 and the model parameters discussed in Section 4.3. The GOF_{FAS} of the full model (red trace in Fig. 4.10) shows no systematic bias where the model without a geotechnical layer clearly underpredicts the spectral energy across almost the entire frequency range. Figs. 4.11 and 4.12 show that the simulated acceleration waveforms and spectra are close to those for the data at various locations of the dam. In summary, the attenuation model using $k = 0.075$ and $\gamma = 0.2$, the homogeneous dam structure with V_P=1,000 m/s, V_S=450 m/s, ρ=2,110 kg/m^3, along with a geotechnical layer in the top 700 m are capable of providing unbiased estimates of the recorded ground motions in both time and frequency domains up to 7.5 Hz.

4.6 Validation II: The 1986 M_w 6.2 Chalfant Valley earthquake

We used the 2015 M_w 3.7 event (Validation I, where finite-fault effects were neglected due its small magnitude) to validate the CVM-S velocity model for the area, calibrate the attenuation model, and confirm the implementation of the near surface geotechnical layers and the 3D structure of the LVD. The model was then used for the second validation event, namely the 1986 M_w 6.2 Chalfant Valley earthquake. This earthquake is located 25 km to the east of LVD, which requires a larger computational domain to accommodate the entire fault and LVD (Fig. 4.13, see Table 4.3 for more details about the simulation domain). The moment magnitude of this event (M_w 6.2) clearly warrants a finite-fault description for its rupture. We use the Graves and Pitarka (2016) kinematic rupture generator, a widely used piece of software implemented on the SCEC

Broadband Platform (Maechling *et al*., 2014), to generate finite-fault descriptions for the Chalfant Valley event, described in the following section.

4.6.1 Finite-fault source model

The hypocenter locations for the Chalfant Valley earthquake reported by previous studies are fairly similar (varying horizontally $\leq$ 1 km), while the interpretation of the focal mechanism and the fault dimensions show larger variation (Smith and Priestley, 2000; Cockerham and Corbett, 1987; Pacheco and Nábělek, 1988; Savage and Gross, 1995). Based on the published focal mechanisms for the event (Cockerham and Corbett, 1987; Pacheco and Nábělek, 1988; Savage and Gross, 1995; Smith and Priestley, 2000), we assume a pure strike-slip focal mechanism in our simulations.

Following the hypocenter location and the interpreted fault length in Smith and Priestley (2000) (13.9 km), we estimated a fault width of 11.6 km using the empirical source scaling relations by Leonard (2014) for a M_w 6.2 event. Using the Graves and Pitarka (2016) kinematic rupture generator, we generated three realizations of slip distributions for the defined fault plane, focal mechanism and hypocenter. The source parameters for this event are listed in Table 4.4, and Fig. 4.14 shows the slip distributions and moment rate functions of the generated source rupture models.

4.6.2 Validation results

We used the model parameters described in Section 4.3 to generate synthetic seismograms for the Chalfant Valley event, e.g., including a GTL tapered to a depth of 700 m below the free surface and a homogeneous dam core with V_S=450 m/s. We found that the three source realizations (see Fig. 4.14) for the Chalfant Valley event result in similar GOF_{FAS} values, where the model predictions are generally unbiased across the entire examined frequency range (Fig. 4.15). As

shown in Figs. 4.16 to 4.18 (only showing seed #2 for demonstration), the source models in Fig. 4.14 generate synthetics that are in reasonable agreement with the data recorded at different locations on the LVD in both time and frequency domains up to 7.5 Hz. The FAS GOF shown in Fig. 4.15 also shows that the three different source realizations generate similar spectral responses, suggesting that the predicted ground motions are insensitive to the choice of random seed number. We note that the Chalfant Valley earthquake validation was carried out using purely elastic rheology, as the PGAs at the dam (about 0.1 g) were deemed insufficient to trigger significant nonlinear soil behavior.

4.7 Hilton Creek Fault scenarios

As shown above, our validations for the M_w 3.7 and the M_w 6.2 1986 Chalfant Valley earthquakes result in well-calibrated velocity and attenuation models for the area. In addition, the results of the modeling of the Chalfant Valley event demonstrate that the Graves and Pitarka (2016) kinematic rupture generator is able to create source descriptions that produce ground motions in agreement with data for frequencies up to 7.5 Hz. We are therefore ready to perform simulations for scenario earthquakes to assess the stability of the LVD. The Hilton Creek Fault (HCF) is a significant range-bounding normal fault at the eastern side of the Sierra Nevada. Because of its closest distance to the LVD of just 8 km, it has been identified as a possible source for the MCE that could significantly affect the stability of the dam (Lai and Seed, 1985; Chen *et al.*, 2014).

4.7.1 Source description

We designed scenarios with M_w 6.6 on the HCF with a fault length of 21 km and a width of 13.3 km estimated using the empirical magnitude-area relations by Leonard (2010). The M_w

6.6 scenario is one of three cases presented in a study by Chen *et al*. (2014) for assessing the seismic hazard of the Long Valley Caldera area associated with the Hilton Creek Fault. In addition to the M_w 6.6 scenario, the study also considered M_w 6.5 and M_w 6.8 scenarios. However, Chen *et al*. (2014) pointed out that the fault rupture for the M_w 6.8 scenario needs to extend into the Long Valley Caldera with a geometry that violates both geologic and kinematic constraints Hill and Montgomery-Brown (2015). Assuming that the hazards to the LVD from the M_w 6.5 are smaller, we chose the M_w 6.6 scenario to represent the MCE. Based on the estimate of Chen *et al*. (2014), the recurrence interval for this scenario is 204 years.

Three different rupture scenarios with the same slip distribution were selected to capture the range of ground motions generated among a southward, northward and a bilateral rupture mode (Fig. 4.19). The hypocenters of all three rupture scenarios are located 6 km down-dip from the top of the fault, all featuring surface ruptures. The source parameters of HCF scenarios are listed in Table 4.6.

4.7.2 Elastic and nonlinear properties of materials

For the HCF simulations we used the SCEC CVM-S with a GTL layer tapered to 700 m, $Q_S = 0.075 V_S f^{0.2}$, and $Q_P = 2Q_S$, the preferred model for the M_w 3.7 and Chalfant Valley earthquake validations. In the HCF scenarios, we included nonlinear response of the materials in our simulations using the Ducker-Prager yield condition (Drucker and Prager, 1952), where the materials behave purely linear until the yield stress is reached.

The implementation of Drucker-Prager plasticity in AWP-ODC is based on the work of Roten *et al*. (2016). The non-associated Drucker-Prager plasticity is regularized using time-dependent relaxation (Andrews, 2005) via the return map algorithm, following the guidelines of the SCEC/USGS (U.S. Geological Survey) dynamic earthquake rupture code verification exercise (Harris *et al*., 2011). The Drucker-Prager yield stress $Y(\sigma)$ is defined as

$$Y(\sigma) = max(0, c\ cos\phi - (\sigma_m + P_f) sin\phi) \tag{4.7}$$

where c is the cohesion, ϕ is the friction angle, P_f is the fluid pressure, and σ_m is the mean stress $\frac{1}{3}(\sigma_{xx} + \sigma_{yy} + \sigma_{zz})$. Eq. (4.7) includes the hydrostatic condition for the fluid pressure, linearly increasing with depth below the water level. The water level inside the dam follows the pre-defined phreatic line shown in Fig. 4.20. We set P_f=0 for all material above the phreatic line inside the dam.

For the material within the dam, we assumed a cohesion of 45 *kPa* and a friction angle $\phi = 39^o$, as was used for the core material as described in Griffiths and Prevost (1988). To determine the yield stress of material off the dam, we adopted the generalized Hoek-Brown failure criterion that conveniently provides the effective cohesion and a friction angle needed for the Drucker-Prager yield condition (Hoek *et al*., 2002). The Hoek-Brown failure criterion uses a Geological Strength Index (GSI) value for each material. As the mechanical properties of near-surface material are poorly constrained, we make the assumption that GSI is correlated with the local shear wave speed (V_S). The V_S and GSI measurements for rock samples in southern California by Townsend *et al*. (2021) (Figure 5 of their study) illustrate the relationship between these two quantities. Their analysis shows that (1) rocks with V_S of 200-300 m/s can be characterized by a GSI of 20, (2) GSI of rock samples with V_S of 300-500 m/s fall in the 20-40 range, and (3) rocks with V_S of 1,500 m/s are usually associated with GSI values of $\sim$90. Based on these observations, we first assigned each material into a category based on its S-wave speed, and used the corresponding relationship to compute the GSI value:

$$GSI = \begin{cases} 20 & \text{if } V_S < 300m/s \\ 20 + (V_S - 300) \times \frac{40-20}{500-300} & \text{if } 300m/s \leq V_S < 500m/s \\ 40 + (V_S - 500) \times \frac{90-40}{1500-500} & \text{if } 500m/s \leq V_S < 1500m/s \\ 90 + (V_S - 1500) \times \frac{100-90}{2000-1500} & \text{if } 1500m/s \leq V_S < 2000m/s \\ 100 & \text{if } V_S \geq 2000m/s \end{cases}$$

4.7.3 HCF Scenario Ground Motion Results

We performed both linear and nonlinear simulations for the proposed HCF scenarios, in order to quantify the latter effects. Figs. 4.A.4 to 4.A.6 show comparisons of 0.25-7.5Hz synthetics computed by linear simulations for the three proposed HCF rupture scenarios at different locations on and around the dam. The results show that the variation of hypocenter location can cause variation of PGA predicted at the crest top by a factor of 1.5 (Fig. 4.A.6). The southward rupture scenario is found to produce the largest PGAs at the center of the dam crest. The predicted ground accelerations are lower around the downstream base ($\sim$ 1.5 g) as compared to the dam crest, which demonstrates that the structure of the dam itself amplifies the ground motion by a factor of 2 or more. Given that the southward rupture scenario produces the largest ground motions overall, we focus on this scenario in the following analysis.

Figs. 4.21 to 4.23 illustrate the differences between the linear and nonlinear (Ducker-Prager rheology) behavior at 3 sensor locations for the southward HCF rupture scenario. Notice the strong reduction of the PGAs due to nonlinear response of the material, up to a factor of 2.5, where we predict stronger reductions on the dam as compared to off the dam (e.g., CH6, 7, and 8 in Fig. 4.23 versus CH11, 12, and 13 in Fig. 4.21). These results indicate that nonlinear effects are significantly affecting the ground motions at the LVD.

We illustrate the ground motion response of the dam for the HCF scenarios along a 2D

transect across the dam (white line crossing the dam in Fig. 4.1). Fig. 4.24 shows that both PGVs and PGAs are amplified along the surface of the dam. The largest PGVs occur at the center crest while the largest PGAs are found in the middle of the downstream face, in particular in the region between the downstream face and the phreatic line. This is expected as the material above the phreatic line is exposed to less nonlinear damping due to lack of fluid pressure, and therefore stronger ground motions. Also notice the 50 m by 20 m zone of elevated PGAs at the base of the dam, right beneath the crest, likely originating from interaction between the dam and the underlying materials.

Settlement of the dam after a seismic event is crucial information for evaluating dam stability. We computed the relative displacements inside the dam along the 2D transect with respect to a control point below the lake as a proxy of the settlements (Fig. 4.25). Our simulation predicts primarily east-southeastward movement of the material on the upstream face by approximately 10 cm with 3 cm south-southwestward movement near the crest, and very little uplift of displacements with respect to the control point ($< |2|$ cm). The spatial extent of the relative horizontal movement of the LVD is confined to the upper half of the dam. The maximum displacements are about 0.2% of the height of the LVD.

In addition to settlement of the LVD, we followed the approach in Ma *et al*. (2000) to calculate the accumulated strain values, η (Fig. 4.26). As mentioned in Ma *et al*. (2000), this quantity is a good representation of actual material damage since it is the cumulative norm of the strain-tensor increments throughout the simulation and thus does not decay through time. The largest cumulative strain occurs in the upstream part of the dam, and areas of the downstream side, near the surface of the upstream and downstream faces, with values up to about 1%. Since the calculation includes all of the dynamic strain, the values in Fig. 4.26 are expected to be larger than the strain computed from the final permanent displacement field.

To further assess the response of the LVD during the MCE scenario, we extracted synthetic waveforms every 7 m along a vertical array from the top to the base of the dam (see Fig. 4.27). As

can be seen in the horizontal motions (Figs. 4.A.7 and 4.A.8), the high-frequency signal present in both acceleration and velocity waveforms at the bottom of the dam (elevations 2017 m and 2024 m) gradually vanishes toward the crest top, where the amplitude first decreases between 2017 m and 2045 m, and then increases by nearly a factor of 2 from 2045 m to 2073 m (crest). Figs. 4.28 to 4.30 show acceleration and velocity waveforms, comparison of linear and nonlinear waveforms at the surface, and FAS at three select locations along the array. The depletion of high frequency waves is clear when comparing waveforms and spectra of the records at 2017 m, 2045 m, and 2073 m in Figs. 4.28 and 4.29. The FAS show that the elevated energy between 4-6 Hz in the waveforms at 2017 m is absent in the record at 2045 m, while the energy between 2-4 Hz is enhanced in the 2045 m record. The migration of energy from high to low frequency is a result of nonlinear soil behavior. Approaching the crest top, the seismic waves are further amplified by the shape of the dam structure at frequencies above 2 Hz. On the other hand, the vertical ground motions show increased amplitudes approaching the crest top without the high frequency energy depletion found on the horizontal components. The reason for this is likely that the vertical component primarily contains P-waves which are less likely to trigger nonlinearity (Figs. 4.A.9 and 4.30). Our results show that the combined effects of nonlinearity and the structure of the dam result in complex ground motion patterns inside the LVD.

4.8 Discussion and conclusions

The goal of this study is to predict broadband (0-7.5 Hz) ground motions at the Long Valley Dam for MCE scenarios that are expected to significantly affect the stability of the dam. To ensure that our predicted ground motions are accurate, we first conducted two validations, namely using (1) a 2015 M_w 3.7 event with a point source representation and (2) the 1986 M_w 6.2 Chalfant Valley earthquake modeled by finite-fault sources. During the first validation (Section 4.5), we calibrated the tapering depth for the near-surface GTL representation to z_T=700 m, with relatively

small differences for z_T between 350-1000 m. Furthermore, we estimated optimal parameters k=0.075 and γ=0.2 for $Q_s(f) = kV_S f^{\gamma}$ (V_S in m/s), as well as for the velocity structure of the dam. Using these calibrated models, we showed that the our numerical simulation results can generate 0-7.5 Hz wavefields that are in good agreement with data. Finally, we successfully extended the validation to finite-fault sources for the 1986 Chalfant Valley event (Section 4.6) using the Graves and Pitarka (2016) kinematic rupture generator.

Very limited direct measurement of the material properties of the LVD is available. A numerical study on the seismic response of the LVD by Yiagos and Prevost (1991) used an exponential function to assign V_S increasing with depth. On the other hand, Griffiths and Prevost (1988) assigned material properties to discrete layers of the dam, including a thin, shallow layer representing the rock shell. Our simulations using the elastic parameters adopted in these studies significantly overpredicted the peak seismic amplitudes on the dam, due to the presence of material with low seismic speed at the shallowest depth. A possible explanation for this discrepancy is that V_S of the rock shell has increased over time due to variation of the water level (Clariá and Rinaldi, 2007; Dong and Lu, 2016) or internal deterioration. However, future work is needed to address this issue, such as shallow seismic surveys on the dam.

Based on the validations, we simulated both linear and nonlinear (Drucker-Prager rheology) ground motions for a series of MCE rupture scenarios on the HCF, which is located within 8 km of the LVD. The southward rupture scenario generated the largest ground motions around the LVD, with PGAs exceeding 1 g considering the nonlinear rheology. However, plastic behavior in the LVD reduced PGVs and PGAs at the crest top by up 2.5 times, with a highly complex wavefield. This reduction factor is similar to that found by Roten *et al*. (2014).

The effects on ground motions due to nonlinearity are expected to vary significantly with the nonlinear properties of the material, as shown by Roten *et al*. (2014) and Roten *et al*. (2018). For this reason, we performed additional simulations with different cohesion values (c) and friction angles (ϕ) to estimate the variation of predicted ground motions due to uncertainties

associated with the nonlinear properties of the LVD. Fig. 4.A.10 compares nonlinear synthetic waveforms for the center crest computed with different combinations of c and ϕ. Assuming that the cohesion used in our MCE simulation (c=45 kPa) is an upper bound for compacted clay, we considered two low-cohesion scenarios of c=20 kPa along with friction angles of 20^o and 30^o. The results of these simulations suggest another 30-40% reduction of horizontal PGAs when using lower cohesion, while the vertical motions appear mostly insensitive to the nonlinear parameters. Future studies should focus on acquiring more robust constraints on nonlinear properties of the studied structures. Finally, the simulations predict relatively small ($\sim$ 10 cm) settlements of the dam, with the largest displacements near the surface of the upstream side.

In summary, our research on the LVD has established a procedure for model calibration in order to simulate high-frequency waves, particularly useful for somewhat poorly constrained velocity models. Our simulations at the LVD are in agreement with data in the linear regime, and produce nonlinear response using the Drucker-Prager approach, in a range expected from other numerical analyses. In future work, we recommend that that a fully hysteretic nonlinear analysis be carried for the LVD MCE scenarios, in order to evaluate the stability of the dam.

Acknowledgements

This research was supported through the California Geological Survey (Award #1020-006). Chapter 4, in full, is a reformatted version of a paper currently in preparation for submission for publication: Yeh, T.-Y. and Olsen, K.B. (2022), Simulation of 0-7.5 Hz Deterministic Ground Motions for Maximum Credible Earthquake Scenarios at the Long Valley Dam, CA. The dissertation author was the primary investigator and author of this paper.

Tables and Figures

Table 4.1: Simulation parameters for the 2015 M_w 3.7 event validation

Domain		
Length		19.65 km
Width		15.12 km
Depth		14.98 km
Southwest corner		$-118.86738^o, 37.53854^o$
Northwest corner		$-118.84244^o, 37.67329^o$
Southeast corner		$-118.64744^o, 37.51255^o$
Northeast corner		$-118.62211^o, 37.64726^o$
Rotation angle		9.51^o clockwise from north
Spatial resolution		
Maximum frequency		7.5 Hz
Minimum V_S		175 m/s
Points per minimum wavelength		6.7
Grid spacing	3.5 m	Free surface to 5.03 km below sea level
	10.5 m	5.00 km to 6.00 km below sea level
	31.5 m	5.93 km to 14.97 km below sea level
Temporal resolution		
Time step		0.0002 s
Simulation time		20 s

Table 4.2: Source parameters for the 2015 M_w 3.7 event

Hypocenter location	$Lon.: -118.7878^o \quad Lat.: 37.5975^o \quad Depth: 4.8km$
Origin time	2015-08-22 13:34:48 UTC (USGS)
Seismic moment	4.678×10^{14} Nm (USGS)
Focal mechanism	Plane 1:$158^o/75^o/-103^o$ Plane 2: $20^o/20^o/-50^2$

USGS: U.S. Geological Survey earthquake report

Table 4.3: Simulation parameters for the 1986 M_w 6.2 event validation

Domain		
Length		52.92 km
Width		31.75 km
Depth		30.75 km
Southwest corner		$-118.87550^o, 37.44691^o$
Northwest corner		$-118.81336^o, 37.72868^o$
Southeast corner		$-118.28703^o, 37.36313^o$
Northeast corner		$-118.22272^o, 37.64463^o$
Rotation angle		11.08^o clockwise from north
Spatial resolution		
Maximum frequency		7.5 Hz
Minimum V_S		175 m/s
Points per minimum wavelength		6.66
Grid spacing	3.5 m	4.38 to 0.35 km above sea level
	10.5 m	0.38 km above sea level to 5.66 km below sea level
	31.5 m	5.59 km to 30.75 km below sea level
Temporal resolution		
Time step		0.00027 s
Simulation time		30 s

Table 4.4: Source parameters for the 1986 M_w 6.2 Chalfant Valley earthquake

Hypocenter location[a]	$Lon.: -118.4408^o \quad Lat.: 37.5333^o \quad Depth: 10.8km$
Origin time[b]	1986-07-21 14:42:26 (UTC)
Seismic moment[c]	2.65×10^{18} Nt-m
Focal mechanism	strike/dip/rake=$150^o/55^o/-180^o$
Fault dimensions[d]	Length=13.9 km Width=11.6 km

[a]: Smith and Priestley (2000)

[b]: USGS, U.S. Geological Survey earthquake report

[c]: GCMT, Global CMT project

[d]: Leonard (2010) and Smith and Priestley (2000)

Table 4.5: Simulation parameters for the Hilton Creek fault M_w 6.6 MCE scenarios

Domain		
Length		28.72 km
Width		40.82 km
Depth		30.68 km
Southwest corner		$-118.84019^o, 37.37252^o$
Northwest corner		$-118.96107^o, 37.72752^o$
Southeast corner		$-118.52681^o, 37.43966^o$
Northeast corner		$-118.64633^o, 37.79500^o$
Rotation angle		14.01^o counterclockwise from north
Spatial resolution		
Maximum frequency		7.5 Hz
Minimum V_S		175 m/s
Points per minimum wavelength		6.66
Grid spacing	3.5 m	4.23 km above sea level to 0.24 km below sea level
	10.5 m	0.22 km to 2.56 km below sea level
	31.5 m	2.49 km to 30.68 km below sea level
Temporal resolution		
Time step		0.00027 s
Simulation time		40 s

Table 4.6: Source parameters for the Hilton Creek fault M_w 6.6 MCE scenarios

Hypocenter location	Southward rupture: $Lon.: -118.7638^o$ $Lat.: 37.6347^o$ $Depth: 4.8$ km Bilateral rupture: $Lon.: -118.7481^o$ $Lat.: 37.5813^o$ $Depth: 4.6$ km Northward rupture: $Lon.: -118.4408^o$ $Lat.: 37.5291^o$ $Depth: 4.3$ km
Focal mechanism[a]	strike/dip/rake=$348^o/50^o/-90^o$
Fault dimensions[b]	Length=21 km Width=13.3 km

[a]: U.S. Geological Survey Quaternary fault and fold database (Haller *et al*., 2004)

[b]: Leonard (2010)

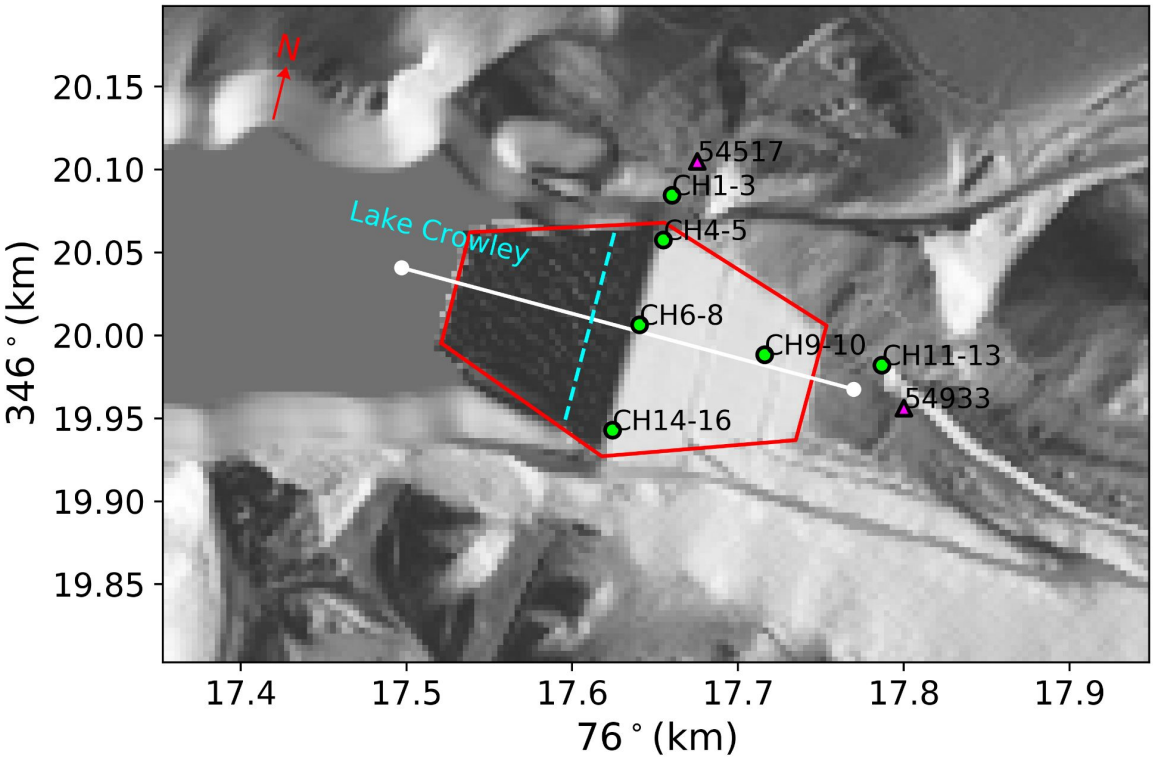

Figure 4.1: Map view of the Long Valley dam. Blue dashed line depicts the contact of lake water surface on the upstream face. Green-filled circles are sensor locations of the structure array (station code 54214) installed on LVD. Magenta triangles are the nearby stations, which were used for estimating the GTL tapering depth (more details in Section 4.5.2).

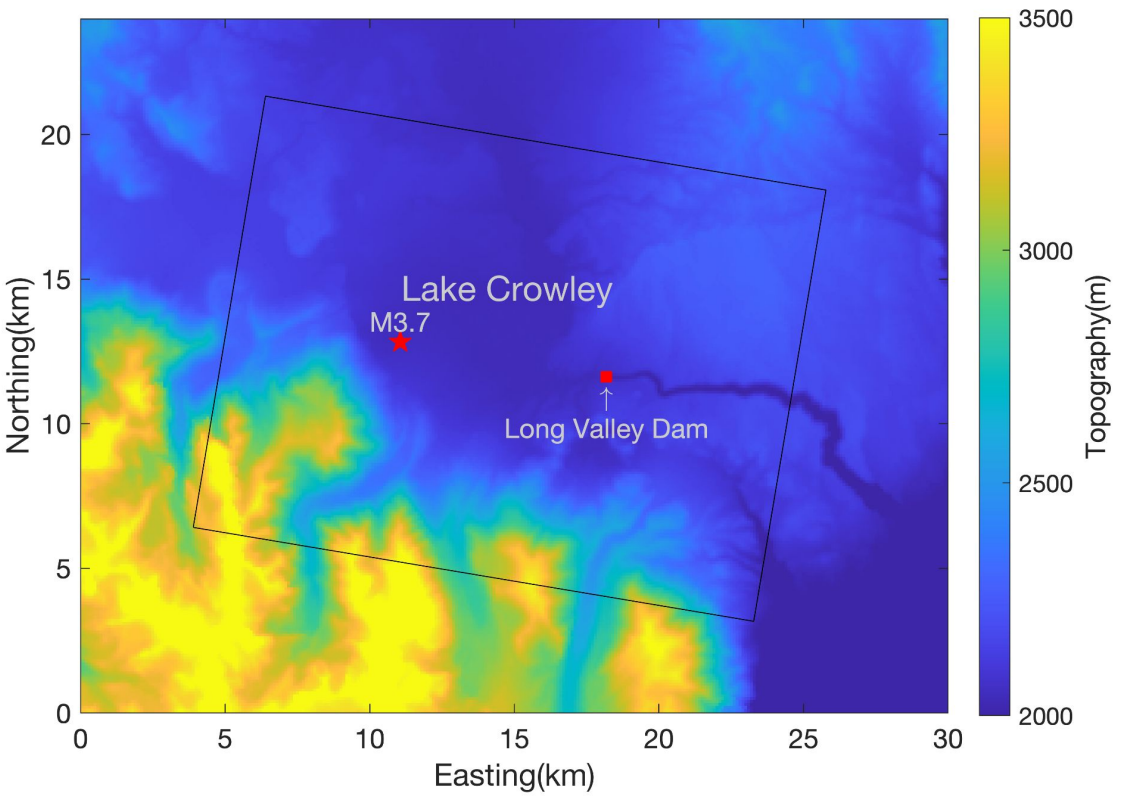

Figure 4.2: Model domain (black rectangle) for the simulations of the 2015 M_w 3.7 earthquake.

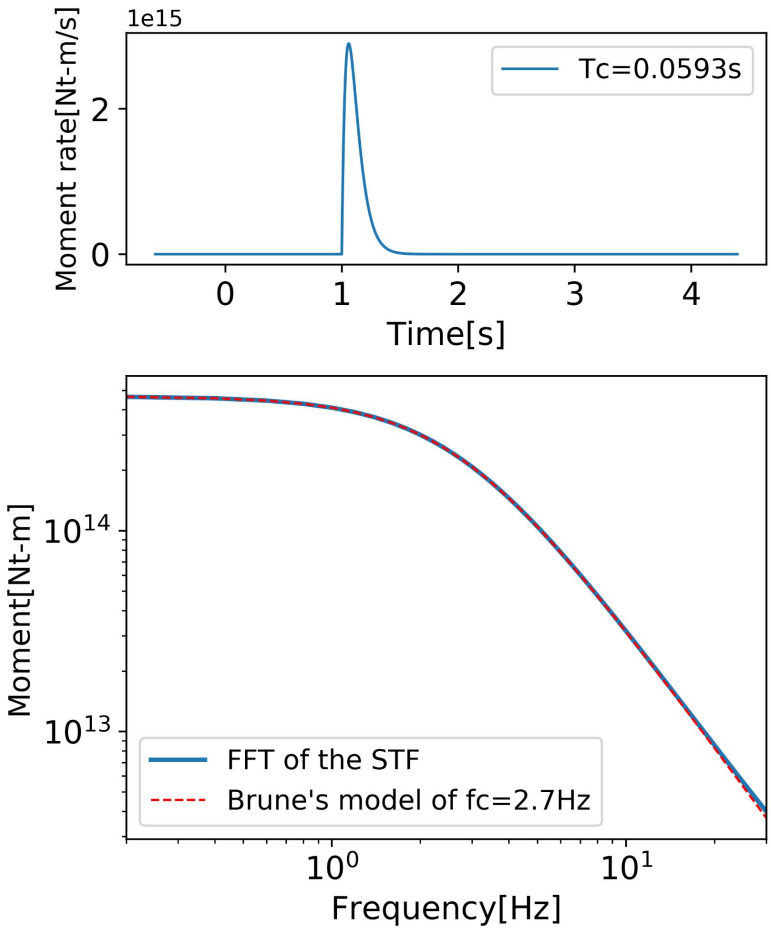

Figure 4.3: Moment-rate function for the 2015 M_w 3.7 earthquake (top) and its FAS (bottom). Red dashed spectrum was computed directly using Brune's model in Eq. (4.2) for comparison.

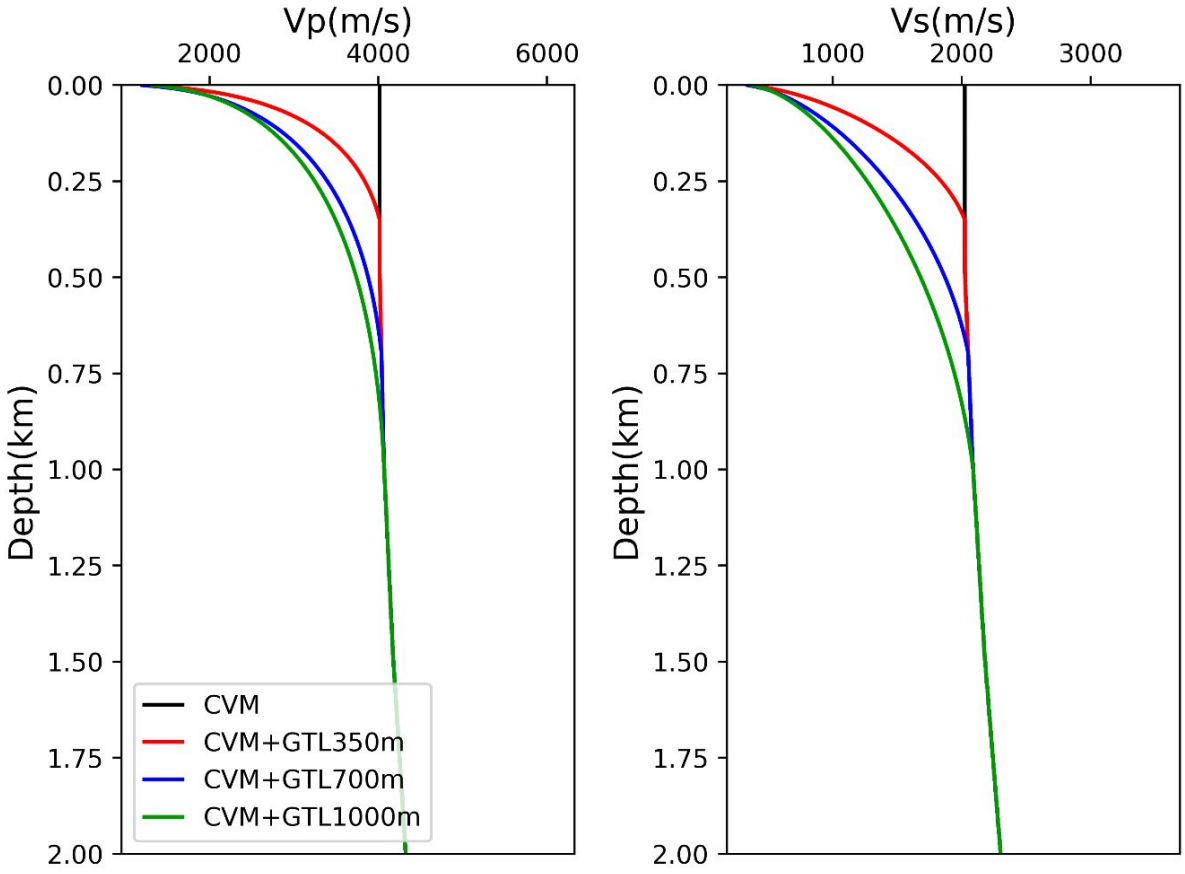

Figure 4.4: Comparison of 1D V_P and V_S profiles beneath station 54933, a site located near the downstream base of the LVD, extracted from the model with GTL tapered to (red) 350 m, (blue) 700 m, and (green) 1000 m and the one without GTL (black).

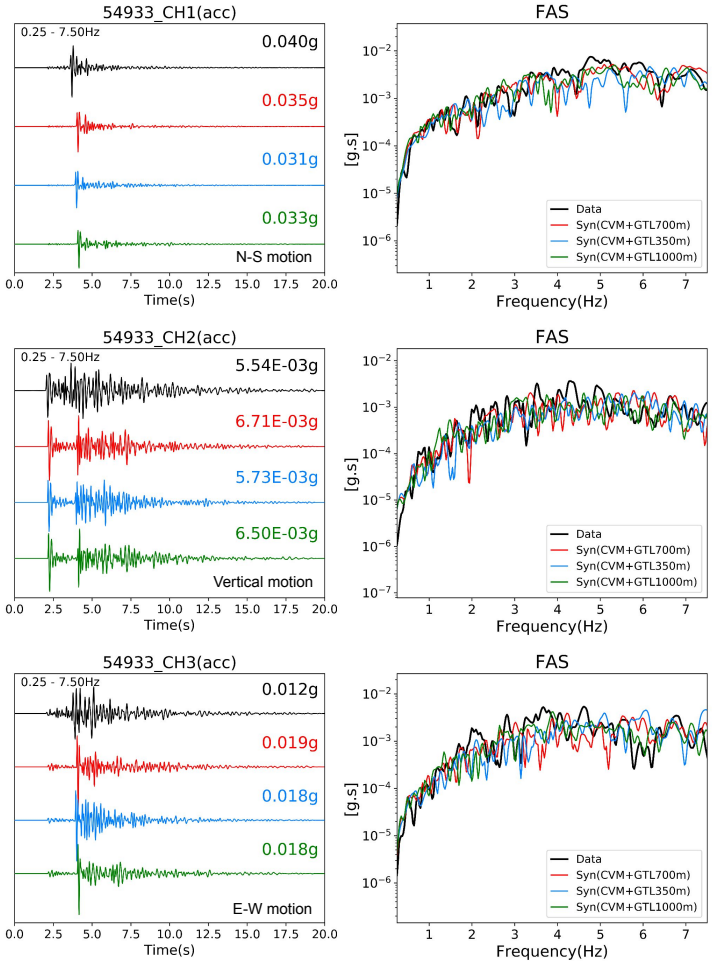

Figure 4.5: Comparison of data (black traces) and synthetics in the time and the FAS domain at station 54933. Synthetics were computed for the model with GTL tapered to (red) 700 m, (blue) 350 m, and (green) 1000 m.

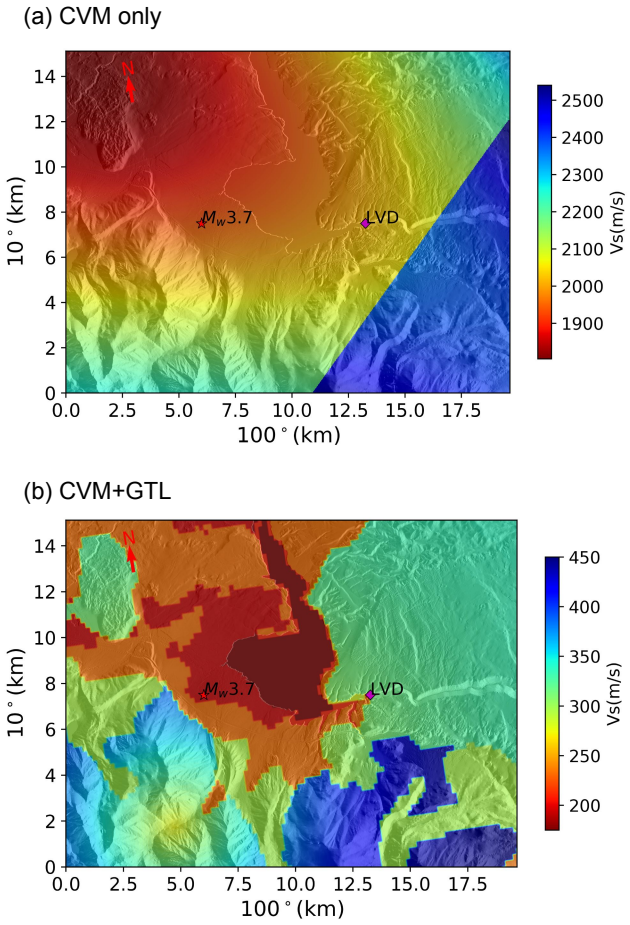

Figure 4.6: Comparison of surface V_S in the model domain for the 2015 M_w 3.7 earthquake. Top panel shows the model with CVM-S only, where bottom panel displays the model with CVM-S and GTL.

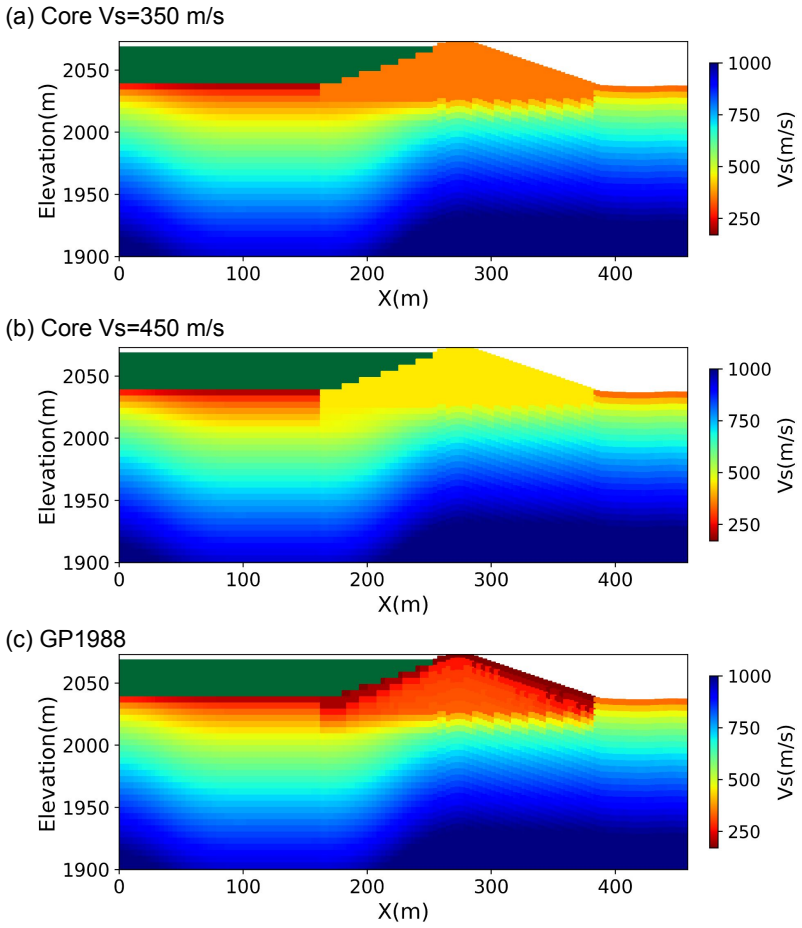

Figure 4.7: 2D V_S transects across LVD extracted from the three different dam models tested in this study. Dam core in models (a) and (b) is homogeneous, whereas (c) has a layered structure computed from the elastic parameters used in Griffiths and Prevost (1988).

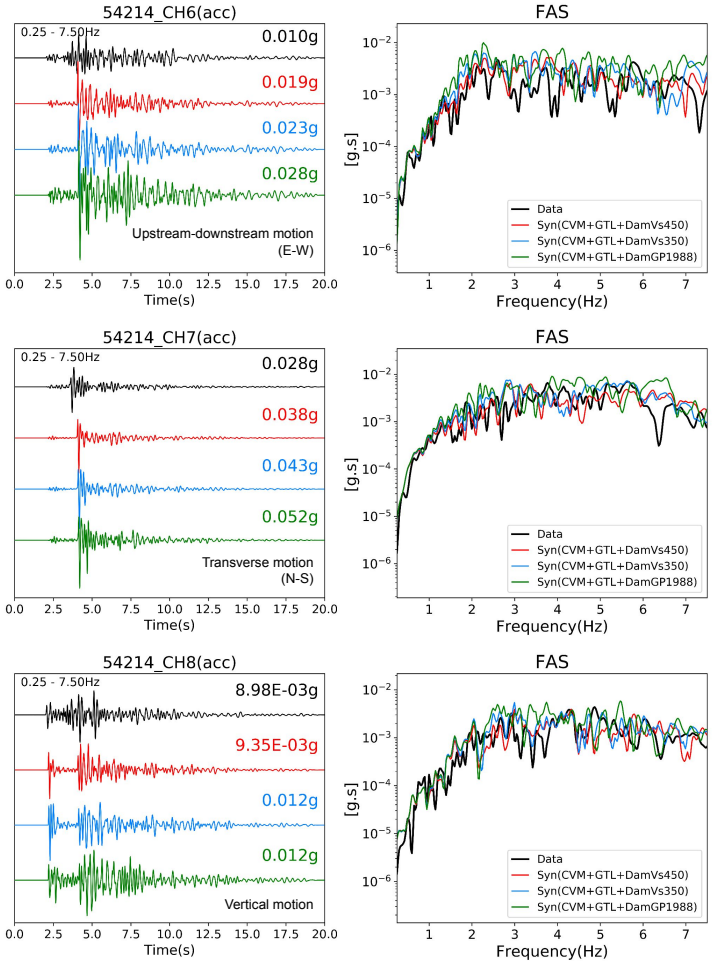

Figure 4.8: Comparison of data (black traces) and synthetics in the time and the FAS domains at sensors located at the crest center (See Fig. 4.1 for sensor location). Synthetics were computed for three dam core models shown in Fig. 4.7, including two homogeneous core models of V_S=450 m/s (red) and V_S=350 m/s (blue), and a layered core model (green).

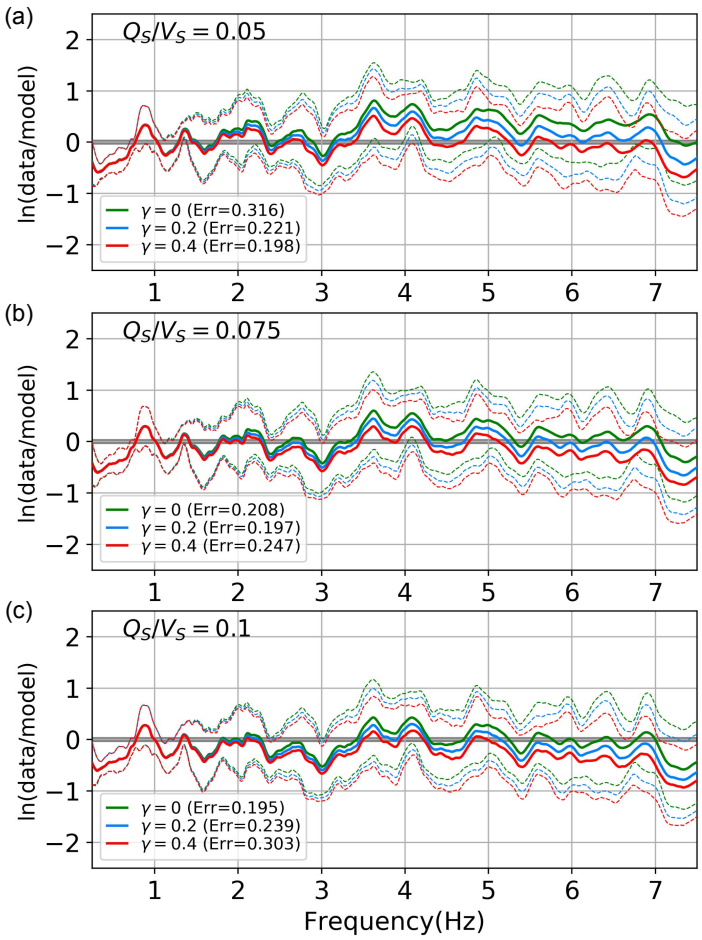

Figure 4.9: 0-7.5 Hz mean GOF_{FAS} for simulations with different combinations of $Q(f)$ parameters. GOF_{FAS} for γ of 0, 0.2, and 0.4 are compared for different Q_S/V_S values. Dashed lines depict one standard deviation.

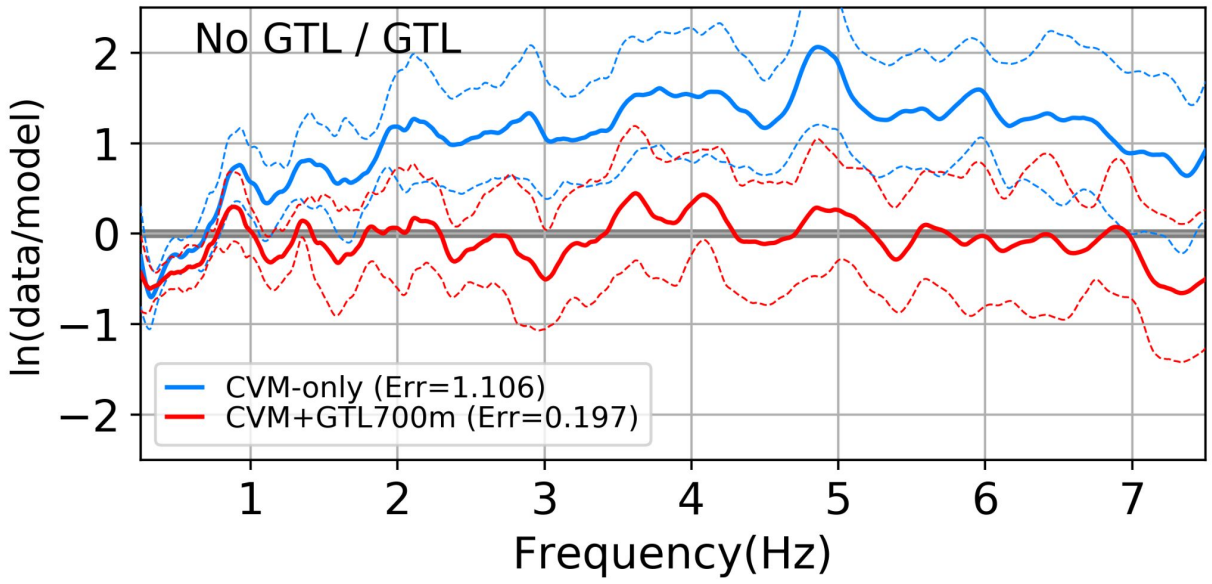

Figure 4.10: Comparison of 0-7.5 Hz mean GOF_{FAS} for simulations (red) with and (blue) without GTL tapered to 700 m below the free surface. Dashed lines depict one standard deviation.

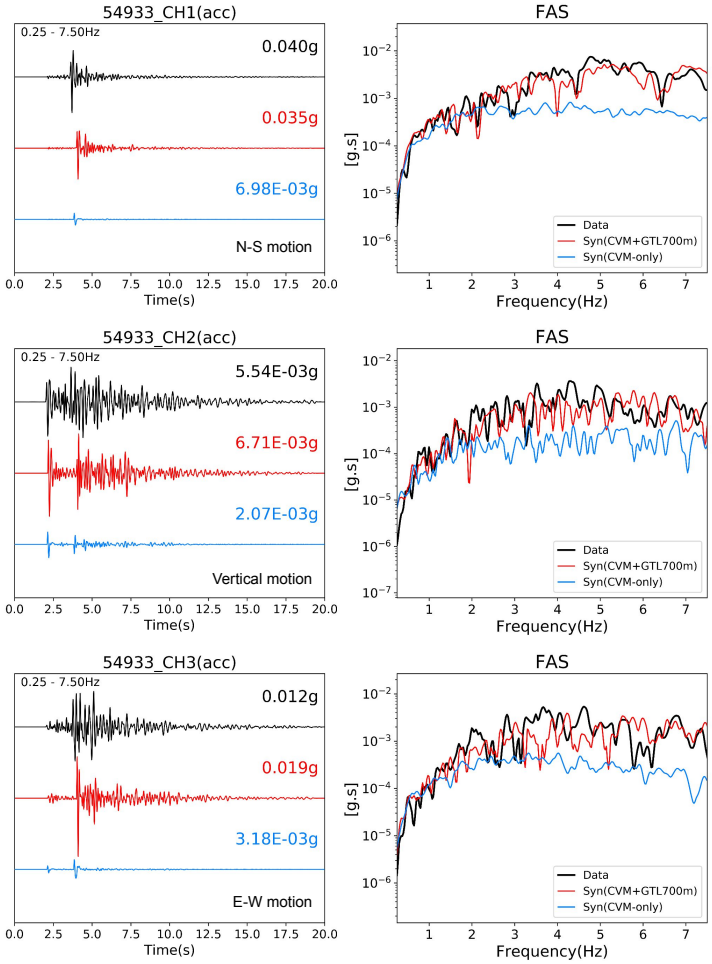

Figure 4.11: Comparison of data (black traces) and synthetics (red and blue traces) in the time and FAS domains at sensors located near the downstream base (See Fig. 4.1 for sensor location). The red synthetic traces were computed with CVM-S, a GTL tapered to 700 m below the free surface, and a dam core with 450 m/s, whereas the blue traces were computed with CVM-S only.

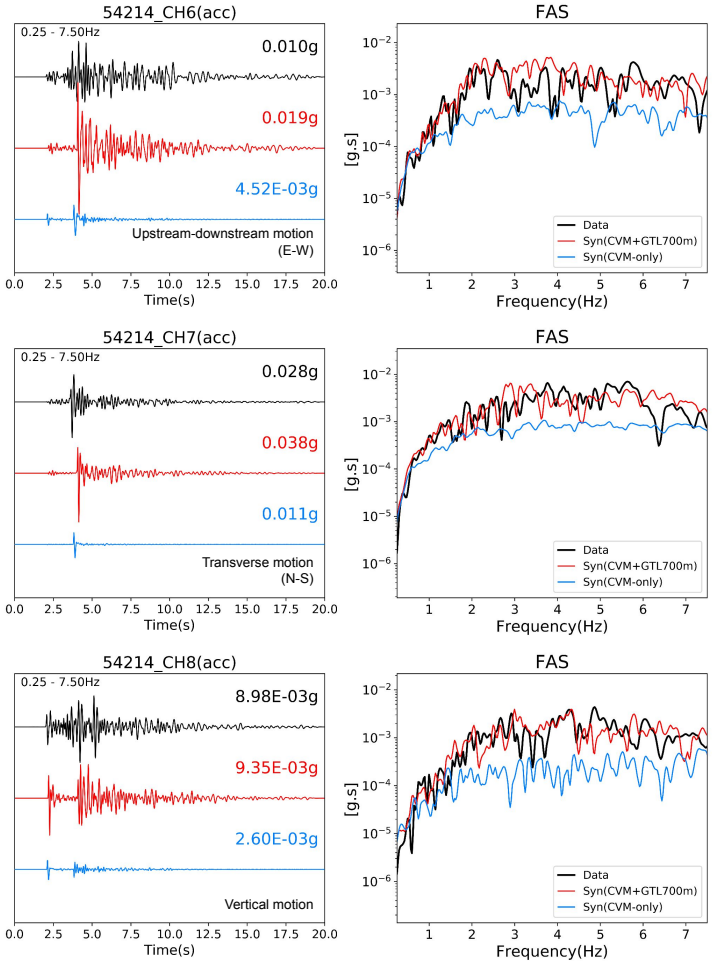

Figure 4.12: Same as Fig. 4.11, but for the sensors located at the crest center (See Fig. 4.1 for sensor location) .

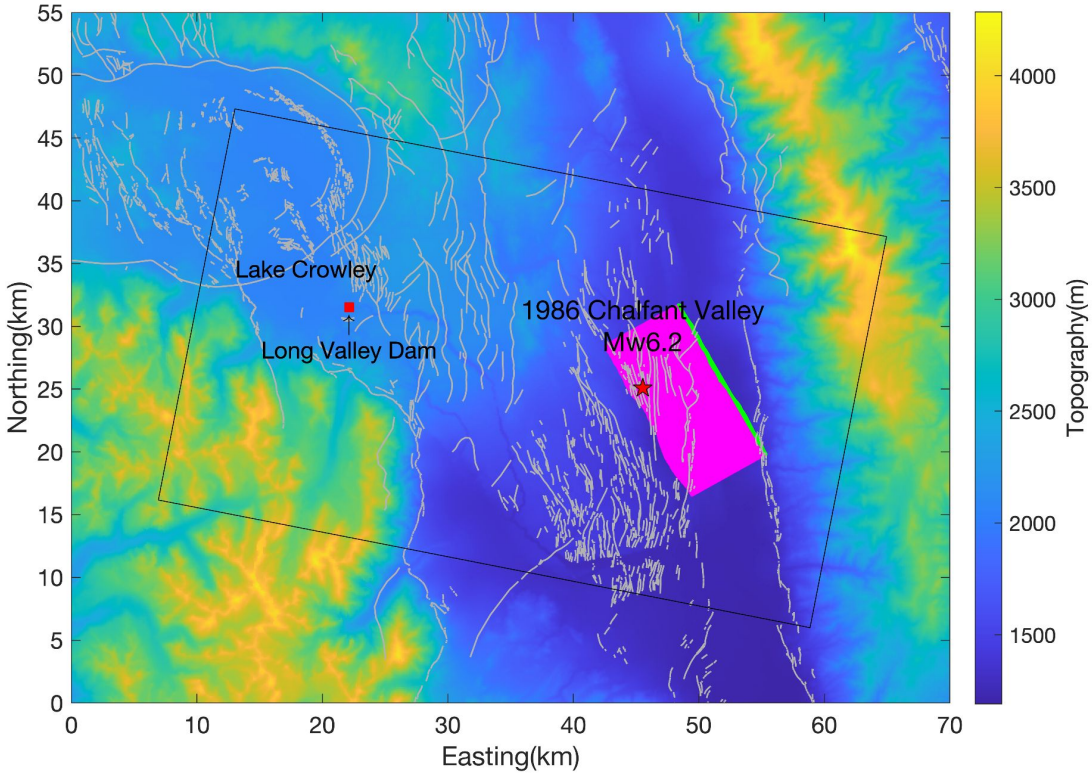

Figure 4.13: Location map for the simulation domain of the 1986 M_w 6.2 Chalfant Valley earthquake. The black box depicts the simulation domain for the earthquake. The pink area shows the surface projection of our finite fault source for the event, the red star shows the epicenter location and the green line depicts the top edge of the fault plane at 2.5 km depth. Green triangles depict station locations.

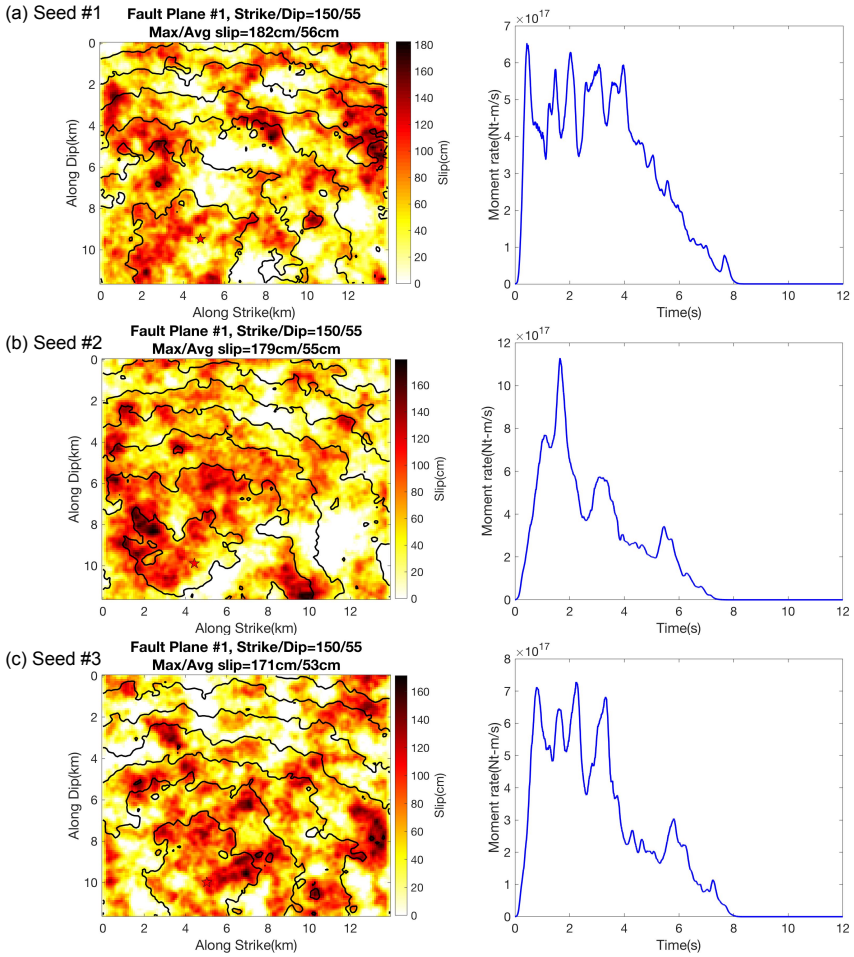

Figure 4.14: (left) Slip distribution and (right) moment rate function of the three realizations of rupture models generated by the Graves and Pitarka (2016) kinematic rupture generator for the 1986 M_w 6.2 Chalfant Valley earthquake. The red star depicts the hypocenter location. The top of the fault is located at 2.5 km depth.

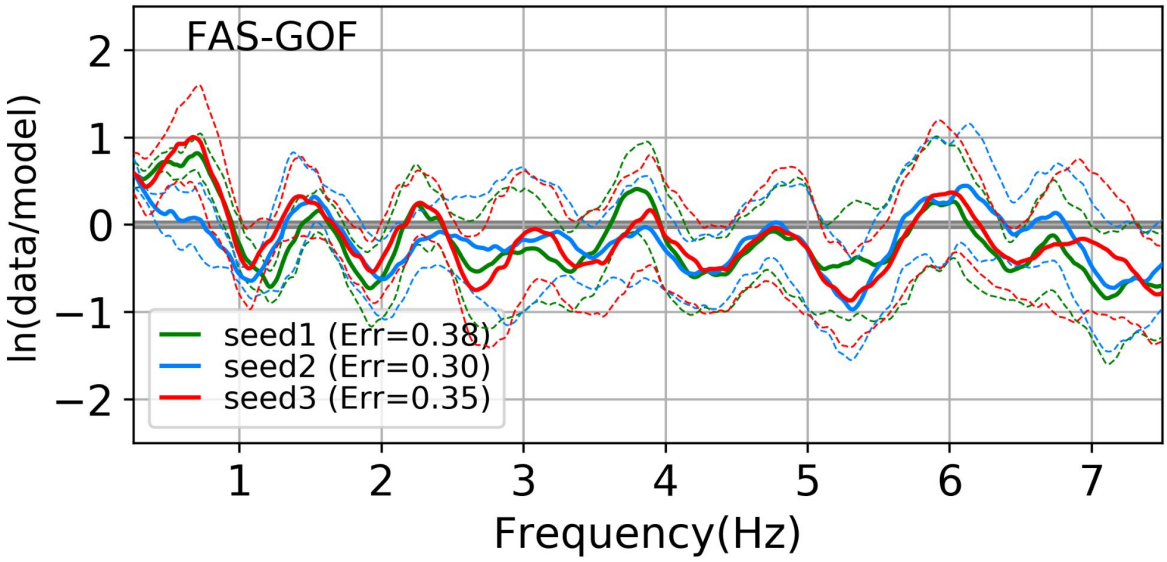

Figure 4.15: 0-7.5 Hz FAS goodness-of-fit of the simulated spectra computed with three random realizations of source models against the seismic data recorded during the 1986 M_W 6.2 earthquake. Thick lines show the mean values whereas the thin dashed lines depict the standard deviation.

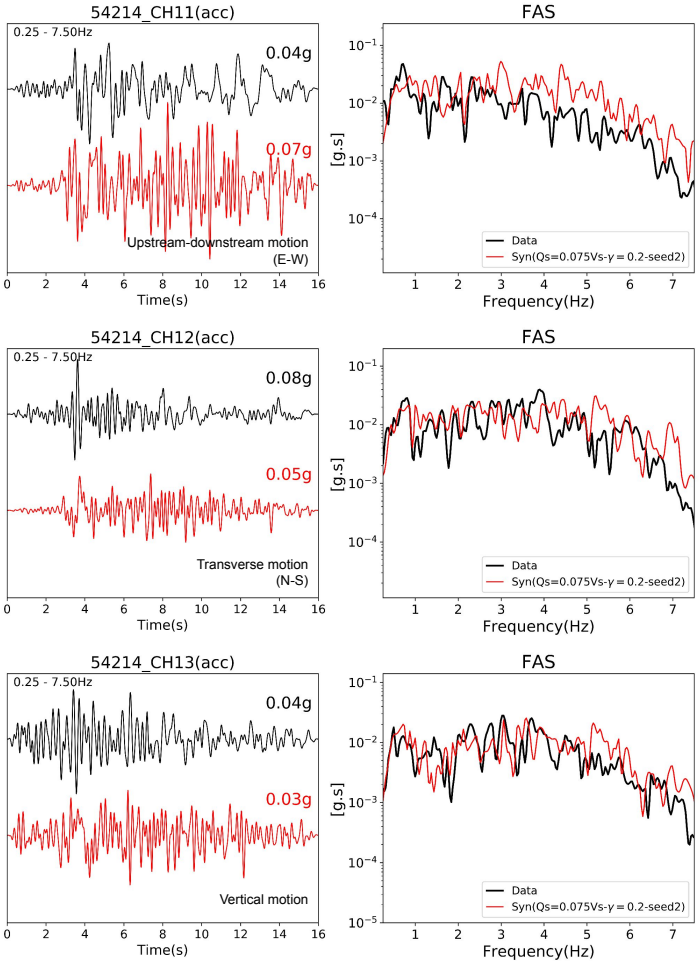

Figure 4.16: Comparison of data (black traces) and synthetics (red traces) in the time and the FAS domains at sensors located near the downstream base (See Fig. 4.1 for sensor location). The red synthetic traces were computed with CVM-S, a GTL tapered to 700 m below free surface, and a dam core with V_S=450 m/s, using the source model shown in Fig. 4.14. (See Fig. 4.1 for sensor location)

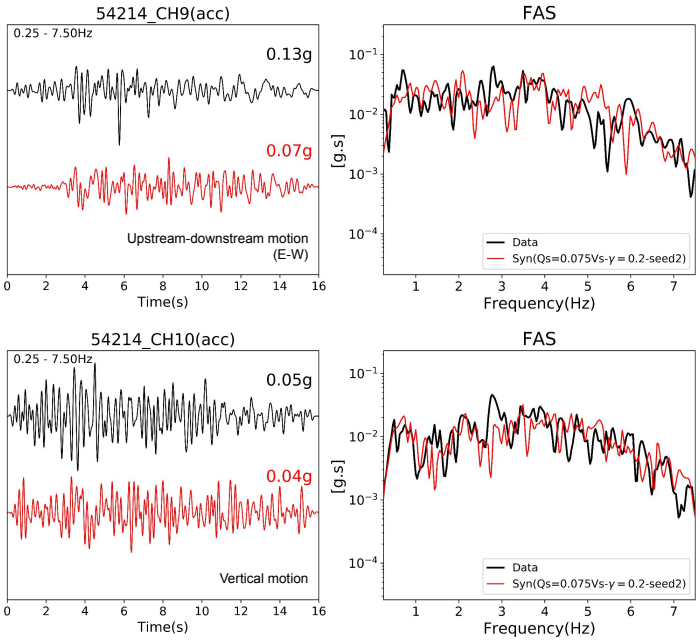

Figure 4.17: Same as Fig. 4.16, but for the sensor located in the middle of the downstream face (See Fig. 4.1 for sensor location).

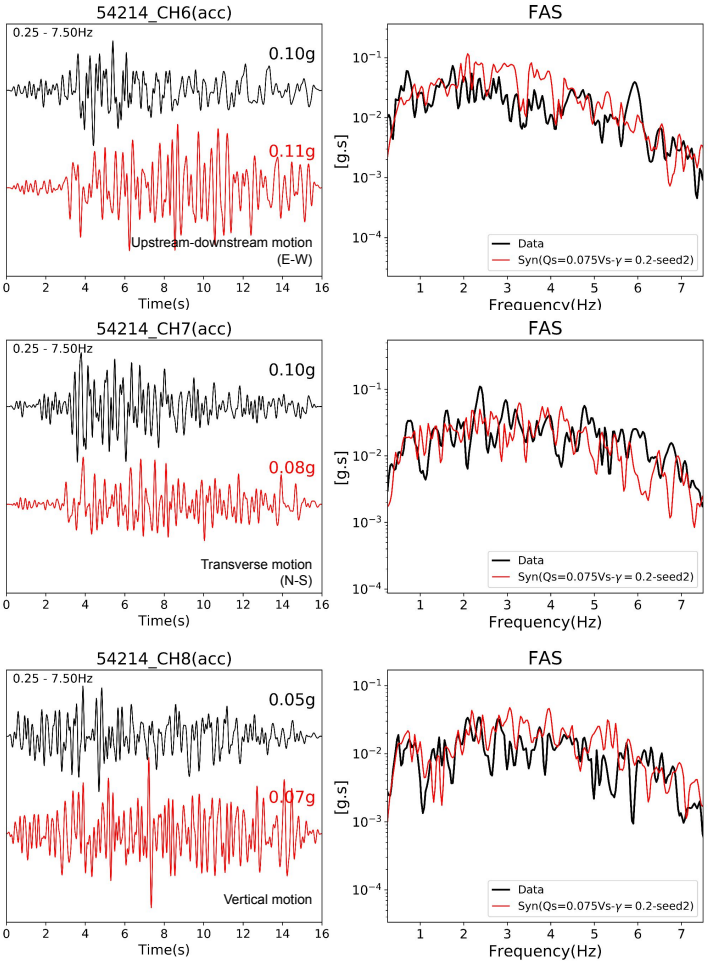

Figure 4.18: Same as Fig. 4.16, but for the sensor located at the crest center (See Fig. 4.1 for sensor location).

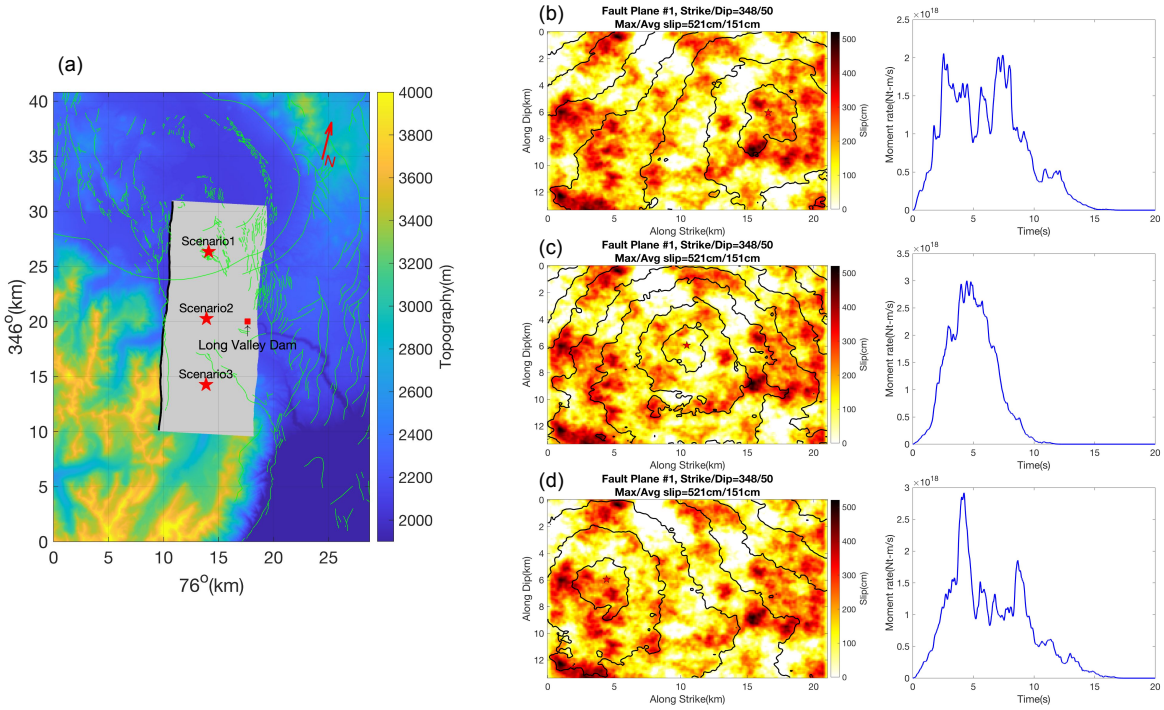

Figure 4.19: (left) Surface projection of the fault plane for the HCF scenarios, with epicentral locations for the 3 rupture scenarios (stars). (right) Slip (colors) and rupture time contours as well as moment rate histories (on the right of each slip model) for the 3 HCF scenarios with (a) southward, (b) bilateral and (c) northward rupture modes. Red stars on the slip models depict the rupture initiation locations.

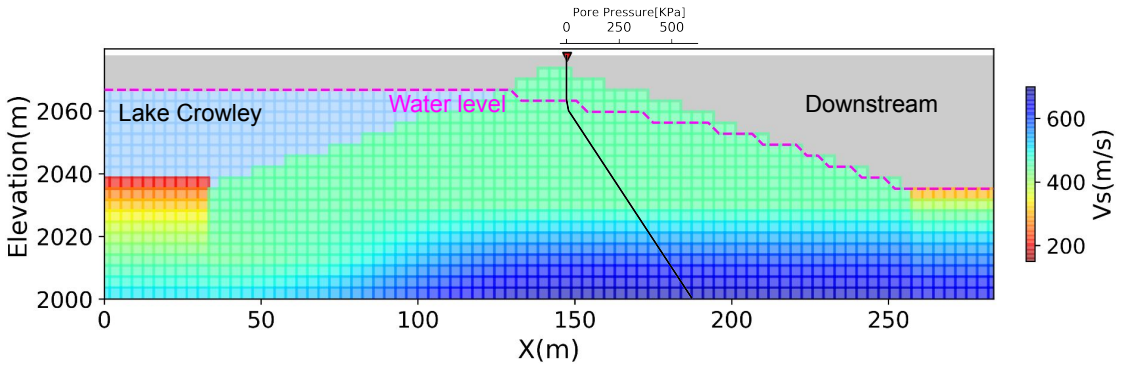

Figure 4.20: Water level assumed for the nonlinear simulations. Pore pressure as a function of depth is also shown.

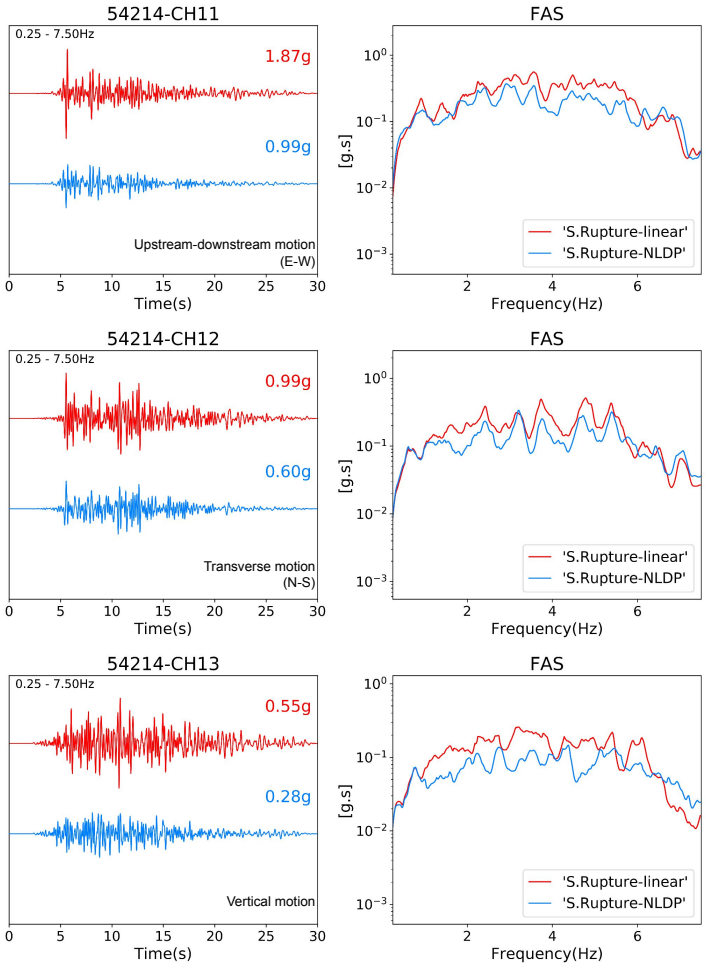

Figure 4.21: Comparison of linear (red traces) and DP-nonlinear (blue traces) synthetics computed for the southward rupture scenario in the time and FAS domains at sensors located near the downstream base (See Fig. 4.1 for sensor location).

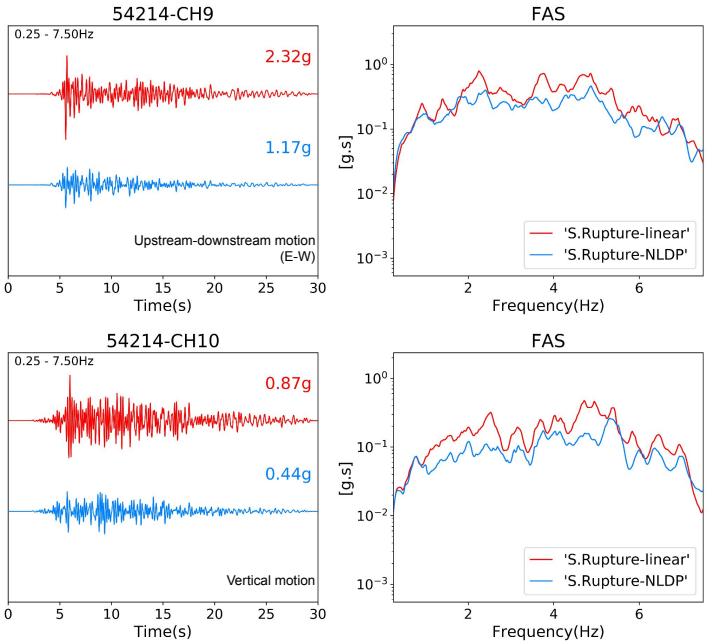

Figure 4.22: Same as Fig. 4.21, but for sensors in the middle of the downstream face (See Fig. 4.1 for sensor location).

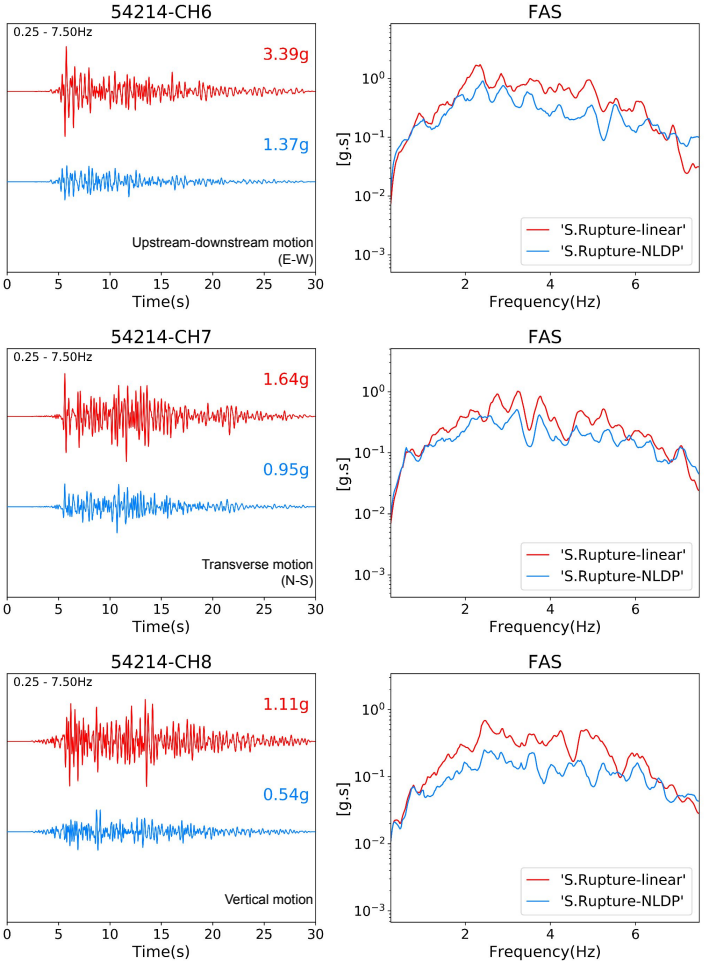

Figure 4.23: Same as Fig. 4.21, but for sensors at the crest center (See Fig. 4.1 for sensor location).

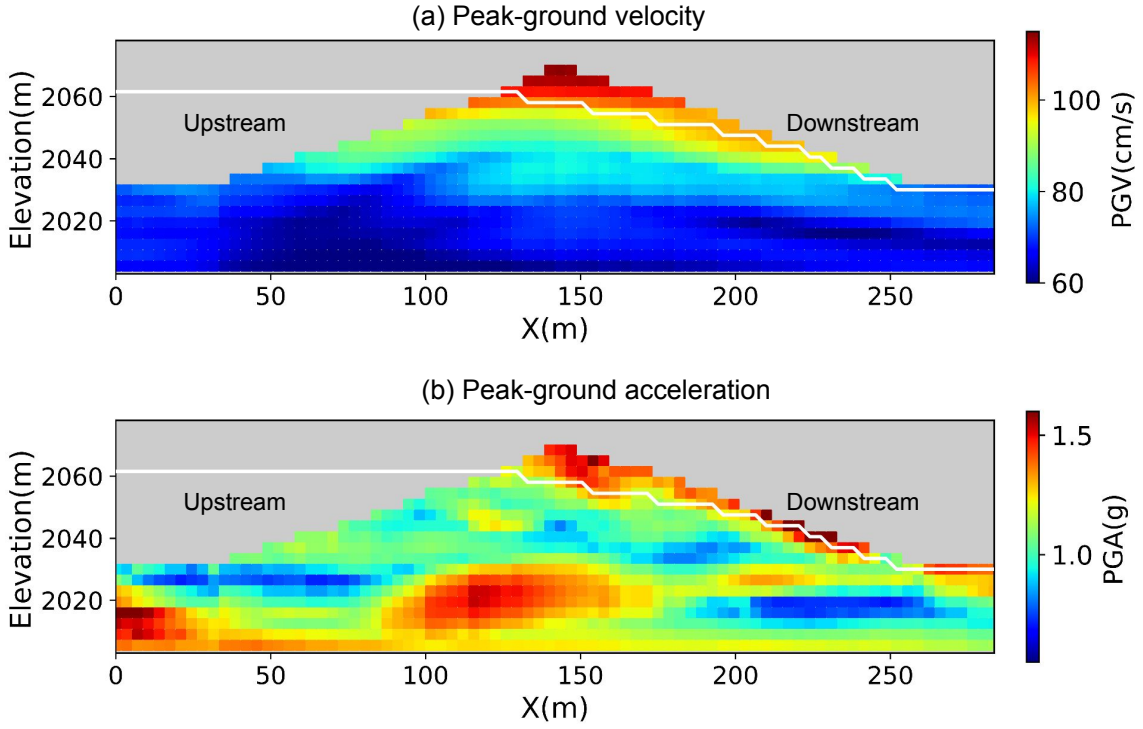

Figure 4.24: (top) PGV and (bottom PGA from HCF scenario 1 in Fig. 4.19 along the transect shown by the white line in Fig. 4.1.

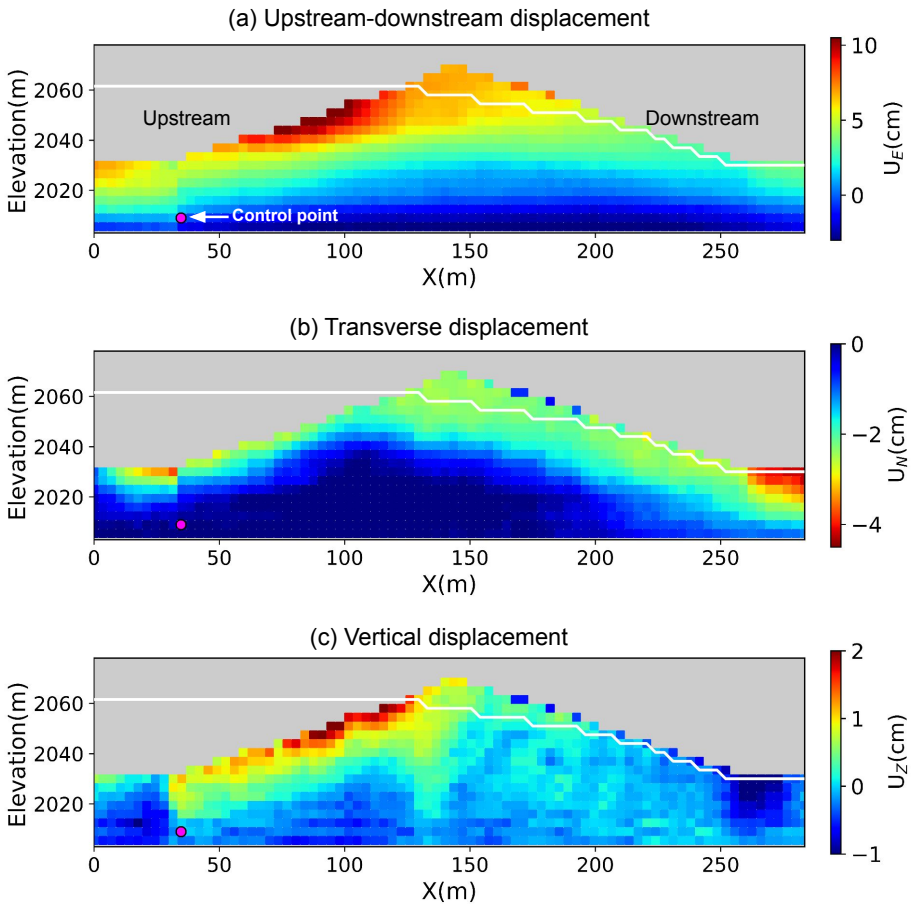

Figure 4.25: Relative displacement of the material within the LVD with respect to the control point (shown by the magenta dot) from HCF scenario 1 in Fig. 4.19.

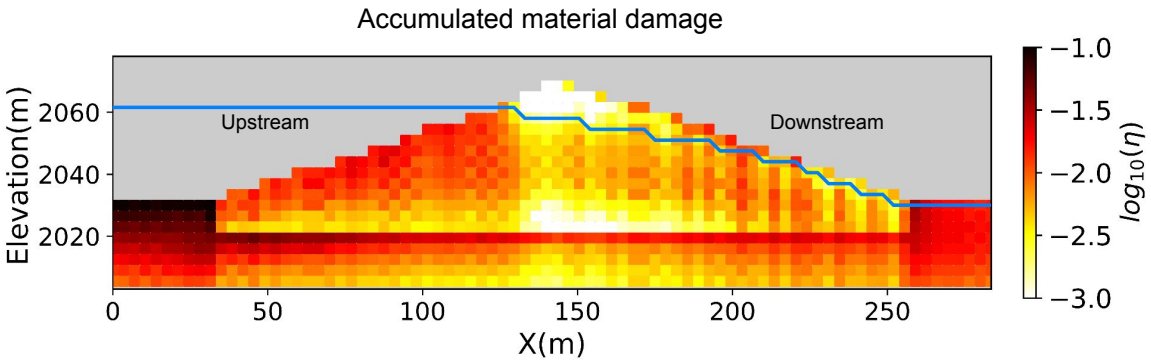

Figure 4.26: Accumulated material damage in LVD from HCF scenario 1 in Fig. 4.19 (southward rupture).

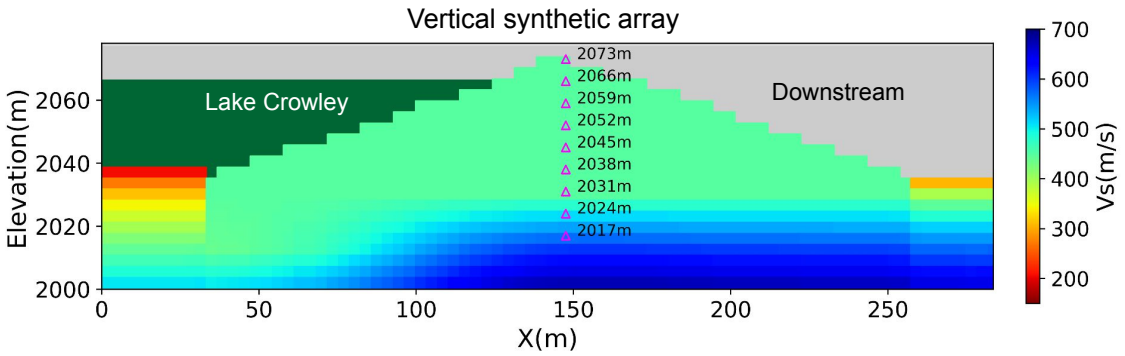

Figure 4.27: Locations of receivers in the virtual vertical array.

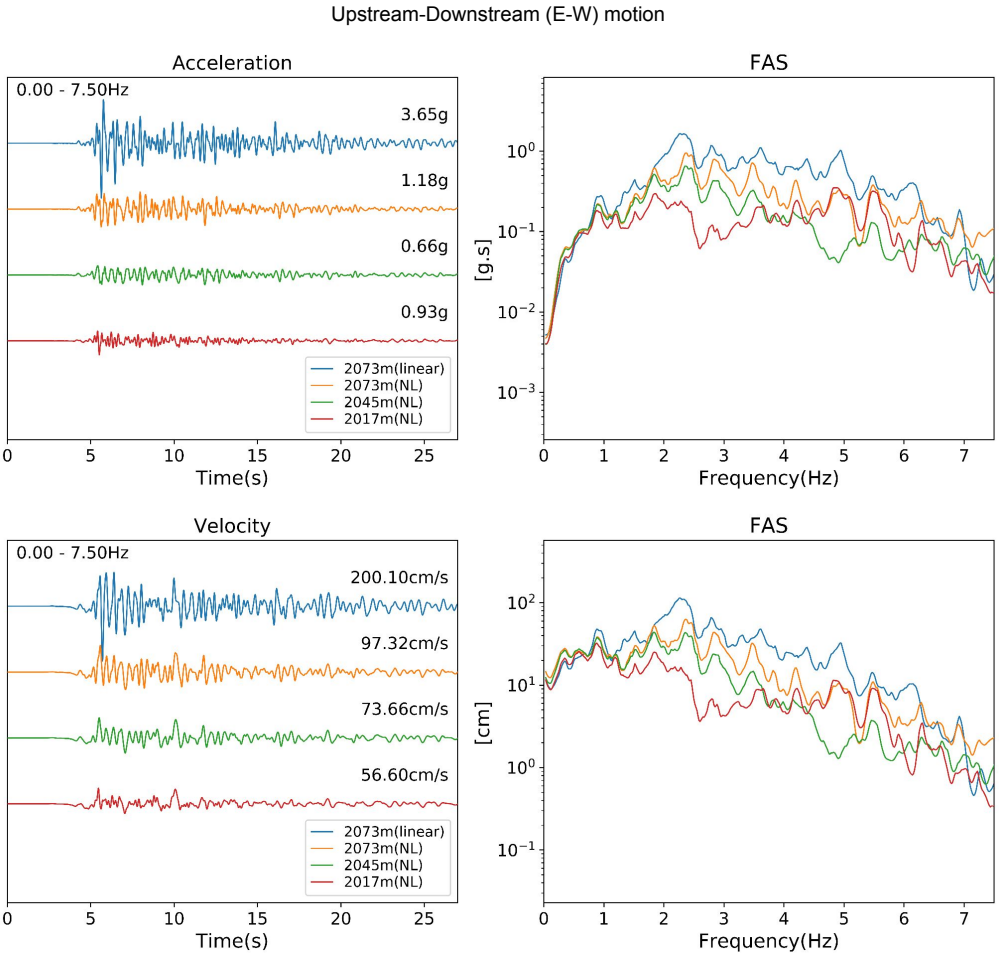

Figure 4.28: Comparison of nonlinear (top) acceleration and (bottom) velocity waveforms and spectra at stations at elevations of 2017 m (dam bottom), 2045 m, and 2073 m (dam crest surface), with the linear response at 2073 m for comparison (blue).

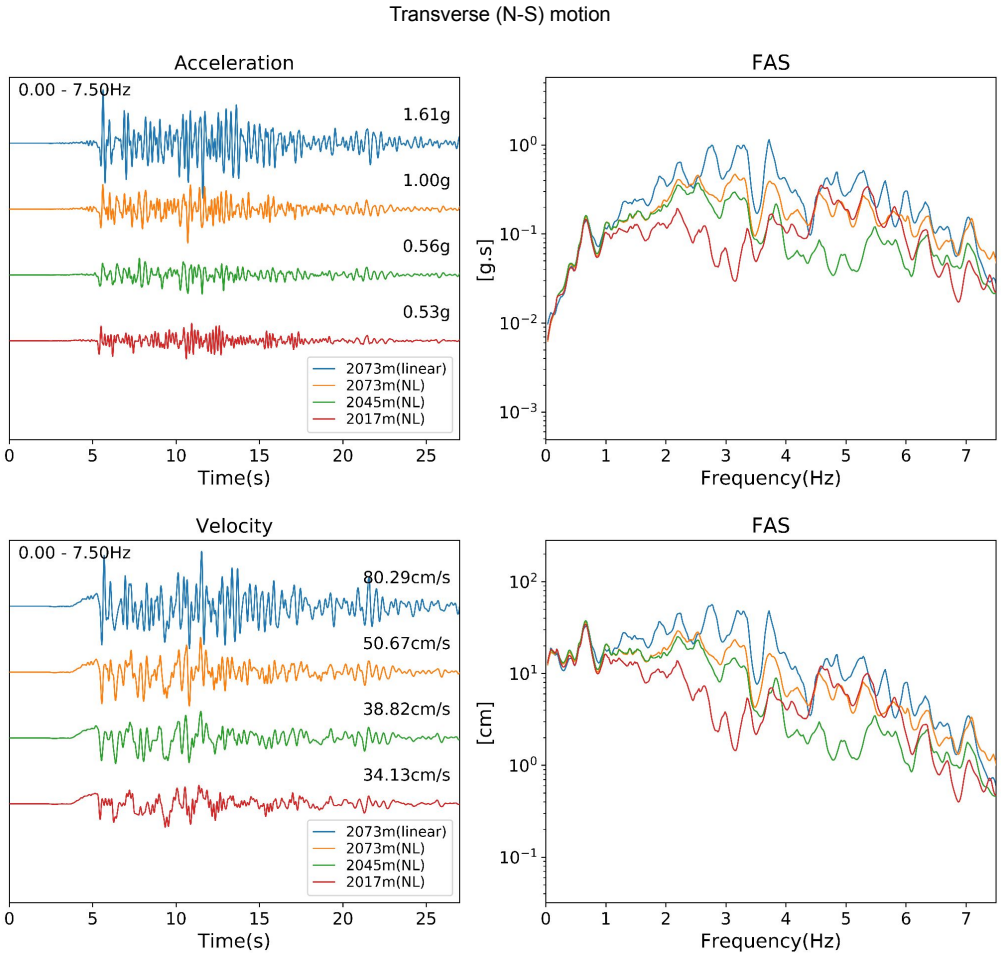

Figure 4.29: Same as Fig. 4.28, but for the transverse motion (N-S).

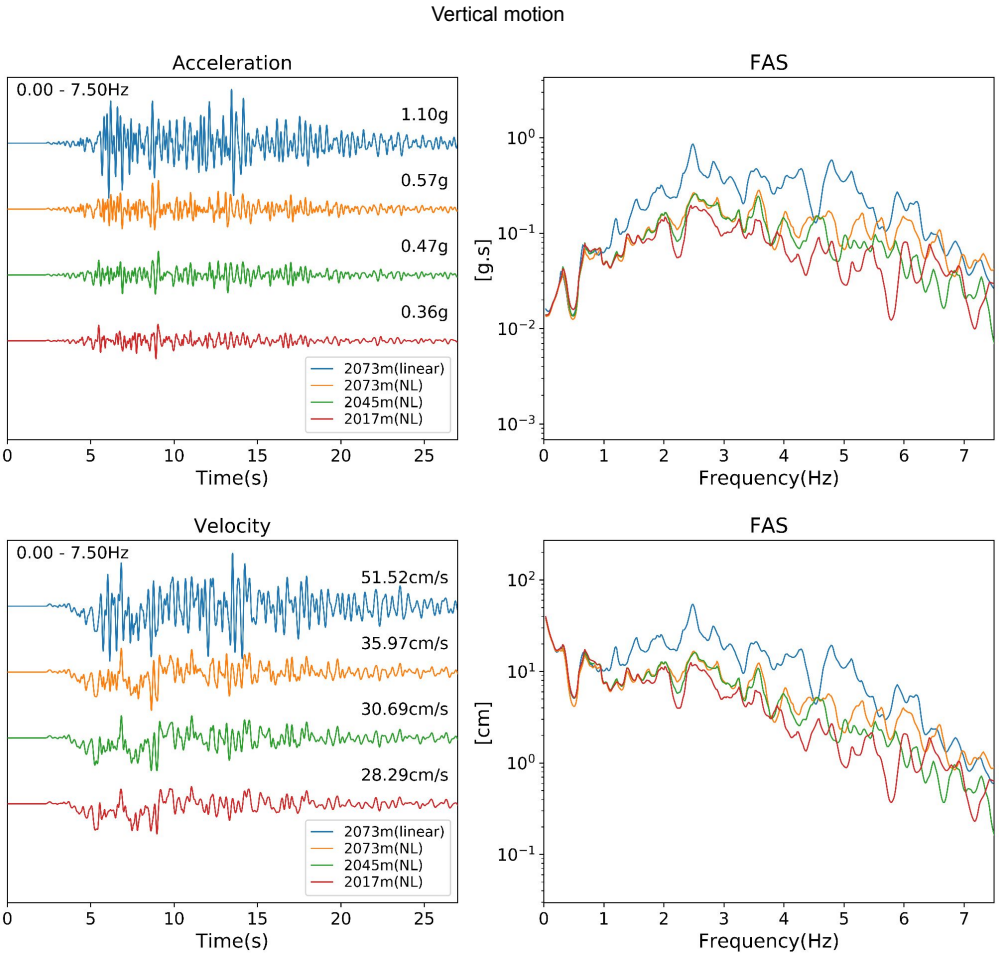

Figure 4.30: Same as Fig. 4.28, but for the vertical motion.

Appendix

4.A Appendix to Chapter 4

4.A.1 Accuracy of the vacuum formulation

We used the vacuum formulation as the free surface condition in our simulations of the Chalfant Valley and MCE scenarios for the HCF, as a version of AWP-ODC supporting both the nonlinear rheology and the surface topography using curvilinear grids was not available. The vacuum formulation treats air as an elastic material, with zero or extremely low V_S (Randall, 1989; Zahradník *et al*., 1993; Graves, 1996; Maeda *et al*., 2017). After trial-and-error simulation, we found that discretizing air with V_S=0.00001 m/s, V_P=$\sqrt{2}V_S$, and ρ=1.225 kg/m^3 and strong attenuation of Q_P=Q_S=25 produced stable results with no wave energy leaking into the air.

The geometric shape of the surface topography discretized by the vacuum formulation is described by a staircase geometry, and for this reason requires more points per wavelength as compared to other, more sophisticated free surface conditions, such as the curvilinear approach. To ensure that the resolution of our vacuum formulation is sufficient for our analysis, we compared the solution computed using the vacuum formulation against the curvilinear results in both time and frequency domains for the 2015 M_w 3.7 validation event. These tests used a Q model of Q_S/V_S=0.075, γ=0.2, $Q_P = 2Q_S$ and a GTL tapering depth of 700 m. Our analysis used stations at different locations on LVD.

To quantify the differences in the frequency domain, spectra of both solutions were smoothed over a 0.5 Hz band between 0-7.5 Hz. We then computed the percent bias of the smoothed vacuum formulation spectra, relative to that of the curvilinear solution (see Fig. 4.A.1). The spectral energy predicted by the vacuum formulation is consistently lower by $\sim$ 15%, as compared to the more accurate curvilinear approach, generally independent of frequency. Fig. 4.A.3 compares the GOF_{FAS} for these two solutions, revealing similar relative differences with respect to data.

In the time domain, we examined 0.05-7.5 Hz broadband envelopes, smoothed with a 0.2 s moving window. We find that the vacuum formulation in general can capture the overall characteristics of the curvilinear solution with 30-35 % envelope misfits (EM) (Kristeková *et al*., 2006; Kristeková *et al*., 2009) over the frequency range (Fig. 4.A.2).

In summary, our analysis suggests that the vacuum formulation used for the nonlinear modeling of the LVD with 6.7 points per minimum wavelength consistently underpredicts the spectral energy by 10-20%, with envelope misfits of 30-35%. However, these errors are much smaller than the differences with respect to data and likely less than that for the MCE source variation, justifying the use of the vacuum formulation in our analysis of the LVD.

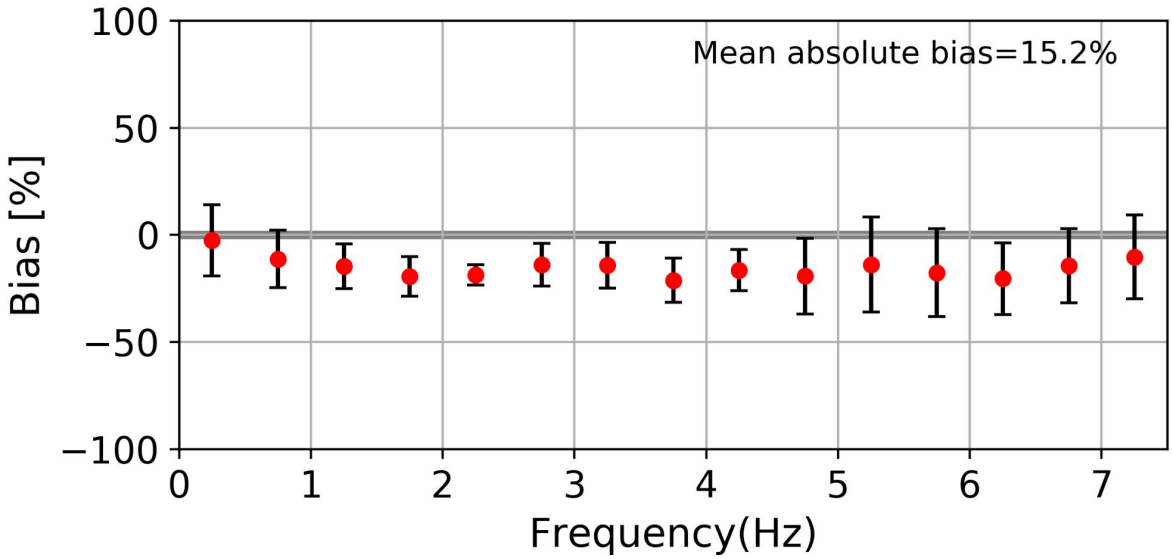

Figure 4.A.1: Bias of the FAS (smoothed over 0.5 Hz bands) of the vacuum formulation solution with respect to that of the curvilinear solution. Dots are the mean over measurements from 21 seismograms, and the error bars depict the corresponding standard deviation.

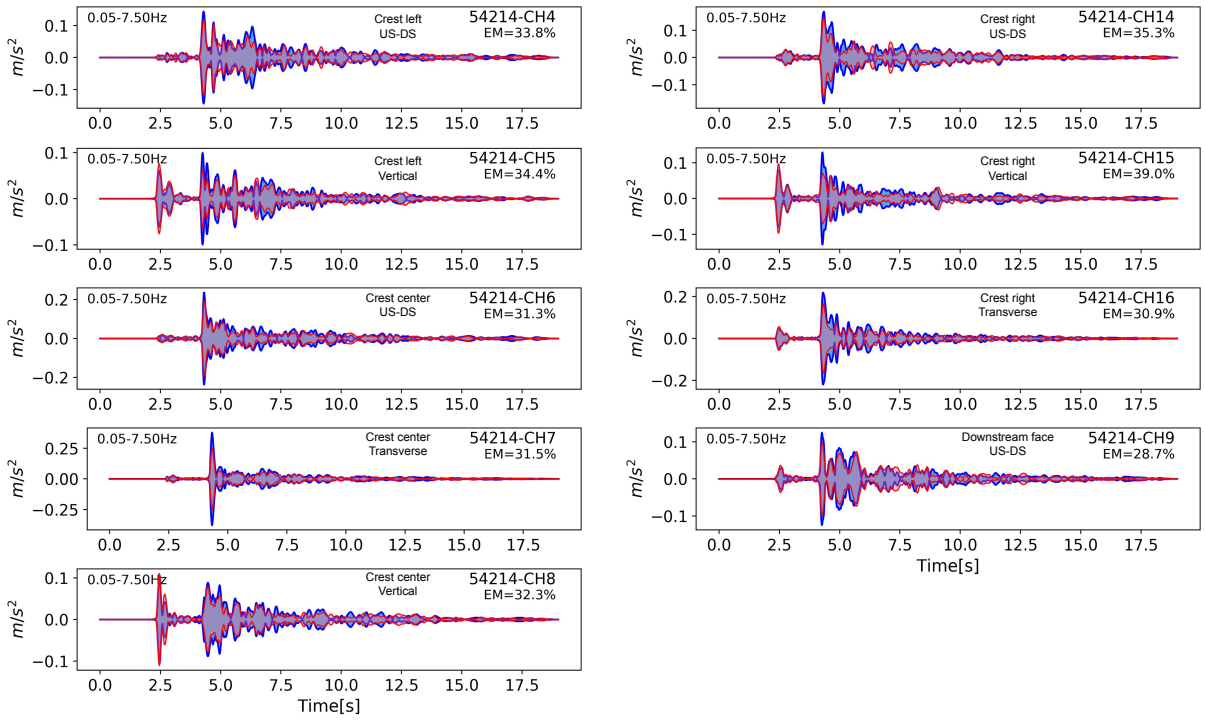

Figure 4.A.2: Smoothed (over a 0.2 s window) envelopes of the synthetics computed with the (blue) curvilinear and the (red) vacuum formulation methods.

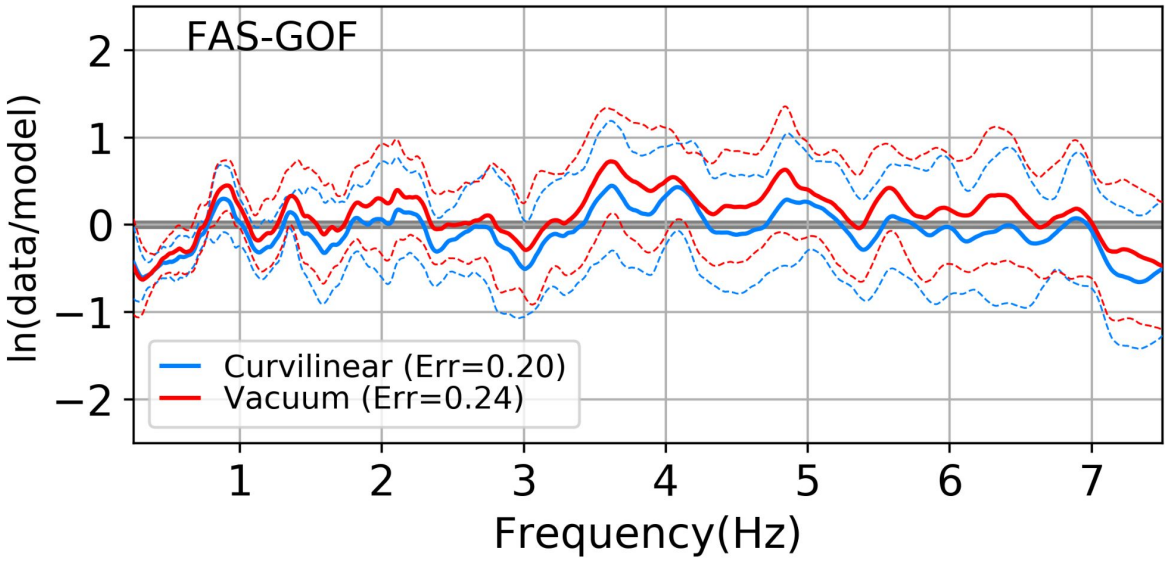

Figure 4.A.3: 0-7.5 Hz mean FAS GOF with respect to data for the vacuum formulation (red) and the curvilinear (blue) solution. Dashed lines depict one standard deviation.

4.A.2 Supplementary figures for Chapter 4

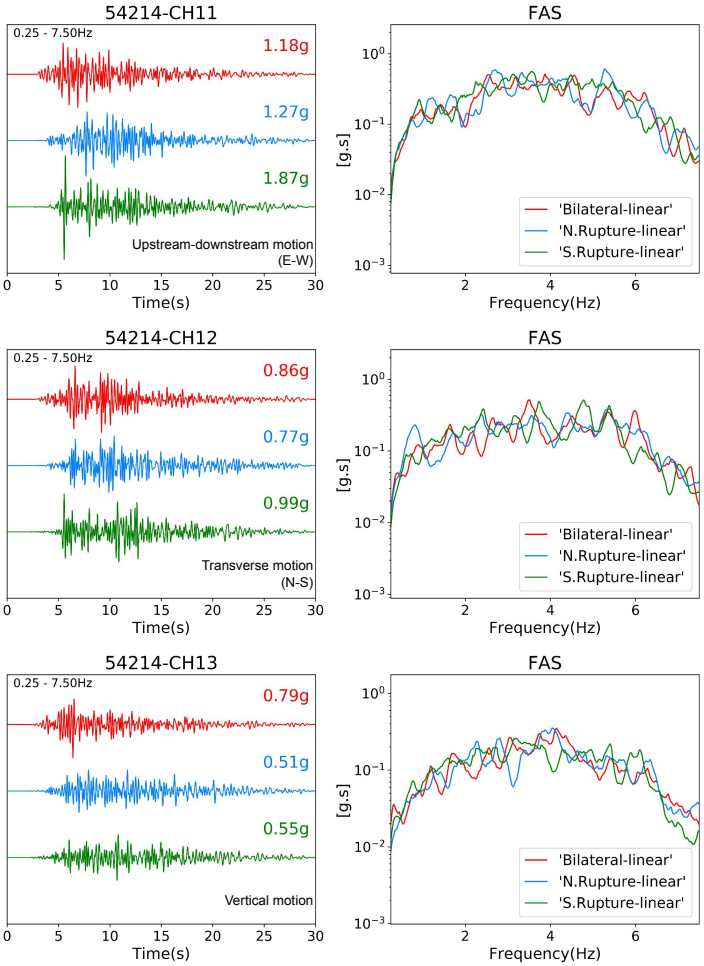

Figure 4.A.4: Comparison of synthetics for the three HCF scenarios in the time and FAS domains at sensors located near the downstream base. Synthetics were computed from purely linear simulations with (red) bilateral, (blue) northward, and (green) southward rupture modes. See Fig. 4.1 for sensor location.

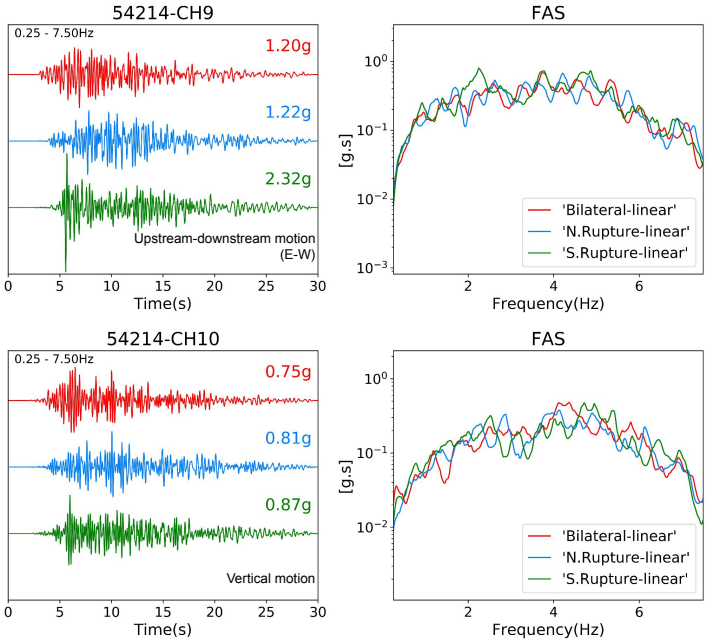

Figure 4.A.5: Same as Fig. 4.A.4, but for the sensor located in the middle of the downstream face. See Fig. 4.1 for sensor location.

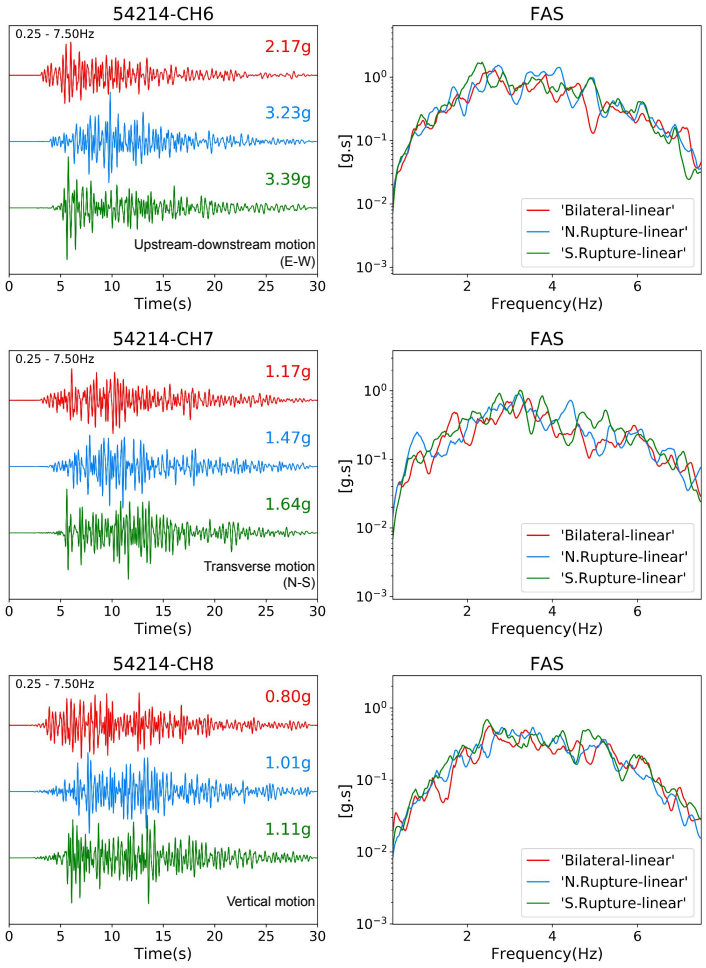

Figure 4.A.6: Same as Fig. 4.A.4, but for the sensor located at crest center. See Fig. 4.1 for sensor location.

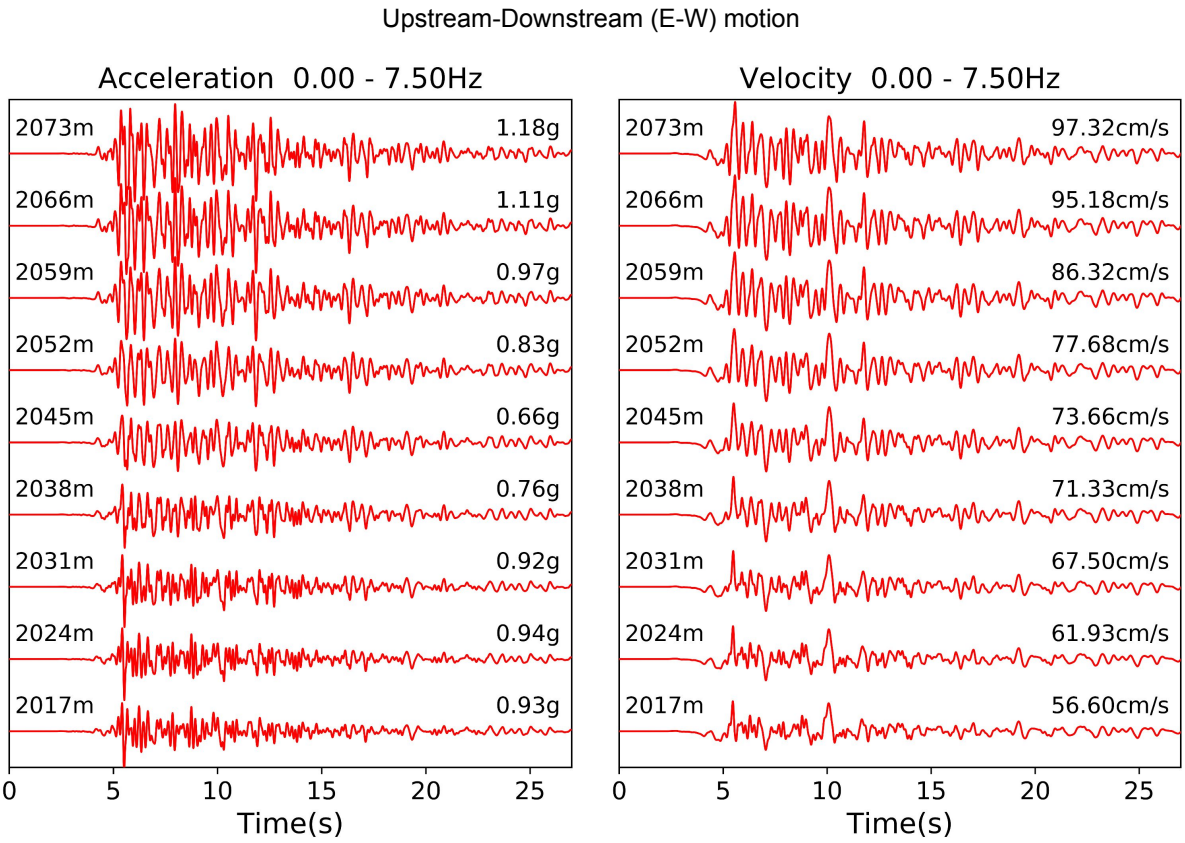

Figure 4.A.7: Synthetic (left) acceleration and (right) velocity waveforms recorded at receivers shown in Fig. 4.27. Peak motions are denoted to the right of each trace.

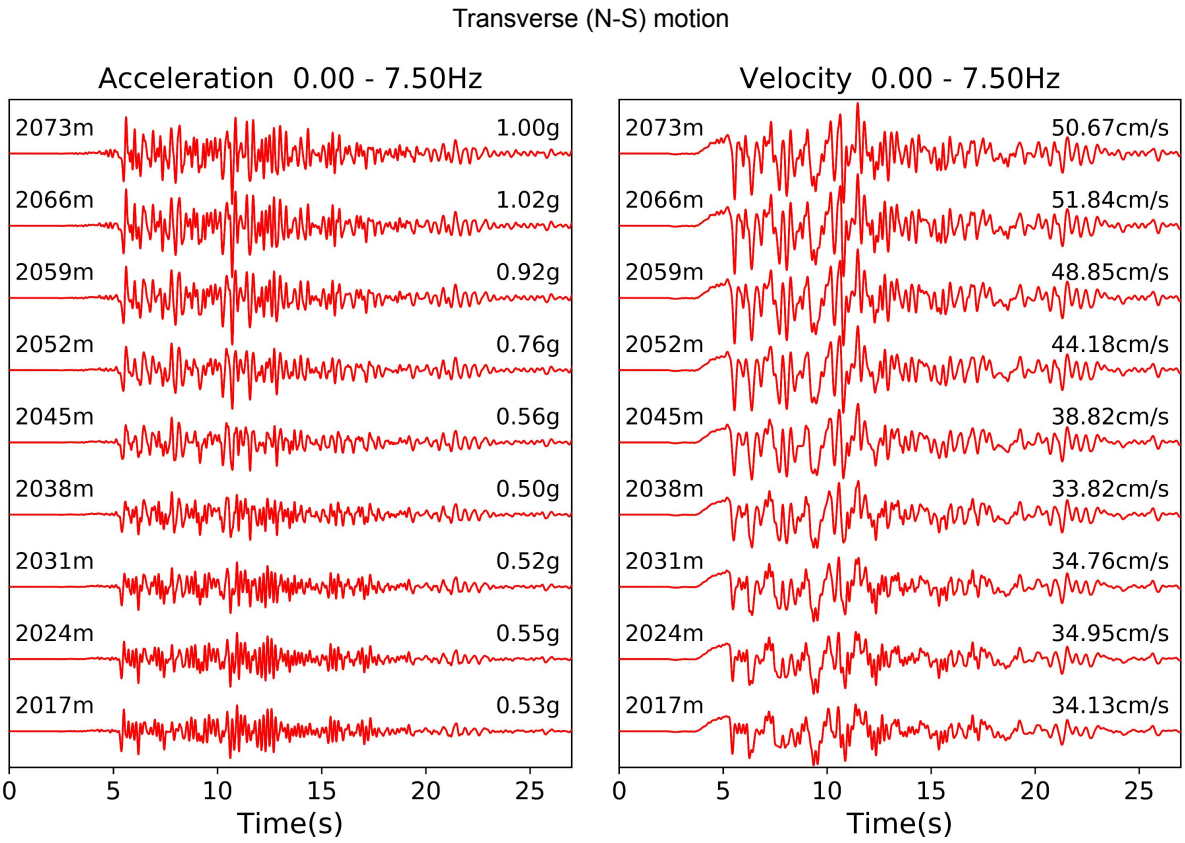

Figure 4.A.8: Same as Fig. 4.A.7, but for the transverse component (N-S).

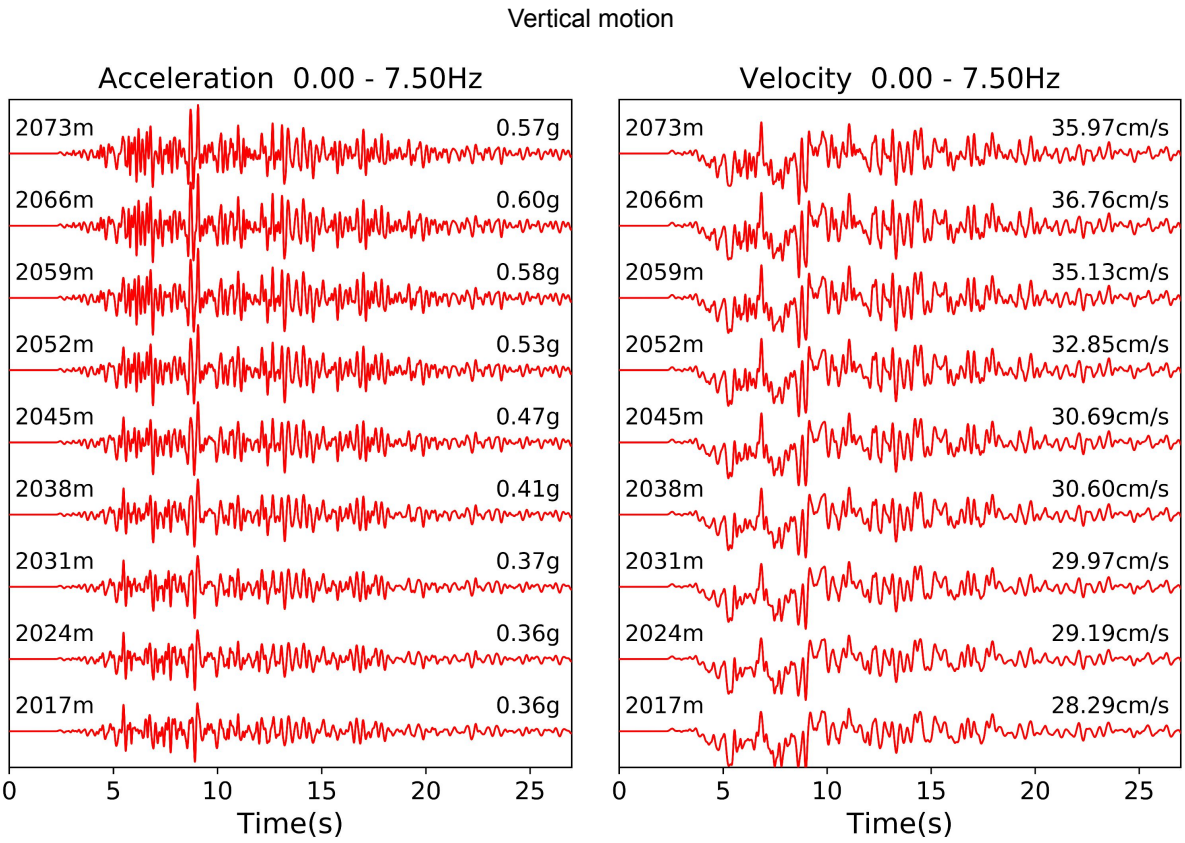

Figure 4.A.9: Same as Fig. 4.A.7, but for the vertical component.

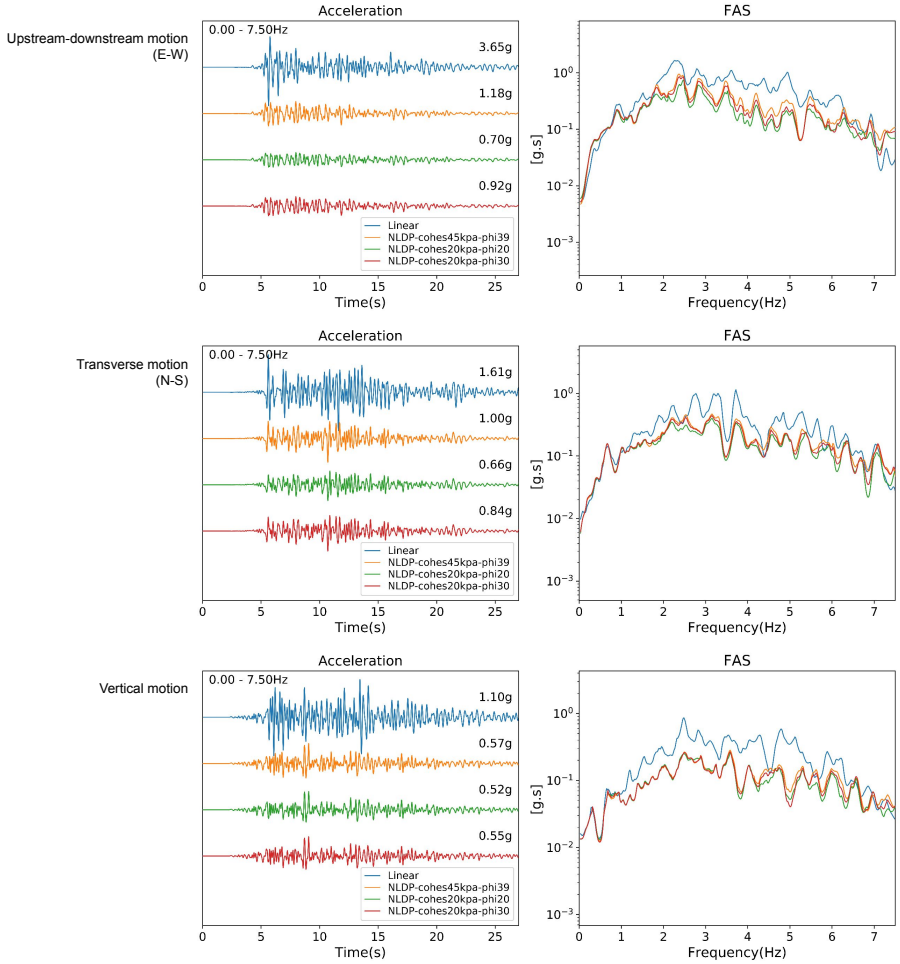

Figure 4.A.10: 0-7.5 Hz synthetic acceleration waveforms predicted for the center crest of the LVD, simulated by linear and nonlinear simulations using different combinations of cohesion and internal friction angle for the dam.

Bibliography

Ajala, R. and Persaud, P. (2021). "Effect of Merging Multiscale Models on Seismic Wavefield Predictions Near the Southern San Andreas Fault". In: *Journal of Geophysical Research: Solid Earth* 126.10, e2021JB021915. ISSN: 2169-9313.

Aki, K. (1980). "Attenuation of Shear-Waves in the Lithosphere for Frequencies from 0.05 to 25 Hz". In: *Physics of the Earth and Planetary Interiors* 21.1, pp. 50–60. ISSN: 0031-9201.

Allam, A., Ben-Zion, Y., Kurzon, I., and Vernon, F. (2014). "Seismic Velocity Structure in the Hot Springs and Trifurcation Areas of the San Jacinto Fault Zone, California, from Double-Difference Tomography". In: *Geophysical Journal International* 198.2, pp. 978–999. ISSN: 0956-540X. eprint: https://academic.oup.com/gji/article-pdf/198/2/978/1637770/ggu176.pdf.

Anderson, J. G. (2014). "The Composite Source Model for Broadband Simulations of Strong Ground Motions". In: *Seismological Research Letters* 86.1, pp. 68–74. ISSN: 0895-0695.

Andrews, D. J. (2005). "Rupture Dynamics with Energy Loss Outside the Slip Zone". In: *Journal of Geophysical Research: Solid Earth* 110.B1. ISSN: 2156-2202.

Atkinson, G. M. and Assatourians, K. (2014). "Implementation and Validation of EXSIM (A Stochastic Finite-Fault Ground-Motion Simulation Algorithm) on the SCEC Broadband Platform". In: *Seismological Research Letters* 86.1, pp. 48–60. ISSN: 0895-0695.

Bao, H., Bielak, J., Ghattas, O., Kallivokas, L. F., O'Hallaron, D. R., Shewchuk, J. R., and Xu, J. (1998). "Large-Scale Simulation of Elastic Wave Propagation in Heterogeneous Media on Parallel Computers". In: *Computer Methods in Applied Mechanics and Engineering*. Containing Papers Presented at the Symposium on Advances in Computational Mechanics 152.1, pp. 85–102. ISSN: 0045-7825.

Bard, P.-Y., Campillo, M., Chávez-Garcia, F. J., and Sánchez-Sesma, F. (1988). "The Mexico Earthquake of September 19, 1985—A Theoretical Investigation of Large- and Small-scale Amplification Effects in the Mexico City Valley". In: *Earthquake Spectra* 4.3, pp. 609–633. ISSN: 8755-2930.

Ben-Zion, Y. and Aki, K. (1990). "Seismic Radiation from an SH Line Source in a Laterally Heterogeneous Planar Fault Zone". In: *Bulletin of the Seismological Society of America* 80.4, pp. 971–994.

Ben-Zion, Y., Peng, Z., Okaya, D., Seeber, L., Armbruster, J. G., Ozer, N., Michael, A. J., Baris, S., and Aktar, M. (2003). "A Shallow Fault-Zone Structure Illuminated by Trapped Waves in the Karadere–Duzce Branch of the North Anatolian Fault, Western Turkey". In: *Geophysical Journal International* 152.3, pp. 699–717. ISSN: 0956-540X. eprint: https://academic.oup.com/gji/article-pdf/152/3/699/2032363/152-3-699.pdf.

Bianco, M. J. and Gerstoft, P. (2018). "Travel Time Tomography With Adaptive Dictionaries". In: *IEEE Transactions on Computational Imaging* 4.4, pp. 499–511. ISSN: 2333-9403.

Bianco, M. J., Gerstoft, P., Olsen, K. B., and Lin, F.-C. (2019). "High-Resolution Seismic Tomography of Long Beach, CA Using Machine Learning". In: *Sci Rep* 9.1 (1), p. 14987. ISSN: 2045-2322.

Boore, D. M. (2003). "Simulation of Ground Motion Using the Stochastic Method". In: *Pure appl. geophys.* 160.3, pp. 635–676. ISSN: 1420-9136.

Boore, D. M. and Atkinson, G. M. (2008). "Ground-Motion Prediction Equations for the Average Horizontal Component of PGA, PGV, and 5%-Damped PSA at Spectral Periods between 0.01 s and 10.0 s". In: *Earthquake Spectra* 24.1, pp. 99–138. ISSN: 8755-2930.

Boore, D. M. and Joyner, W. B. (1997). "Site Amplifications for Generic Rock Sites". In: *Bulletin of the Seismological Society of America* 87.2, pp. 327–341. ISSN: 0037-1106.

Boore, D. M., Stewart, J. P., Seyhan, E., and Atkinson, G. M. (2014). "NGA-West2 Equations for Predicting PGA, PGV, and 5% Damped PSA for Shallow Crustal Earthquakes". In: *Earthquake Spectra* 30.3, pp. 1057–1085. ISSN: 8755-2930.

Bouchon, M. and Sánchez-Sesma, F. J. (2007). "Boundary Integral Equations and Boundary Elements Methods in Elastodynamics". In: *Advances in Geophysics*. Ed. by R.-S. Wu, V. Maupin, and R. Dmowska. Vol. 48. Advances in Wave Propagation in Heterogenous Earth. Elsevier, pp. 157–189.

Breuer, A., Heinecke, A., Rettenberger, S., Bader, M., Gabriel, A.-A., and Pelties, C. (2014). "Sustained Petascale Performance of Seismic Simulations with SeisSol on SuperMUC". In: *Supercomputing*. Ed. by J. M. Kunkel, T. Ludwig, and H. W. Meuer. Lecture Notes in Computer Science. Cham: Springer International Publishing, pp. 1–18. ISBN: 978-3-319-07518-1.

Brissaud, Q., Bowden, D. C., and Tsai, V. C. (2020). "Extension of the Basin Rayleigh-Wave Amplification Theory to Include Basin-Edge Effects". In: *Bulletin of the Seismological Society of America* 110.3, pp. 1305–1322. ISSN: 0037-1106.

Brocher, T. M. (2005). "Empirical Relations between Elastic Wavespeeds and Density in the Earth's Crust". In: *Bulletin of the Seismological Society of America* 95.6, pp. 2081–2092. ISSN: 0037-1106.

Brune, J. N. (1970). "Tectonic Stress and the Spectra of Seismic Shear Waves from Earthquakes". In: *Journal of Geophysical Research (1896-1977)* 75.26, pp. 4997–5009. ISSN: 0148-0227.

Campbell, K. W. and Bozorgnia, Y. (2008). "NGA Ground Motion Model for the Geometric Mean Horizontal Component of PGA, PGV, PGD and 5% Damped Linear Elastic Response Spectra for Periods Ranging from 0.01 to 10 s". In: *Earthquake Spectra* 24.1, pp. 139–171. ISSN: 8755-2930.

Campillo, M., Bard, P.-Y., Nicollin, F., and Sánchez-Sesma, F. (1988). "The Mexico Earthquake of September 19, 1985—The Incident Wavefield in Mexico City during the Great Michoacán Earthquake and Its Interaction with the Deep Basin". In: *Earthquake Spectra* 4.3, pp. 591–608. ISSN: 8755-2930.

Campillo, M., Gariel, J. C., Aki, K., and Sánchez-Sesma, F. J. (1989). "Destructive Strong Ground Motion in Mexico City: Source, Path, and Site Effects during Great 1985 Michoacán Earthquake". In: *Bulletin of the Seismological Society of America* 79.6, pp. 1718–1735. ISSN: 0037-1106.

Catchings, R. D., Goldman, M. R., Steidl, J. H., Chan, J. H., Allam, A. A., Criley, C. J., Ma, Z., Langermann, D. S., Huddleston, G. J., McEvilly, A. T., Mongovin, D. D., Berg, E. M., and Ben-Zion, Y. (2020). "Nodal Seismograph Recordings of the 2019 Ridgecrest Earthquake Sequence". In: *Seismological Research Letters* 91.6, pp. 3622–3633. ISSN: 0895-0695.

Chen, R., Branum, D. M., Wills, C. J., and Hill, D. P. (2014). "Scenario Earthquake Hazards for the Long Valley Caldera-Mono Lake Area, East-Central California (Ver. 2.0, January 2018)". In: Open-File Report. U.S. Geological Survey.

Chiou, B.-J. and Youngs, R. R. (2008). "An NGA Model for the Average Horizontal Component of Peak Ground Motion and Response Spectra". In: *Earthquake Spectra* 24.1, pp. 173–215. ISSN: 8755-2930.

Choi, Y., Stewart, J. P., and Graves, R. W. (2005). "Empirical Model for Basin Effects Accounts for Basin Depth and Source Location". In: *Bulletin of the Seismological Society of America* 95.4, pp. 1412–1427. ISSN: 0037-1106.

Clariá, J. J. and Rinaldi, V. A. (2007). "Shear Wave Velocity of a Compacted Clayey Silt". In: *Geotechnical Testing Journal* 30.5, pp. 399–408.

Clayton, R. W., Heaton, T., Kohler, M., Chandy, M., Guy, R., and Bunn, J. (2015). "Community Seismic Network: A Dense Array to Sense Earthquake Strong Motion". In: *Seismological Research Letters* 86.5, pp. 1354–1363. ISSN: 0895-0695.

Cochran, E. S., Li, Y.-G., Shearer, P. M., Barbot, S., Fialko, Y., and Vidale, J. E. (2009). "Seismic and Geodetic Evidence for Extensive, Long-Lived Fault Damage Zones". In: *Geology* 37.4, pp. 315–318.

Cockerham, R. S. and Corbett, E. J. (1987). "The July 1986 Chalfant Valley, California, Earthquake Sequence: Preliminary Results". In: *Bulletin of the Seismological Society of America* 77.1, pp. 280–289. ISSN: 1943-3573.

Crempien, J. G. F. and Archuleta, R. J. (2014). "UCSB Method for Simulation of Broadband Ground Motion from Kinematic Earthquake Sources". In: *Seismological Research Letters* 86.1, pp. 61–67. ISSN: 0895-0695.

Cruz, C. and Miranda, E. (2017). "Evaluation of Damping Ratios for the Seismic Analysis of Tall Buildings". In: *Journal of Structural Engineering* 143.1, p. 04016144. ISSN: 1943-541X.

Cui, Y., Olsen, K. B., Jordan, T. H., Lee, K., Zhou, J., Small, P., Roten, D., Ely, G., Panda, D. K., Chourasia, A., Levesque, J., Day, S. M., and Maechling, P. (2010). "Scalable Earthquake Simulation on Petascale Supercomputers". In: SC '10: Proceedings of the 2010 ACM/IEEE International Conference for High Performance Computing, Networking, Storage and Analysis, pp. 1–20. ISBN: 2167-4337.

Cui, Y., Poyraz, E., Olsen, K. B., Zhou, J., Withers, K., Callaghan, S., Larkin, J., Guest, C., Choi, D., Chourasia, A., Shi, Z., Day, S. M., Maechling, P. J., and Jordan, T. H. (2013). "Physics-Based Seismic Hazard Analysis on Petascale Heterogeneous Supercomputers". In: SC '13: Proceedings of the International Conference on High Performance Computing, Networking, Storage and Analysis, pp. 1–12. ISBN: 2167-4337.

Day, S. M., Graves, R., Bielak, J., Dreger, D., Larsen, S., Olsen, K. B., Pitarka, A., and Ramirez-Guzman, L. (2008). "Model for Basin Effects on Long-Period Response Spectra in Southern California". In: *Earthquake Spectra* 24.1, pp. 257–277. ISSN: 8755-2930.

Dong, Y. and Lu, N. (2016). "Dependencies of Shear Wave Velocity and Shear Modulus of Soil on Saturation". In: *Journal of Engineering Mechanics* 142.11, p. 04016083. ISSN: 1943-7889.

Drucker, D. C. and Prager, W. (1952). "Soil Mechanics and Plastic Analysis or Limit Design". In: *Quarterly of applied mathematics* 10.2, pp. 157–165.

Ely, G. P., Jordan, T., Small, P., and Maechling, P. J. (2010). "A VS30-derived Nearsurface Seismic Velocity Model". In: Abstract S51A-1907, Fall Meeting. AGU San Francisco, CA.

Eshelby, J. D. (1957). "The Determination of the Elastic Field of an Ellipsoidal Inclusion, and Related Problems". In: *Proceedings of the royal society of London. Series A. Mathematical and physical sciences* 241.1226, pp. 376–396.

Fäh, D., Suhadolc, P., St. Mueller, and Panza, G. F. (1994). "A Hybrid Method for the Estimation of Ground Motion in Sedimentary Basins: Quantitative Modeling for Mexico City". In: *Bulletin of the Seismological Society of America* 84.2, pp. 383–399. ISSN: 0037-1106.

FEMA, P. (2005). *Federal Guidelines for Dam Safety: Earthquake Analyses and Design of Dams. FEMA 65*.

Fohrmann, M., Igel, H., Jahnke, G., and Ben-Zion, Y. (2004). "Guided Waves from Sources Outside Faults: An Indication for Shallow Fault Zone Structure?" In: *pure and applied geophysics* 161.11, pp. 2125–2137. ISSN: 1420-9136.

Frankel, A. (1993). "Three-Dimensional Simulations of Ground Motions in the San Bernardino Valley, California, for Hypothetical Earthquakes on the San Andreas Fault". In: *Bulletin of the Seismological Society of America* 83.4, pp. 1020–1041. ISSN: 0037-1106.

Goulet, C., Kottke, A., Boore, D., Bozorgnia, Y., Hollenback, J., Kishida, T., Der Kiureghian, A., Ktenidou, O., Kuehn, N., Rathje, E., *et al*. (2018). "Effective Amplitude Spectrum (EAS) as a Metric for Ground Motion Modeling Using Fourier Amplitudes". In: *2018 Seismology of the Americas Meeting*.

Graves, R. and Pitarka, A. (2014). "Refinements to the Graves and Pitarka (2010) Broadband Ground-Motion Simulation Method". In: *Seismological Research Letters* 86.1, pp. 75–80. ISSN: 0895-0695.

— (2016). "Kinematic Ground-Motion Simulations on Rough Faults Including Effects of 3D Stochastic Velocity Perturbations". In: *Bulletin of the Seismological Society of America* 106.5, pp. 2136–2153. ISSN: 0037-1106.

Graves, R. W. (1996). "Simulating Seismic Wave Propagation in 3D Elastic Media Using Staggered-Grid Finite Differences". In: *Bulletin of the Seismological Society of America* 86.4, pp. 1091–1106. ISSN: 0037-1106.

Graves, R. W., Aagaard, B. T., and Hudnut, K. W. (2011). "The ShakeOut Earthquake Source and Ground Motion Simulations". In: *Earthquake Spectra* 27.2, pp. 273–291.

Graves, R. W., Aagaard, B. T., Hudnut, K. W., Star, L. M., Stewart, J. P., and Jordan, T. H. (2008). "Broadband Simulations for Mw 7.8 Southern San Andreas Earthquakes: Ground Motion Sensitivity to Rupture Speed". In: *Geophysical Research Letters* 35.22. ISSN: 0094-8276.

Griffiths, D. V. and Prevost, J. H. (1988). "Two- and Three-Dimensional Dynamic Finite Element Analyses of the Long Valley Dam". In: *Géotechnique* 38.3, pp. 367–388.

Haller, K. M., Machette, M. N., Dart, R. L., and Rhea, B. S. (2004). *US Quaternary Fault and Fold Database Released*.

Harris, R. A., Barall, M., Andrews, D. J., Duan, B., Ma, S., Dunham, E. M., Gabriel, A.-A., Kaneko, Y., Kase, Y., Aagaard, B. T., Oglesby, D. D., Ampuero, J.-P., Hanks, T. C., and Abrahamson, N. (2011). "Verifying a Computational Method for Predicting Extreme Ground Motion". In: *Seismological Research Letters* 82.5, pp. 638–644. ISSN: 0895-0695.

Hill, D. P. and Montgomery-Brown, E. (2015). "Long Valley Caldera and the UCERF Depiction of Sierra Nevada Range-Front Faults". In: *Bulletin of the Seismological Society of America* 105.6, pp. 3189–3195. ISSN: 0037-1106.

Hoek, E., Carranza-Torres, C., and Corkum, B. (2002). "Hoek-Brown Failure Criterion-2002 Edition". In: *Proceedings of NARMS-Tac* 1.1, pp. 267–273.

Hu, Z., Olsen, K. B., and Day, S. M. (2022a). "0–5 Hz Deterministic 3-D Ground Motion Simulations for the 2014 La Habra, California, Earthquake". In: *Geophysical Journal International* 230.3, pp. 2162–2182. ISSN: 0956-540X.

— (2022b). "Calibration of the Near-Surface Seismic Structure in the SCEC Community Velocity Model Version 4". In: *Geophysical Journal International* 230.3, pp. 2183–2198. ISSN: 0956-540X.

Igel, H., Jahnke, G., and Ben-Zion, Y. (2002). "Numerical Simulation of Fault Zone Guided Waves: Accuracy and 3-D Effects". In: *Earthquake Processes: Physical Modelling, Numerical Simulation and Data Analysis Part I*. Ed. by M. Matsu'ura, P. Mora, A. Donnellan, and X.-c. Yin. Basel: Birkhäuser Basel, pp. 2067–2083. ISBN: 978-3-0348-8203-3.

Kawase, H. (1996). "The Cause of the Damage Belt in Kobe: "The Basin-Edge Effect," Constructive Interference of the Direct S-Wave with the Basin-Induced Diffracted/Rayleigh Waves". In: *Seismological Research Letters* 67.5, pp. 25–34. ISSN: 0895-0695.

Kohler, M. D., Filippitzis, F., Heaton, T., Clayton, R. W., Guy, R., Bunn, J., and Chandy, K. M. (2020). "2019 Ridgecrest Earthquake Reveals Areas of Los Angeles That Amplify Shaking of High-Rises". In: *Seismological Research Letters* 91.6, pp. 3370–3380. ISSN: 0895-0695.

Komatitsch, D. and Vilotte, J.-P. (1998). "The Spectral Element Method: An Efficient Tool to Simulate the Seismic Response of 2D and 3D Geological Structures". In: *Bulletin of the Seismological Society of America* 88.2, pp. 368–392. ISSN: 0037-1106.

Kottke, A. R., Abrahamson, N. A., Boore, D. M., Bozorgnia, Y., Goulet, C. A., Hollenback, J., Kishida, T., Ktenidou, O.-J., Rathje, E. M., Silva, W. J., Thompson, E. M., and Wang, X. (2021). "Selection of Random Vibration Theory Procedures for the NGA-East Project and Ground-Motion Modeling". In: *Earthquake Spectra* 37 (1_suppl), pp. 1420–1439. ISSN: 8755-2930.

Kristeková, M., Kristek, J., and Moczo, P. (2009). "Time-Frequency Misfit and Goodness-of-Fit Criteria for Quantitative Comparison of Time Signals". In: *Geophysical Journal International* 178.2, pp. 813–825. ISSN: 0956-540X.

Kristeková, M., Kristek, J., Moczo, P., and Day, S. M. (2006). "Misfit Criteria for Quantitative Comparison of Seismograms". In: *Bulletin of the Seismological Society of America* 96.5, pp. 1836–1850. ISSN: 0037-1106.

Lai, S. and Seed, H. B. (1985). *Dynamic Response of Long Valley Dam in the Mammoth Lake Earthquake Series of May 25-27, 1980*. 142304. College of Engineering, University of California.

Lee, E.-J., Chen, P., Jordan, T. H., Maechling, P. B., Denolle, M. A. M., and Beroza, G. C. (2014). "Full-3-D Tomography for Crustal Structure in Southern California Based on the Scattering-Integral and the Adjoint-Wavefield Methods". In: *Journal of Geophysical Research: Solid Earth* 119.8, pp. 6421–6451. ISSN: 2169-9313.

Lee, S.-J., Komatitsch, D., Huang, B.-S., and Tromp, J. (2009). "Effects of Topography on Seismic-Wave Propagation: An Example from Northern TaiwanEffects of Topography on Seismic-Wave Propagation: An Example from Northern Taiwan". In: *Bulletin of the Seismological Society of America* 99.1, pp. 314–325. ISSN: 0037-1106.

Leonard, M. (2010). "Earthquake Fault Scaling: Self-Consistent Relating of Rupture Length, Width, Average Displacement, and Moment Release". In: *Bulletin of the Seismological Society of America* 100 (5A), pp. 1971–1988. ISSN: 0037-1106.

— (2014). "Self-Consistent Earthquake Fault-Scaling Relations: Update and Extension to Stable Continental Strike-Slip Faults". In: *Bulletin of the Seismological Society of America* 104.6, pp. 2953–2965. ISSN: 0037-1106.

Lewis, M. A., Peng, Z., Ben-Zion, Y., and Vernon, F. L. (2005). "Shallow Seismic Trapping Structure in the San Jacinto Fault Zone near Anza, California". In: *Geophysical Journal International* 162.3, pp. 867–881. ISSN: 0956-540X. eprint: https://academic.oup.com/gji/article-pdf/162/3/867/6042388/162-3-867.pdf.

Li, Y.-G. and Leary, P. C. (1990). "Fault Zone Trapped Seismic Waves". In: *Bulletin of the Seismological Society of America* 80.5, pp. 1245–1271. ISSN: 0037-1106. eprint: https://pubs.geoscienceworld.org/ssa/bssa/article-pdf/80/5/1245/5339761/bssa0800051245.pdf.

Li, Y.-G., Vidale, J. E., and Cochran, E. S. (2004). "Low-Velocity Damaged Structure of the San Andreas Fault at Parkfield from Fault Zone Trapped Waves". In: *Geophysical Research Letters* 31.12.

Lin, Y.-P. and Jordan, T. H. (2018). "Frequency-Dependent Attenuation of P and S Waves in Southern California". In: *Journal of Geophysical Research: Solid Earth* 123.7, pp. 5814–5830. ISSN: 2169-9313.

Liu, C., Lay, T., Brodsky, E. E., Dascher-Cousineau, K., and Xiong, X. (2019). "Coseismic Rupture Process of the Large 2019 Ridgecrest Earthquakes From Joint Inversion of Geodetic and Seismological Observations". In: *Geophysical Research Letters* 46.21, pp. 11820–11829. ISSN: 0094-8276 1944-8007.

Ma, K.-F., Song, T.-R. A., Lee, S.-J., and Wu, H. I. (2000). "Spatial Slip Distribution of the September 20, 1999, Chi-Chi, Taiwan, Earthquake (MW7.6) -Inverted from Teleseismic Data". In: *Geophysical Research Letters* 27.20, pp. 3417–3420. ISSN: 00948276.

Madariaga, R. (1976). "Dynamics of an Expanding Circular Fault". In: *Bulletin of the Seismological Society of America* 66.3, pp. 639–666.

Maechling, P. J., Silva, F., Callaghan, S., and Jordan, T. H. (2014). "SCEC Broadband Platform: System Architecture and Software Implementation". In: *Seismological Research Letters* 86.1, pp. 27–38. ISSN: 0895-0695.

Maeda, T. and Furumura, T. (2013). "FDM Simulation of Seismic Waves, Ocean Acoustic Waves, and Tsunamis Based on Tsunami-Coupled Equations of Motion". In: *Pure and Applied Geophysics* 170.1, pp. 109–127. ISSN: 1420-9136.

Maeda, T., Takemura, S., and Furumura, T. (2017). "OpenSWPC: An Open-Source Integrated Parallel Simulation Code for Modeling Seismic Wave Propagation in 3D Heterogeneous Viscoelastic Media". In: *Earth, Planets and Space* 69.1, p. 102. ISSN: 1880-5981.

Magistrale, H., Day, S., Clayton, R. W., and Graves, R. (2000). "The SCEC Southern California Reference Three-Dimensional Seismic Velocity Model Version 2". In: *Bulletin of the Seismological Society of America* 90 (6B), S65–S76. ISSN: 0037-1106.

Manolis, G. D. and Beskos, D. E. (1988). *Boundary Element Methods in Elastodynamics*. Taylor & Francis.

Muir, J. B., Clayton, R. W., Tsai, V. C., and Brissaud, Q. (2022). "Parsimonious Velocity Inversion Applied to the Los Angeles Basin, CA". In: *Journal of Geophysical Research: Solid Earth* 127.2. e2021JB023103 2021JB023103, e2021JB023103. ISSN: 2169-9356.

Nie, S., Wang, Y., Olsen, K. B., and Day, S. M. (2017). "Fourth-Order Staggered-Grid Finite-Difference Seismic Wavefield Estimation Using a Discontinuous Mesh Interface (WEDMI)Fourth-Order Staggered-Grid Finite-Difference Seismic WEDMI". In: *Bulletin of the Seismological Society of America* 107.5, pp. 2183–2193. ISSN: 0037-1106.

O'Reilly, O., Yeh, T.-Y., Olsen, K. B., Hu, Z., Breuer, A., Roten, D., and Goulet, C. A. (2021). "A High-Order Finite-Difference Method on Staggered Curvilinear Grids for Seismic Wave Propagation Applications with Topography". In: *Bulletin of the Seismological Society of America*. ISSN: 0037-1106.

Olsen, K. B. (2000). "Site Amplification in the Los Angeles Basin from Three-Dimensional Modeling of Ground Motion". In: *Bulletin of the Seismological Society of America* 90 (6B), S77–S94. ISSN: 0037-1106.

Olsen, K. B., Day, S. M., and Bradley, C. R. (2003). "Estimation of Q for Long-Period (>2 Sec) Waves in the Los Angeles Basin". In: *Bulletin of the Seismological Society of America* 93.2, pp. 627–638. ISSN: 0037-1106.

Olsen, K. B., Day, S. M., Dalguer, L. A., Mayhew, J., Cui, Y., Zhu, J., Cruz-Atienza, V. M., Roten, D., Maechling, P., Jordan, T. H., Okaya, D., and Chourasia, A. (2009). "ShakeOut-D: Ground Motion Estimates Using an Ensemble of Large Earthquakes on the Southern San Andreas Fault with Spontaneous Rupture Propagation". In: *Geophysical Research Letters* 36.4. ISSN: 0094-8276.

Olsen, K. B., Day, S. M., Minster, J. B., Cui, Y., Chourasia, A., Faerman, M., Moore, R., Maechling, P., and Jordan, T. (2006). "Strong Shaking in Los Angeles Expected from Southern San Andreas Earthquake". In: *Geophysical Research Letters* 33.7. ISSN: 0094-8276.

Olsen, K. B., Day, S. M., Minster, J. B., Cui, Y., Chourasia, A., Okaya, D., Maechling, P., and Jordan, T. (2008). "TeraShake2: Spontaneous Rupture Simulations of Mw 7.7 Earthquakes on the Southern San Andreas Fault". In: *Bulletin of the Seismological Society of America* 98.3, pp. 1162–1185. ISSN: 0037-1106.

Olsen, K. and Takedatsu, R. (2014). "The SDSU Broadband Ground-Motion Generation Module BBtoolbox Version 1.5". In: *Seismological Research Letters* 86.1, pp. 81–88. ISSN: 0895-0695.

Olsen, K. B., Pechmann, J. C., and Schuster, G. T. (1995). "Simulation of 3D Elastic Wave Propagation in the Salt Lake Basin". In: *Bulletin of the Seismological Society of America* 85.6, pp. 1688–1710. ISSN: 1943-3573.

Olsen, K. B. and Mayhew, J. E. (2010). "Goodness-of-Fit Criteria for Broadband Synthetic Seismograms, with Application to the 2008 Mw 5.4 Chino Hills, California, Earthquake". In: *Seismological Research Letters* 81.5, pp. 715–723. ISSN: 0895-0695.

Olsen, K. B. (1994). "Simulation of Three-Dimensional Wave Propagation in the Salt Lake Basin". In: *Ph.D. Thesis* University of Utah, Salt Lake City, Utah, 157 p.

Pacheco, J. and Nábělek, J. (1988). "Source Mechanisms of Three Moderate California Earthquakes of July 1986". In: *Bulletin of the Seismological Society of America* 78.6, pp. 1907–1929. ISSN: 0037-1106.

Peng, Z. and Ben-Zion, Y. (2006). "Temporal Changes of Shallow Seismic Velocity around the Karadere-Düzce Branch of the North Anatolian Fault and Strong Ground Motion". In: *Pure and Applied Geophysics* 163.2, pp. 567–600.

Phillips, W. S., Mayeda, K. M., and Malagnini, L. (2014). "How to Invert Multi-Band, Regional Phase Amplitudes for 2-D Attenuation and Source Parameters: Tests Using the USArray". In: *Pure and Applied Geophysics* 171.3, pp. 469–484. ISSN: 1420-9136.

Phung, V.-B., Loh, C. H., Chao, S. H., Chiou, B. S., and Huang, B.-S. (2020). "Ground Motion Prediction Equation for Crustal Earthquakes in Taiwan". In: *Earthquake Spectra* 36.4, pp. 2129–2164. ISSN: 8755-2930.

Pitarka, A., Graves, R., Irikura, K., Miyakoshi, K., Wu, C., Kawase, H., Rodgers, A., and McCallen, D. (2021). "Refinements to the Graves–Pitarka Kinematic Rupture Generator, Including a Dynamically Consistent Slip-Rate Function, Applied to the 2019 Mw 7.1 Ridgecrest Earthquake". In: *Bulletin of the Seismological Society of America* 112.1, pp. 287–306. ISSN: 0037-1106.

Prejean, S. G. and Ellsworth, W. L. (2001). "Observations of Earthquake Source Parameters at 2 Km Depth in the Long Valley Caldera, Eastern California". In: *Bulletin of the Seismological Society of America* 91.2, pp. 165–177. ISSN: 0037-1106.

Randall, C. J. (1989). "Absorbing Boundary Condition for the Elastic Wave Equation: Velocity-stress Formulation". In: *GEOPHYSICS* 54.9, pp. 1141–1152. ISSN: 0016-8033.

Raoof, M., Herrmann, R. B., and Malagnini, L. (1999). "Attenuation and Excitation of Three-Component Ground Motion in Southern California". In: *Bulletin of the Seismological Society of America* 89.4, pp. 888–902. ISSN: 0037-1106.

Roten, D., Olsen, K. B., Day, S. M., and Cui, Y. (2018). "Quantification of Fault-Zone Plasticity Effects with Spontaneous Rupture Simulations". In: *Best Practices in Physics-based Fault Rupture Models for Seismic Hazard Assessment of Nuclear Installations*. Ed. by L. A. Dalguer, Y. Fukushima, K. Irikura, and C. Wu. Cham: Springer International Publishing, pp. 45–67. ISBN: 978-3-319-72709-7.

Roten, D., Olsen, K. B., Day, S. M., Cui, Y., and Fäh, D. (2014). "Expected Seismic Shaking in Los Angeles Reduced by San Andreas Fault Zone Plasticity". In: *Geophysical Research Letters* 41.8, pp. 2769–2777. eprint: https://agupubs.onlinelibrary.wiley.com/doi/pdf/10.1002/2014GL059411.

Roten, D., Olsen, K. B., and Pechmann, J. C. (2012). "3D Simulations of M 7 Earthquakes on the Wasatch Fault, Utah, Part II: Broadband (0–10 Hz) Ground Motions and Nonlinear Soil Behavior". In: *Bulletin of the Seismological Society of America* 102.5, pp. 2008–2030. ISSN: 0037-1106.

Roten, D., Cui, Y., Olsen, K. B., Day, S. M., Withers, K., Savran, W. H., Wang, P., and Mu, D. (2016). "High-Frequency Nonlinear Earthquake Simulations on Petascale Heterogeneous Supercomputers". In: *SC '16: Proceedings of the International Conference for High Performance Computing, Networking, Storage and Analysis*, pp. 957–968.

Savage, J. C. and Gross, W. K. (1995). "Revised Dislocation Model of the 1986 Chalfant Valley Earthquake, Eastern California". In: *Bulletin of the Seismological Society of America* 85.2, pp. 629–631. ISSN: 0037-1106.

Savitzky, A. and Golay, M. J. (1964). "Smoothing and Differentiation of Data by Simplified Least Squares Procedures." In: *Analytical chemistry* 36.8, pp. 1627–1639.

Savran, W. H. and Olsen, K. B. (2019). "Ground Motion Simulation and Validation of the 2008 Chino Hills Earthquake in Scattering Media". In: *Geophysical Journal International* 219.3, pp. 1836–1850. ISSN: 0956-540X.

Scott, J. S., Masters, T. G., and Vernon, F. L. (1994). "3-D Velocity Structure of the San Jacinto Fault Zone near Anza, California—I. P Waves". In: *Geophysical Journal International* 119.2, pp. 611–626. ISSN: 0956-540X. eprint: https://academic.oup.com/gji/article-pdf/119/2/611/2060581/119-2-611.pdf.

Seed, H. B., Makdisi, F. I., and Alba, P. D. (1978). "Performance of Earth Dams During Earthquakes". In: *Journal of the Geotechnical Engineering Division* 104.7, pp. 967–994.

Shaw, J. H., Plesch, A., Tape, C., Suess, M. P., Jordan, T. H., Ely, G., Hauksson, E., Tromp, J., Tanimoto, T., Graves, R., Olsen, K., Nicholson, C., Maechling, P. J., Rivero, C., Lovely, P., Brankman, C. M., and Munster, J. (2015). "Unified Structural Representation of the

Southern California Crust and Upper Mantle". In: *Earth and Planetary Science Letters* 415, pp. 1–15. ISSN: 0012-821X.

Small, P., Gill, D., Maechling, P. J., Taborda, R., Callaghan, S., Jordan, T. H., Olsen, K. B., Ely, G. P., and Goulet, C. (2017). "The SCEC Unified Community Velocity Model Software Framework". In: *Seismological Research Letters* 88.6, pp. 1539–1552. ISSN: 0895-0695.

Smith, K. D. and Priestley, K. F. (2000). "Faulting in the 1986 Chalfant, California, Sequence: Local Tectonics and Earthquake Source Parameters". In: *Bulletin of the Seismological Society of America* 90.4, pp. 813–831. ISSN: 0037-1106.

Song, S. G. (2016). "Developing a Generalized Pseudo-Dynamic Source Model of Mw 6.5–7.0 to Simulate Strong Ground Motions". In: *Geophysical Journal International* 204.2, pp. 1254–1265. ISSN: 0956-540X.

Song, S. G., Dalguer, L. A., and Mai, P. M. (2014). "Pseudo-Dynamic Source Modelling with 1-Point and 2-Point Statistics of Earthquake Source Parameters". In: *Geophysical Journal International* 196.3, pp. 1770–1786. ISSN: 0956-540X.

Song, X. and Jordan, T. (2013). "Anelastic Attenuation and Elastic Scattering of Seismic Waves in the Los Angeles Region". In: *AGU Fall Meeting Abstracts*. Vol. 2013, S32B–05.

Spudich, P. and Olsen, K. B. (2001). "Fault Zone Amplified Waves as a Possible Seismic Hazard along the Calaveras Fault in Central California". In: *Geophysical Research Letters* 28.13, pp. 2533–2536. ISSN: 1944-8007.

Taborda, R., Azizzadeh-Roodpish, S., Khoshnevis, N., and Cheng, K. (2016). "Evaluation of the Southern California Seismic Velocity Models through Simulation of Recorded Events". In: *Geophysical Journal International* 205.3, pp. 1342–1364. ISSN: 0956-540X.

Taborda, R. and Bielak, J. (2013). "Ground-Motion Simulation and Validation of the 2008 Chino Hills, California, Earthquake". In: *Bulletin of the Seismological Society of America* 103.1, pp. 131–156. ISSN: 0037-1106.

— (2014). "Ground-Motion Simulation and Validation of the 2008 Chino Hills, California, Earthquake Using Different Velocity Models". In: *Bulletin of the Seismological Society of America* 104.4, pp. 1876–1898. ISSN: 0037-1106.

Townsend, K. F., Clark, M. K., and Zekkos, D. (2021). "Profiles of Near-Surface Rock Mass Strength Across Gradients in Burial, Erosion, and Time". In: *Journal of Geophysical Research: Earth Surface* 126.4, e2020JF005694. ISSN: 2169-9003.

Tu, T., Yu, H., Ramirez-Guzman, L., Bielak, J., Ghattas, O., Ma, K.-l., and O'Hallaron, D. R. (2006). "From Mesh Generation to Scientific Visualization: An End-to-End Approach to Parallel Supercomputing". In: *SC '06: Proceedings of the 2006 ACM/IEEE Conference on Supercomputing*. SC '06: Proceedings of the 2006 ACM/IEEE Conference on Supercomputing, pp. 12–12.

Vidale, J. E. and Li, Y.-G. (2003). "Damage to the Shallow Landers Fault from the Nearby Hector Mine Earthquake". In: *Nature* 421.6922, pp. 524–526.

Wald, D. J. and Allen, T. I. (2007). "Topographic Slope as a Proxy for Seismic Site Conditions and Amplification". In: *Bulletin of the Seismological Society of America* 97.5, pp. 1379–1395. ISSN: 0037-1106.

Wang, R., Schurr, B., Milkereit, C., Shao, Z., and Jin, M. (2011). "An Improved Automatic Scheme for Empirical Baseline Correction of Digital Strong-Motion Records". In: *Bulletin of the Seismological Society of America* 101.5, pp. 2029–2044. ISSN: 0037-1106.

Wang, W. and Shearer, P. M. (2017). "Using Direct and Coda Wave Envelopes to Resolve the Scattering and Intrinsic Attenuation Structure of Southern California". In: *Journal of Geophysical Research: Solid Earth* 122.9, pp. 7236–7251. ISSN: 2169-9313.

Wills, C. J., Gutierrez, C. I., Perez, F. G., and Branum, D. M. (2015). "A Next Generation VS30 Map for California Based on Geology and Topography". In: *Bulletin of the Seismological Society of America* 105.6, pp. 3083–3091. ISSN: 0037-1106.

Withers, K. B., Olsen, K. B., and Day, S. M. (2015). "Memory-Efficient Simulation of Frequency-Dependent QMemory-Efficient Simulation of Frequency-Dependent Q". In: *Bulletin of the Seismological Society of America* 105.6, pp. 3129–3142. ISSN: 0037-1106.

Withers, K. B., Olsen, K. B., Day, S. M., and Shi, Z. (2018a). "Ground Motion and Intraevent Variability from 3D Deterministic Broadband (0–7.5 Hz) Simulations along a Nonplanar Strike-Slip Fault". In: *Bulletin of the Seismological Society of America* 109.1, pp. 229–250. ISSN: 0037-1106.

Withers, K. B., Olsen, K. B., Shi, Z., and Day, S. M. (2018b). "Validation of Deterministic Broadband Ground Motion and Variability from Dynamic Rupture Simulations of Buried Thrust Earthquakes". In: *Bulletin of the Seismological Society of America* 109.1, pp. 212–228. ISSN: 0037-1106.

Yiagos, A. N. and Prevost, J. H. (1991). "Two-Phase Elasto-Plastic Seismic Response of Earth Dams: Applications". In: *Soil Dynamics and Earthquake Engineering* 10.7, pp. 371–381. ISSN: 0267-7261.

Yong, A., Martin, A., Stokoe, K., and Diehl, J. (2013). *ARRA-funded VS30 Measurements Using Multi-Technique Approach at Strong-Motion Stations in California and Central-Eastern United States*. US Department of the Interior, US Geological Survey.

Zahradník, J., Moczo, P., and Hron, F. (1993). "Testing Four Elastic Finite-Difference Schemes for Behavior at Discontinuities". In: *Bulletin of the Seismological Society of America* 83.1, pp. 107–129. ISSN: 0037-1106.

Zeghal, M. and Abdel-Ghaffar, A. M. (1992). "Analysis of Behavior of Earth Dam Using Strongmotion Earthquake Records". In: *Journal of Geotechnical Engineering* 118.2, pp. 266–277.

Zhao, J. X., Liang, X., Jiang, F., Xing, H., Zhu, M., Hou, R., Zhang, Y., Lan, X., Rhoades, D. A., Irikura, K., Fukushima, Y., and Somerville, P. G. (2016). "Ground-Motion Prediction Equations for Subduction Interface Earthquakes in Japan Using Site Class and Simple Geometric Attenuation Functions". In: *Bulletin of the Seismological Society of America* 106.4, pp. 1518–1534. ISSN: 0037-1106.

Zhou, Z., Bianco, M., Gerstoft, P., and Olsen, K. (2022). "High-Resolution Imaging of Complex Shallow Fault Zones along the July 2019 Ridgecrest Ruptures". In: *Geophysical Research Letters* 49.1. e2021GL095024 2021GL095024 e2021GL095024 2021GL095024, e2021GL095024. eprint: https://agupubs.onlinelibrary.wiley.com/doi/pdf/10.1029/2021GL095024.